Observational studies on the temporal and spatial structures of the deep-circulation current in the western North Pacific

西部北太平洋における深層循環流の時空間的構造の観測的研究

柳本　大吾

Observational studies on the temporal and spatial structures of the deep-circulation current in the western North Pacific

A dissertation submitted for the degree of Doctor of Science

BY

Daigo Yanagimoto

Atmosphere and Ocean Research Institute, The University of Tokyo

Abstract

For understanding the global deep ocean circulation, which occupies large part of the global meridional overturning circulation, knowing its pathway and volume transport is essential. The author clarified the pathway and the volume transport variability of the deep-circulation current in the western North Pacific with analyzing current velocity data directly measured at two mooring arrays along 165°E and southwest of the Shatsky Rise. The both arrays were deployed at key points for the deep-circulation current in the region between 20°N and 35°N in the Northwest Pacific Basin. Five moorings were deployed at 27°–35°N along 165°E from 1991 to 1993 and additional one mooring at 27°N, 168°E from 1989 to 1991. Nine moorings were deployed between the Shatsky Rise and the Ogasawara Plateau (an eastward bulge from the Izu-Ogasawara Ridge near 25°N) from 2004 to 2005 and additional two moorings on the foot of the Shatsky Rise from 2003 to 2004. The author also utilized recent high-quality and high-resolution dissolved-oxygen data in order to estimate the pathway of the deep-circulation current passing the moorings.

First, the pathway of the deep-circulation current was examined. The eastern branch of the deep-circulation current passes north-northeastward through the Wake Island Passage, turns cyclonically with flowing northwestward around 33°N, 165°E, takes a detour south of the Shatsky Rise, then, flows northwestward mainly on the lower part of the slope of the Shatsky Rise. The deep-circulation current is not found to flow eastward between the Wake-Necker Ridge and the Hess Rise into the Northeast Pacific Basin. The western branch of the deep-circulation current proceeds northward beyond 25°N with a detour east of the Ogasawara Plateau. Thus, both of the eastern and western branches enter the central region of the Northwest Pacific Basin through the relatively narrow strait between the Shatsky Rise and the Ogasawara Plateau.

Next, the temporal variations of volume transports of the western and eastern branches were examined southwest of the Shatsky Rise. Almost zero volume transport occurs at intervals of 2–4 months in the both branches. They have dominant spectral peaks at periods of 3 months and 1month. This is similar to the volume transport variation at the Wake Island Passage in the North Pacific, while it is not similar to those at the Samoan Passage and in the Southwest Pacific Basin in the South Pacific.

Additionally, volume transport variation of the eastern branch has high correlation with its width variation. The eastern branch flowing with an average width of 200 ± 70 km intermittently expands up to 200 km away southwestward from its main position on the lower

part of the slope of the Shatsky Rise. The western branch is so narrow that we find it almost exclusively at one mooring system northeast of the Ogasawara Plateau.

These findings do not only elucidate the pathway of the deep circulation in the western North Pacific that has been different for researchers so far, but also provide an important suggestion on the northward extension of the meridional overturning circulation in the Pacific to the Aleutian Trench.

Acknowledgement

I would like to express my sincere thanks to Prof. M. Kawabe for his invaluable suggestions and advices and continuous encouragement. I would like to express my great thanks to Prof. S. Fujio for his invaluable suggestions and advices. I greatly thank to Drs. E. Oka and K. Tanaka for their helpful suggestions and advices and to Mr. S. Kitagawa for his excellent technical works. I greatly thank to Profs. H. Hasumi, T. Hibiya, I. Yasuda, M. Sato, and K. Iga for their helpful suggestions. I would like to express my thanks to my colleagues in the former Ocean Research Institute and the existing Atmosphere and Ocean Research Institute for fruitful discussions. I would like to express my hearty thanks to Prof. Emeritus K. Taira for his continuous encouragement.

The mooring works, that the present thesis is essentially based on, were carried out in cruises KH-91-5, KH-93-2, KH-03-1, KH-04-4, and KH-05-4 of the R/V Hakuho-maru. The hydrographic observations, that the present thesis is greatly based on, were carried out in these cruises as well as the additional ones of the R/V Hakuho-maru, i.e., KH-95-1, KH-99-1, KH-07-1. I am greatly indebted to the captains and crews of the R/V Hakuho-maru, and the scientists who joined the cruises with the author.

I am greatly thankful to my family.

Contents

Chapter 1. General introduction

In the ocean, there are horizontal wind-driven circulations as well as a global meridional overturning circulation (MOC), which is associated with sinking at high latitudes in the North Atlantic and the Southern Ocean and upwelling elsewhere. The MOC takes a significant role for moderating the world climate by transporting cold waters from high latitudes to low latitudes in the lower layer and warm waters from low latitudes to high latitudes in the upper layer. Therefore, the MOC is attracting attention of oceanographers in recent years in particular as is reviewed by Richardson (2007). The deep circulation occupies the thick deep portion of the MOC and contributes greatly to transporting heat and materials. The MOC in the Pacific Ocean, where there is no significant sinking of water from the surface to the abyssal layer, consists of the deep circulation flowing northward from the Southern Ocean and southward from the North Pacific. It is a large question how far north the MOC extends in the Pacific Ocean.

The global deep circulation originates from formation of saline, oxygen-rich deep water, North Atlantic Deep Water (NADW), mainly off Greenland. NADW is transported southward to the Southern Ocean, where NADW is reformed to Lower Circumpolar Deep Water (LCDW) with affected by cold Antarctic Bottom Water (AABW) formed around Antarctica. Thus, LCDW does not only have low temperature but also inherits a feature of high salinity and high dissolved oxygen from NADW. Such dense, oxygen-rich LCDW spreads along the bottom to each ocean from the Southern Ocean with transported northward by the deep circulation. Therefore, high dissolved oxygen and low silica of LCDW is used as a tracer of the deep circulation (e.g., Mantyla and Reid, 1983). The main stream of the deep circulation transporting LCDW is referred as “deep-circulation current” in this thesis.

The South Pacific has two entrances for LCDW, i.e., the Southwest Pacific Basin and the Chile Basin (Mantyla and Reid, 1983) (Fig. 1.1). While LCDW entering the Chile Basin does not proceed northward beyond the equator due to sill depth, LCDW entering the Southwest Pacific Basin is transported northward further to the North Pacific. Because the Southwest Pacific Basin has simple bottom topography, LCDW and the deep-circulation current are found along the Tonga-Kermadec Ridge, the western boundary of the basin (Fig. 1.2), as is expected from the idealized-model theory by Stommel and Arons (1960). At 32°30′S in the Southwest Pacific Basin, LCDW is found as a high-salinity core of 34.72–34.73 PSU below 3000 m depth, and it has high dissolved oxygen (4.8 ml l^{-1}) and low temperature (0.58°C) (Whitworth et al., 1999). The volume transport of LCDW at this latitude is estimated at 12 Sv (1 Sv = 10^6 m^3 s^{-1}) as a geostrophic transport based on inversely-solved reference velocities by Tsimplis et al.

(1998).

After flowing northward along the Tonga-Kermadec Ridge in the Southwest Pacific Basin, LCDW reaches series of ridges from the Manihiki Plateau to the Robby Ridge (Fig. 1.2). LCDW passes through the Samoan Passage, the eastern flank of the Manihiki Plateau, and a gap of the Robby Ridge, and enters the Central Pacific Basin. Roemmich et al. (1996) estimate volume transports of LCDW (θ<1.1°C) passing these passages at 7.8 Sv in the Samoan Passage, 2.8 Sv at the eastern flank of the Manihiki Plateau, and 1.1 Sv in the Robby-Ridge gap; thus, LCDW is transported with volume transport of 11.7 Sv into the Central Basin. Taft et al. (1991) also estimate geostrophic volume transport in the Samoan Passage at 6.0 Sv.

Distributions of water properties show that LCDW spreads from the Central Pacific Basin to the basins in the North Pacific (Mantyla and Reid, 1983). In contrast with the western South Pacific, it has been difficult to identify its pathway in the western North Pacific due to the extremely complex bottom topography (Fig. 1.2). Nevertheless, accumulation of precise observation data in the World Ocean Circulation Experiment (WOCE) in the 1990s and post-WOCE experiments has made clear the detail of the deep-circulation current in the tropical North Pacific. It is clarified that the deep-circulation current bifurcates into two branch currents in the Central Pacific Basin due to sill depth of the western boundary of the basin, the Gilbert Ridge. The deep part of the deep-circulation current forms the eastern branch, flowing northward along the Gilbert Ridge toward the Wake Island Passage with a volume transport of 8.1 Sv, whereas the shallow part forms the western branch flowing into the Melanesian and East Mariana basins beyond the ridge with a volume transport of 2–6 Sv (Johnson and Toole, 1993; Kawabe, 1993; Kawabe and Taira, 1995; Kawabe et al., 2003; Kawabe et al., 2006) (Fig. 1.2).

The eastern branch has another separation of northward and eastward flows in the Central Pacific Basin (black arrows in Fig. 1.2). The eastward flow enters the Northeast Pacific Basin (Kato and Kawabe, 2009) and the northward flow enters the Northwest Pacific Basin through the Wake Island Passage and adjacent gaps in the Mid-Pacific Seamounts (Kawabe et al., 2003). The eastern branch passing the Wake Island Passage northward is examined with using moorings by Kawabe et al. (2005). They revealed its mean volume transport of 3.6 ± 1.3 Sv. The total northward volume transport including those at the adjacent gaps is estimated at more than 4 Sv.

The western branch in the East Mariana Basin also separates into flows toward adjacent basins (gray arrows in Fig. 1.2). Some part flows into the West Mariana Basin and some part flows into the East Caroline Basin. Kawabe et al. (2003) estimate the volume transport to the

West Mariana Basin as 0.3 Sv and the one to the East Caroline Basin as 1.7 Sv. Siedler et al. (2004) confirmed these currents with using moorings and estimate total volume transport to the two basins at 1 Sv. The remaining part of the western branch proceeds further northward through gaps in the Magellan Seamounts with a volume transport of 2.1 Sv (Kawabe et al., 2003).

Thus, the deep-circulation current south of 20°N and the Wake Island Passage was clarified by Kawabe et al. (2003, 2005). However, the eastern branch north of the Wake Island Passage is not yet confirmed and is shown with broken lines in Kawabe et al. (2003) (Fig. 1.3). According to geostrophic velocity and dissolved oxygen distribution obtained in sections of WOCE Hydrographic Programme (WHP) P13C and P13J at 165°E, Kawabe and Taira (1995) suppose that the eastern branch turns cyclonically in the small basin surrounded by the Shatsky Rise, the Emperor Seamount Chain, and the Wake–Necker Ridge after passing the Wake Island Passage. Eastward outflow near the Midway Island toward the Northeast Pacific Basin inferred from dissolved-oxygen distribution by Mantyla and Reid (1983) and northward proceeding of the western branch with a detour east of the Ogasawara Plateau, an eastward bulge of the Izu-Ogasawara Ridge at 25°N, suggested by Kawabe et al. (2003) are also drawn with broken lines in Fig. 1.3.

On the other hand, Wijffels et al. (1998) show water-mass distribution and geostrophic volume transport from their meridional hydrographic section of WHP P10 at about 149°E. They indicate westward geostrophic transport (7.9 Sv) in the deepest layer north of 25°N; this is similar with the westward pathway of the eastern branch supposed by Kawabe and Taira (1995) (Fig. 1.4a). However, they illustrate the western branch transporting LCDW blocked by a benthic water-mass front near 25°N and turning eastward with mixing with the upper water (Fig. 1.4b).

Furthermore, Owens and Warren (2001) illustrate the deep circulation with summarizing previous results of observations and simulations (Fig. 1.5). They adopt an eastward pathway of the deep water passing between the Shatsky Rise and the Mid-Pacific Seamounts after bifurcating from the western branch north of the Ogasawara Plateau. The eastward current proceeds nearly along 30°N, joins the eastern branch, goes further eastward, and finally flows out to the Northeast Pacific Basin as inferred by Mantyla and Reid (1983). Therefore, the cyclonic turn of deep current near 35°N, 165°E is illustrated as just a local gyre out of the main stream of the deep-circulation current. This eastward pathway of the deep-circulation current contradicts the pathway of the eastern branch supposed by Kawabe and Taira (1995).

Therefore, the deep-circulation current in the southern region between 20°N and 35°N of

the Northwest Pacific Basin must be clarified and confirmed on the basis of observation data. The points of issue to be solved are (1) whether part of the eastern branch flows eastward between the Wake-Necker Ridge and the Hess Rise into the Northeast Pacific Basin or not, (2) whether the western branch proceeds northwestward with a detour east of the Ogasawara Plateau or not, and (3) whether the deep-circulation current flows westward or eastward between 20°N and 35°N. These questions (1), (2), and (3) are examined in this thesis.

The answer to these questions will provide an important suggestion particularly on the northward extension of the MOC in the Pacific. If the deep circulation passes eastward the region at about 30°N between the Wake-Necker Ridge and the Hess Rise (the red star in Fig. 1.1), most of the LCDW carried by the deep-circulation current enters the Northeast Pacific Basin to the south of approximately 30°N, and the MOC in the Pacific mostly turns over at mid-latitude region. However, if not, almost the deep water would continue moving to the northernmost point at about 55°N in the Northwest Pacific Basin, and then, would enter the Northeast Pacific Basin along the Aleutian Trench (the blue star in Fig. 1.1), and the MOC in the Pacific extends to the subpolar region.

Moreover, the author examines variability of the deep-circulation transport in the Pacific. In many cases, volume transports of the deep-circulation current are estimated with geostrophic calculation as previously noted. Actually, large variability of volume transport of the deep-circulation current is reported from the few mooring results in the Pacific. In the Southwest Pacific Basin, Whitworth et al. (1999) show its volume transport varying from -6.6 Sv to 44.9 Sv by 22-month moorings (Fig. 1.6) while Tsimplis et al. (1998) estimate its geostrophic volume transport crossing 32°30′S at 12 Sv by an inverse method. At the Samoan Passage, Rudnick (1997) shows that the volume transport varies from 1.1 Sv to 10.7 Sv during 17 months (Fig. 1.7) while the mean transport of 6.0 ± 1.5 Sv is similar to geostrophic transports of 6.0 Sv (Taft et al., 1991) and 7.8 Sv (Roemmich et al., 1996). Kawabe et al. (2005) estimate the volume transport of the eastern branch passing through the Wake Island Passage at 3.6 ± 1.3 Sv on an average; it varies from -5.3 to 14.8 Sv (Fig. 1.8). The geostrophic volume transport of LCDW at the Wake Island Passage is extremely small (nearly zero) in 1999 (Kawabe et al., 2003) when the mooring result shows temporary weakness of current speed and volume transport (Kawabe et al., 2005). This indicates that snapshots of geostrophic volume transport from hydrographic sections could not have representativeness and must be evaluated with direct measurements.

To study these subjects, the author analyzed directly-measured current velocity data and recent high-quality dissolved-oxygen data. In Chapter 2, the author analyzed current velocity data from a mooring array with 5 systems from 27°N to 35°N at 165°E from 1991 to 1993 with

a system at 167°E, 27°N during 1989–1991, and examined the question (3). In Chapter 3, the author mapped dissolved oxygen with recent high-quality hydrographic data accumulated since the WOCE era and examined the questions (1) and (3). In Chapter 4, the author analyzed current velocity data from a mooring array with 9 systems between the Shatsky Rise and the Ogasawara Plateau from 2004 to 2005, and examined the questions (2) and (3) as well as the variability of deep-circulation transport. Finally, the general conclusion is written in Chapter 5. The contents in Chapters 2 and 3 have been published in Yanagimoto and Kawabe (2007) and the contents in Chapter 4 have been published in Yanagimoto et al. (2010).

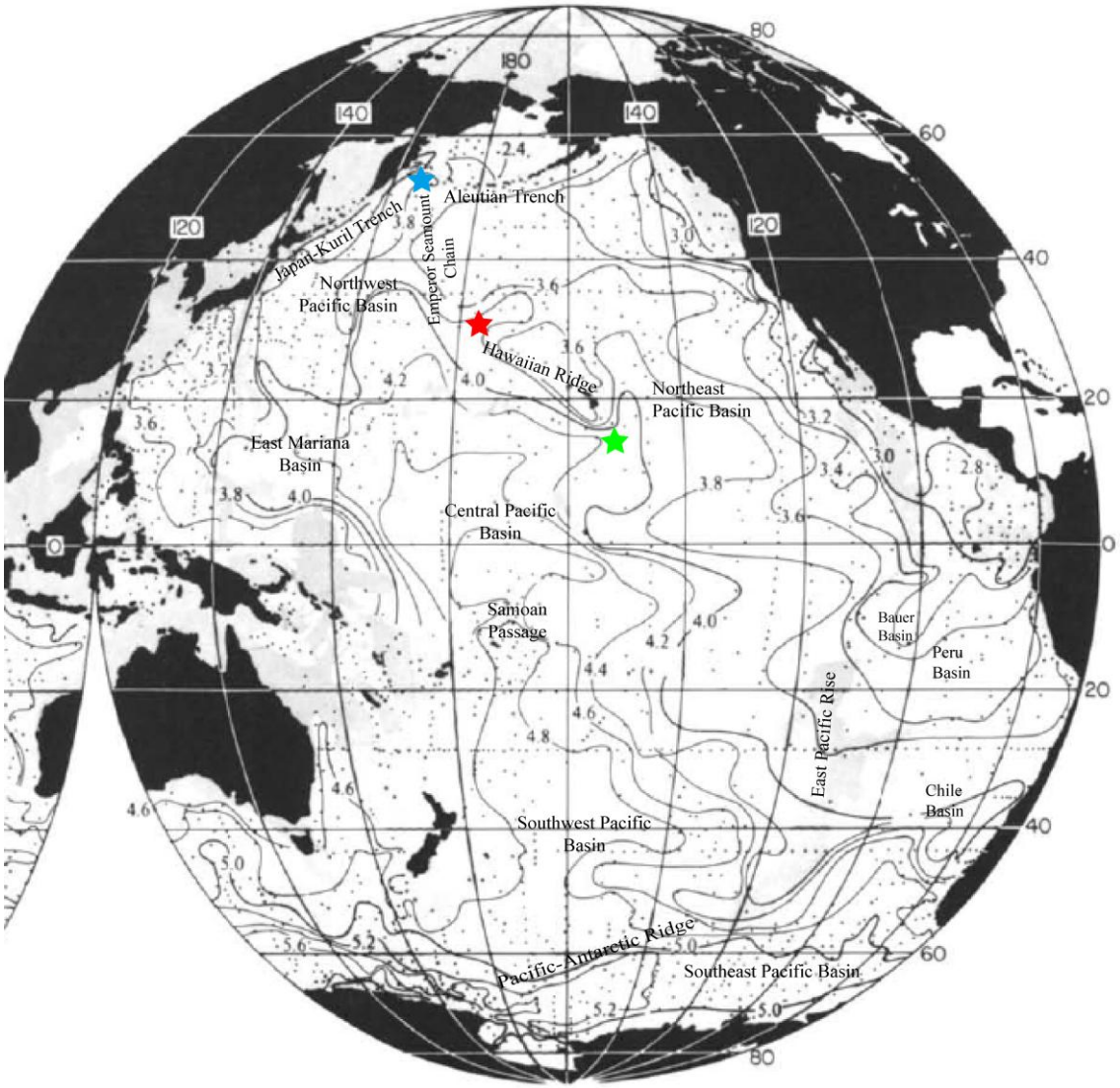

Fig. 1.1 Distribution of dissolved oxygen (ml l^{-1}) near the bottom in the Pacific from Mantyla and Reid (1983). They indicated that the three points shown with blue, red, and green stars are entrances of the deep water to the Northeast Pacific Basin.

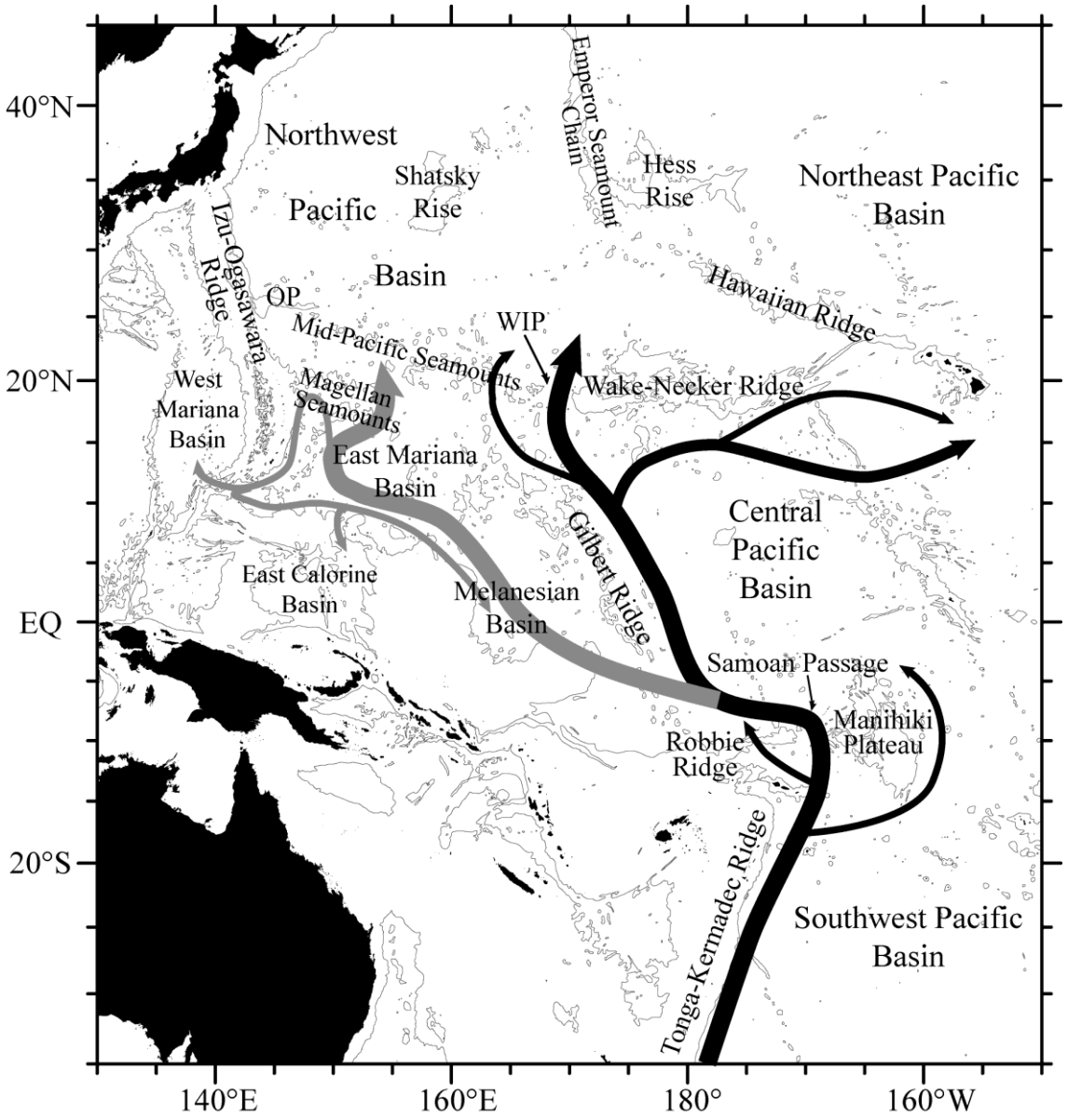

Fig. 1.2 Bottom topography and pathways of the deep-circulation current in the western Pacific. The black arrow shows the deep-circulation current and the following eastern branch, and the gray arrow shows the western branch of the deep-circulation current. Bottom topography is shown by isobaths of 4000 m. WIP and OP is an abbreviation for the Wake Island Passage and the Ogasawara Plateau, respectively.

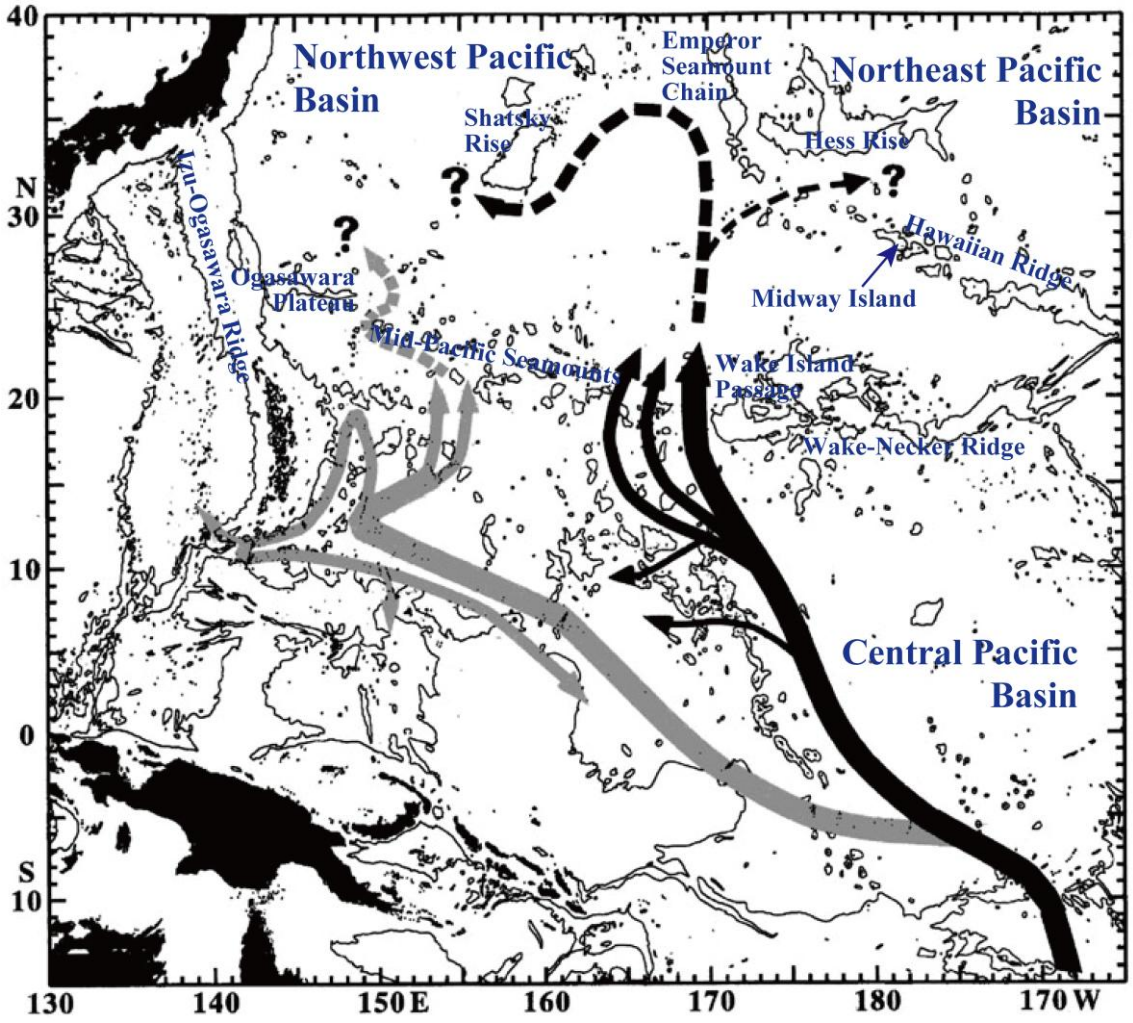

Fig. 1.3 Schematic of the deep circulation in the western Pacific by Kawabe et al. (2003). Black and gray arrows from the Central Pacific Basin show the pathways of the eastern and western branch of the deep circulation, respectively.

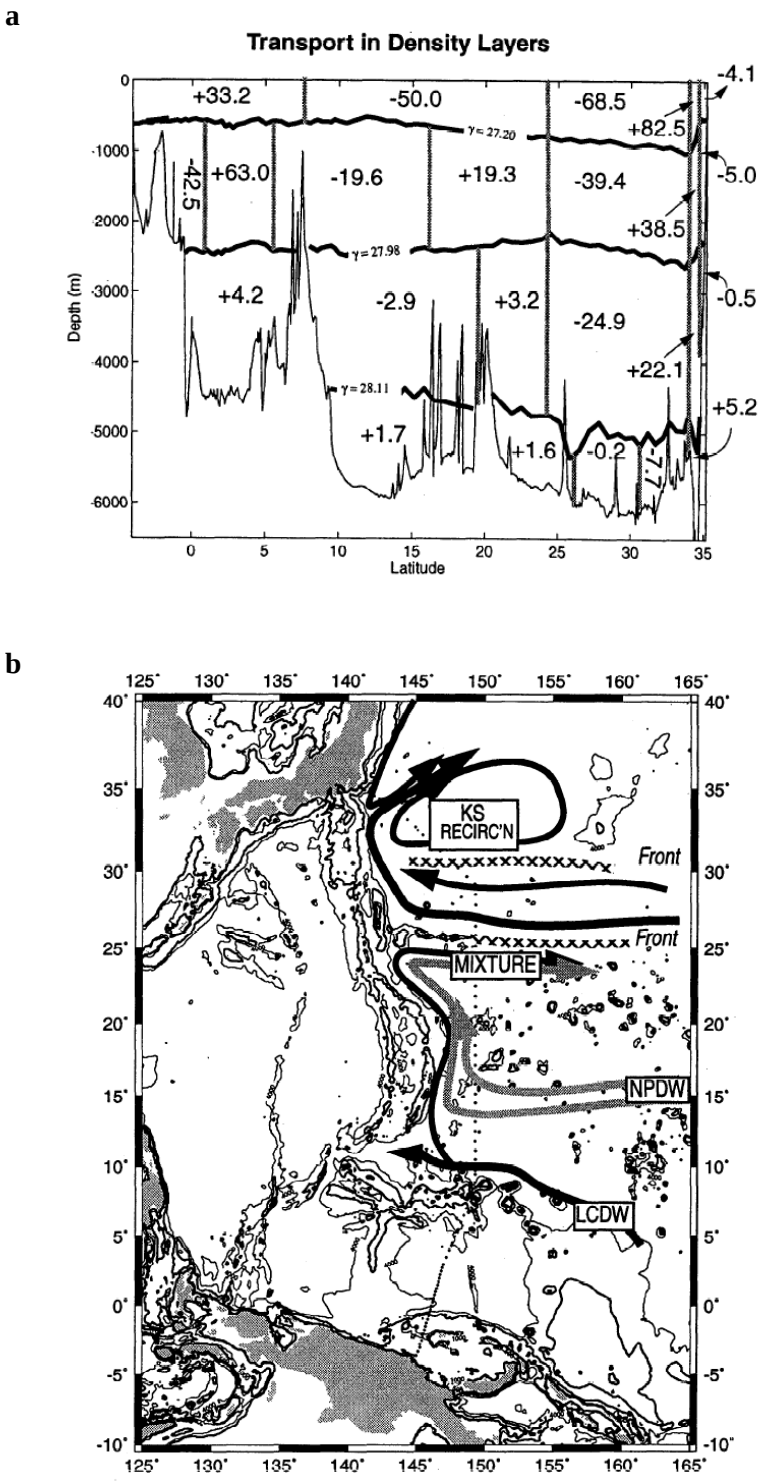

Fig. 1.4 (a) Distribution of volume transport at a hydrographic section, WHP P10, mostly along 149°E, and (b) schematic of deep currents at depths of 2500–4500 m based on the section (Wijffels et al., 1998).

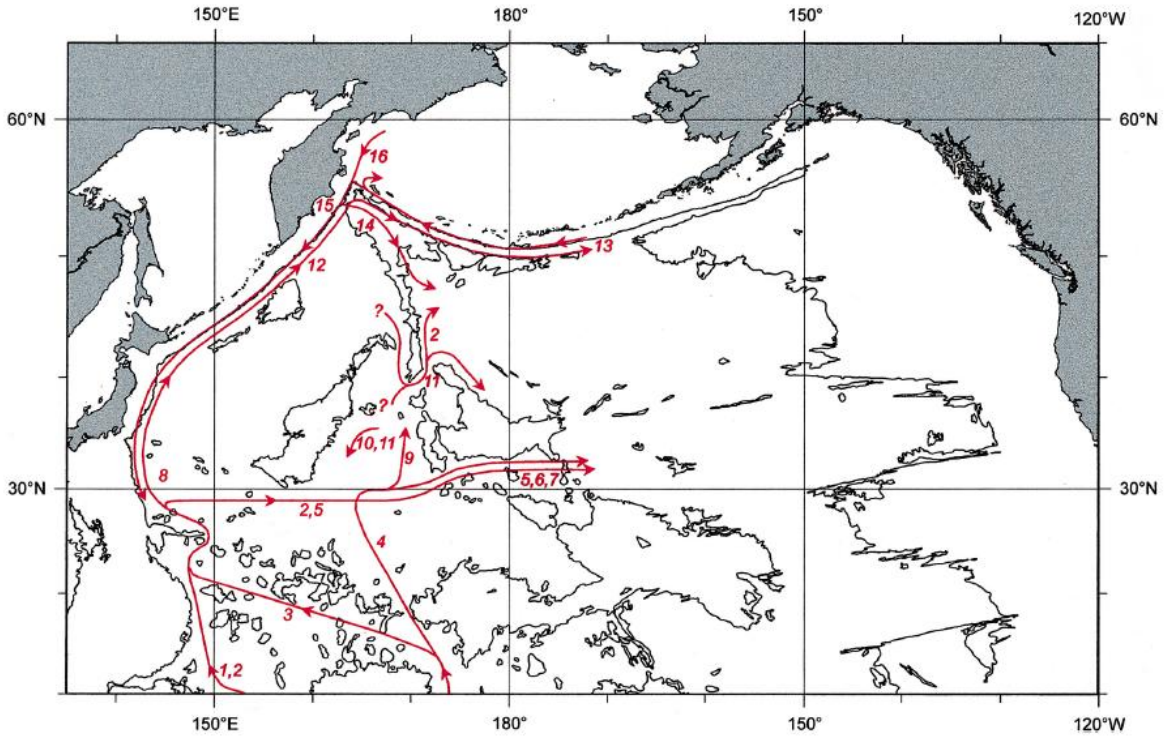

Fig. 1.5 Schematic of deep currents based on previous observations and simulations summarized by Owens and Warren (2001). Numbers indicate references which they adopt (see their text).

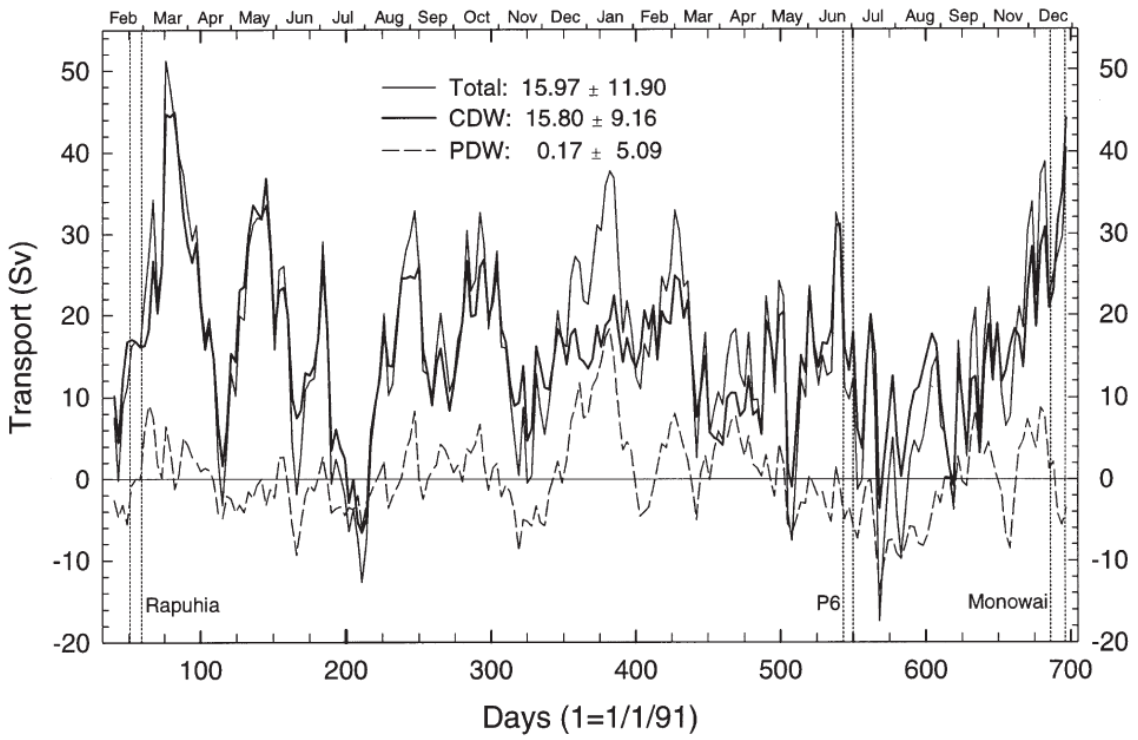

Fig. 1.6 Time series of total volume transport at the PCM9 array at 32°30′S and volume transports of Lower Circumpolar Deep Water (CDW in this figure) and Pacific Deep Water (PDW) (Whitworth et al., 1999).

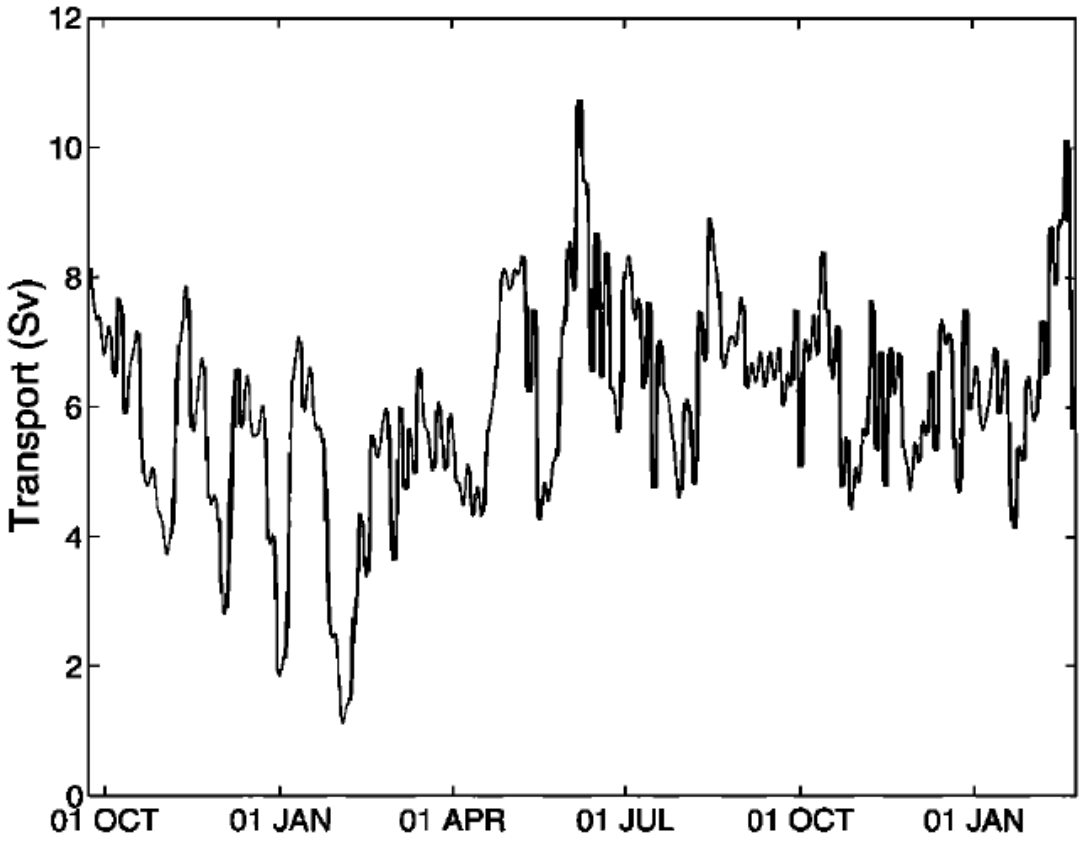

Fig. 1.7 Time series of volume transport deeper than 4000-m depth in the Samoan Passage (Rudnick, 1997).

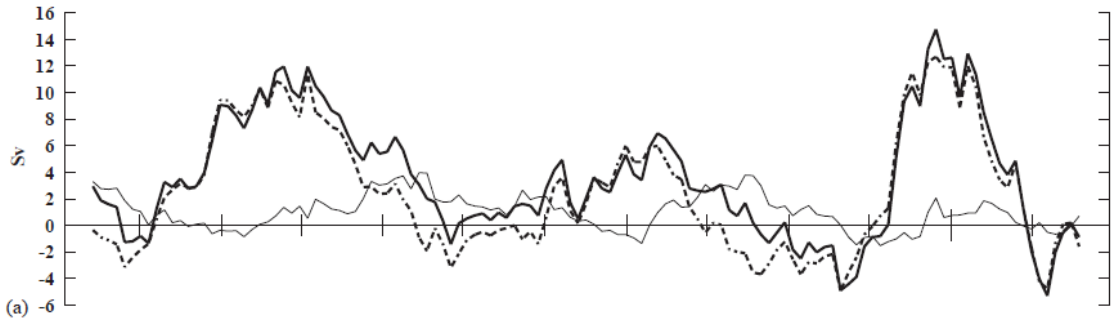

Fig. 1.8 Time series of volume transport of the eastern branch in the Wake Island Passage (Kawabe et al., 2005). Thin solid and broken line shows the volume transport in the western and eastern half of the passage, respectively, and thick solid line shows the total volume transport.

Chapter 2. Temporal and spatial characteristics of deep-circulation current measured at mid-latitude of 165°E

2.1. Introduction

Lower Circumpolar Deep Water (LCDW) that separates from the Antarctic Circumpolar Current flows northward along the deep western boundary of the South Pacific, enters the Central Pacific Basin through the Samoan Passage, and spreads to neighboring basins in the North Pacific, such as the Northwest Pacific Basin, the Northeast Pacific Basin, and the East Mariana Basin (Mantyla and Reid, 1983). Figure 2.1 shows topographic features of the western North Pacific. The pathway of LCDW around the Central Pacific Basin is bifurcated into the eastern and western branches north of the Samoan Passage. The densest, coldest LCDW is carried by the eastern branch current of the deep circulation and flows northward along the Gilbert Ridge at the western periphery of the Central Pacific Basin and through the Wake Island Passage (Johnson and Toole, 1993; Kawabe et al., 2003). The eastern branch current of the deep circulation is called the deep-circulation current in the present chapter. The deep-circulation current through the Wake Island Passage was confirmed by direct current measurement with a one-year mooring (Kawabe et al., 2005).

In the early 1990s, 165°E meridional hydrographic observations were conducted three times as part of the World Ocean Circulation Experiment (WOCE) Hydrographic Programme (WHP): WHP P13C in 1991, P13 in 1992, and P13J in 1993. Kawabe and Taira (1995) analyzed hydrographic data from WHP P13C and P13J and concluded from geostrophic velocity and dissolved oxygen distribution that the deep-circulation current proceeds northward east of 165°E up to 29°N and passes 165°E westward between 32° and 35°N. They supposed that the deep-circulation current turns cyclonically in the basin between the Shatsky Rise and the Emperor Seamount Chain. This is based on not only their observations at 165°E but also the following previous findings: (1) the lowest temperature and nutrients, the highest salinity and oxygen near the bottom around 165°E in the INDOPAC section at 35°N (Kenyon, 1983); (2) the lack of evidence of cold, high-oxygen water north of 36°N in a 165°E meridional section (Joyce, 1987); and (3) stable northwestward flow at 4000-m depth at 33°N, 165°E measured from 1983 to 1985 with moored current meters (Schmitz, 1987).

Kawabe and Taira (1995) indicated that the deep-circulation current at 165°E changed the meridional location by 1° latitude between WHP P13C and P13J. Figure 2.2 shows dissolved oxygen distribution on a deep isopycnal surface σ_5 = 50.17 kg m^{-3} observed in three WHP P13

sections. The oxygen distribution in WHP P13C and P13J was the same as that in Kawabe and Taira (1995). High-oxygen water was found between 29°N and 35°N, and the location of oxygen peaks differed among the three sections. This confirms their conclusion of the approximate position and meridional variation of the deep-circulation current by taking into consideration the additional data of WHP P13 in 1992, although current variations cannot be clarified with the data collected at the three time points.

In the present chapter, the author reveals the spatial and temporal properties of the deep-circulation current with analyzing current velocity data obtained with current meters moored for approximately two years at depths greater than 3800 m at five stations from 27°N to 35°N, 165°E and at one station at 27°N, 168°E.

2.2. Mooring observations

We conducted direct current measurement for approximately two years using five mooring systems with 24 current meters at intervals of two degrees of latitude between 27°N and 35°N at 165°E (Fig. 2.1, Table 2.1). The five moorings were anchored from 20 to 24 August 1991 on the R/V Hakuho-maru cruise KH-91-5 (WHP P13C) and were recovered from 17 to 22 May 1993 on KH-93-2 (WHP P13J). The moorings were labeled accordingly from M1 at 35°N to M5 at 27°N. Five current meters were moored near the bottom (30 m from the bottom), one at each of the five moorings, and three were moored at depths of approximately 4000 m, one each at M1, M3, and M5. Water depth at every mooring point was approximately 6000 m. Water depths and mooring depths were based on echo sounding of the ocean floor using a ship-mounted precision depth recorder (PDR) at the time when the moorings were anchored on KH-91-5. All of the current meters near the bottom and two current meters at 4000-m depth at M1 and M5 recorded velocity data during the full mooring period. The current meter at 4000 m at M3 failed to function.

Another mooring, CP, was deployed at 27°N, 168°E from 3 November 1989 to 25 August 1991. Mooring CP had three current meters moored at depths of 5820 m (30 m from the bottom), 4820 m, and 3820 m, but the first two current meters failed to function.

We used Aanderaa RCM5 current meters and equivalent instruments manufactured by Union Engineering Co., Ltd., Japan. Inertial oscillations and diurnal and semi-diurnal tides were filtered out with a Gaussian filter equivalent to “gaus24” described by Thompson (1983). We analyzed the values daily at midnight of the coordinate universal time.

2.3. Temporal and spatial variations of near-bottom currents at 165°E

The most prominent feature of the near-bottom current at 165°E is the strong

northwestward flow with stable current direction at a depth of 6180 m at M2 (33°N), which continues almost throughout the observation period (Fig. 2.3b). This northwestward flow is the main part of the deep-circulation current (Kawabe and Taira, 1995; Fig. 2.2). The vector mean velocity is 7.77 cm s^{-1}, 310°T, and is the highest among those of the five moorings (Table 2.1). This flow has a very sharp peak at 310°T in the current direction histogram and a mean velocity of 12 cm s^{-1} for the 310°T sector, which is the highest mean velocity among current direction sectors (Fig. 2.4). As a result, it has the highest ratio of vector velocity mean to scalar velocity mean ($|\bar{\mathbf{u}}|/\overline{|\mathbf{u}|}$) among the five recorded near-bottom currents (Table 2.1). The ratio represents stability of current direction; the higher this ratio is, the more stable the current direction is, and it becomes 1.0 when current does not change direction at all besides occurrence of no velocity.

The northwestward flow at M2 is strong at WHP P13 (21 cm s^{-1}, 310°T) and P13J (17 cm s^{-1}, 317°T) at which the northern oxygen peak exists near 33°N, whereas the flow at M2 is weak and southwestward at P13C (6 cm s^{-1}, 239°T), because the deep-circulation current is located at 33°–35°N (Kawabe and Taira, 1995). Suspensions of the northwestward flow during August–September 1991, March and June 1992, and December 1992–February 1993, occurring with intervals of seven or eight months, must be due to a meridional shift of the deep-circulation current. Therefore, the variations of near-bottom current velocity at M2 are due to variations of not only velocity amplitude but also position of the deep-circulation current. Except for the suspensions, the deep-circulation current continues to exist around M2, keeping the northwestward flow direction, as the major axis of variance is parallel to the mean current (Table 2.1).

The relatively high oxygen at 31°N in Fig. 2.2 suggests that the mooring M3 is located in the deep-circulation current at least temporarily. Near-bottom current at M3 is dominated by north-northwestward to northward flows and is almost northward on average, but has significant velocity in the west-northwestward to northwestward direction despite the low frequency (Figs. 2.4c and 2.5). The strong northwestward flow during December 1991–January 1992 and April–May 1993 is probably the deep-circulation current that occupies M2 and M3 (Fig. 2.3). Thus, the deep-circulation current occasionally expands or shifts southward and is located around the region 31°–33°N for approximately one month.

Schmitz (1987) showed that a strong northwestward current of 6.2 cm s^{-1} on average flowed at 4000-m depth at 33˚N, 165˚E during 1983–1985 (Fig. 2.5). This mean current has almost the same direction and similar velocity, in comparison with the mean near-bottom current with a velocity of 7.8 cm s^{-1} in the present study. The deep-circulation current at 4000-m depth at the Wake Island Passage has a mean velocity of 0.4–0.9 cm s^{-1} and is much

weaker than the near-bottom flow with a mean velocity of 1.9–3.5 cm s^{-1} (Kawabe et al., 2005). The velocity at 4000-m depth at 33°N, 165°E during 1983–1985 is too high for the deep-circulation current at 4000-m depth. An anti-clockwise deep eddy would exist south of the deep-circulation current as seen in the geostrophic flow distribution at the 165°E section (Kawabe and Taira, 1995), and would overlap the deep-circulation current at 33°N, 165°E.

The near-bottom current at M1 (35°N) has large meso-scale variability, and the current direction has several peaks in the histogram (Figs. 2.3a and 2.4a). Consequently, the mean current speed is very low and not statistically significant (Fig. 2.5, Table 2.1). The frequency of the current direction is significant for north-northwestward flow between 330° and 350°T and southward flow between 170° and 190°T. The north-northwestward flow during August–September 1991, during which the deep-circulation current is not located at M2, is possibly the deep-circulation current. However, the current velocity during this period is similar to that at depths of 4000 m (Fig. 2.6a) and 2500 m (not shown), having mean velocities of 8.47 cm s^{-1}, 329°T near the bottom, 7.99 cm s^{-1}, 333°T at 4000-m depth, and 7.46 cm s^{-1}, 344°T at 2500-m depth. Such a barotropic structure in the deep layer differs from the significant upward decrease in strength of the deep-circulation current at the Wake Island Passage to the extent that the mean velocity at 4000-m depth decreases to one-fourth or one-fifth of that near the bottom (Kawabe et al, 2005). Moreover, the dissolved oxygen at WHP P13C is low at M1 (Fig. 2.2). These observations suggest that the deep-circulation current did not extend to M1, although it was located at 33°–35°N (Kawabe and Taira, 1995). It is described in Section 2.4 that the deep current at M1 may be due to meso-scale eddies throughout the mooring period.

Moorings M4 (29°N) and M5 (27°N) are located outside the deep-circulation current. The near-bottom current at M4 is dominant in the direction of 170°T; it does not have the northward component (-90°–90°T) of velocity (Figs. 2.3d and 2.4d) but has a high southward mean velocity (4.88 cm s^{-1}, 184°T) with high direction stability (Fig. 2.5, Table 2.1). The near-bottom current at M5 is dominant in the direction of 30°–120°T, with a high east-northeastward mean velocity (3.13 cm s^{-1}, 75°T) (Figs. 2.3e, 2.4e, and 2.5, Table 2.1). Mooring M5 is located immediately east of the northern end of a line of deep seamounts extending northeastward from the Mid-Pacific Seamounts, as shown by the 5500-m isobaths in Fig. 2.5. The deep flow must be strongly influenced by this seamount, so that the direction of the near-bottom current at M5 is confined to a relatively small range, and the mean direction (75°T) is similar to the direction of the seamount. The effect of the seamount seems to extend to the current at 4000-m depth at M5. The direction histogram is similar to that of the near-bottom current, although the velocity is much lower in all directions (Figs. 2.6b and 2.7b).

The current at 4000-m depth at CP (27°N, 168°E) is extremely weak throughout the observation period and has no directional dominancy (Figs. 2.6c and 2.7c). Its mean velocity is too low to have any statistical significance (Fig. 2.5, Table 2.1) and is negligible in comparison with the mean velocities at 4000-m depth at the Wake Island Passage (0.93 and 0.40 cm s^{-1}), which are statistically significant (Kawabe et al., 2005). This implies that the deep-circulation current does not pass mooring CP.

2.4. Frequency-domain characteristics of current variations

Power spectral densities of major axis components of velocity variations are shown in Fig. 2.8. The largest power spectral density exists at periods longer than 100 days near the bottom at M2, having the maximum around 250 days (Fig. 2.8b). The periods of 250 days correspond to the intervals (seven or eight months) of suspensions of northwestward flow at M2, as discussed in Section 2.3, and the long-term variations may be due to the southward shift of the deep-circulation current.

Spectral densities over the period of 30 to 80 days at M1 are the largest among meso-scale variances at all the moorings (Fig. 2.8a). The spectral peaks and magnitudes at periods longer than 30 days are almost the same among 2500-m, 4000-m, and near-bottom depths at M1. Coherences between these depths are much higher than the 95% confidence level at almost all periods longer than 10 days. These suggest that meso-scale eddies having nearly uniform amplitude and large coherence at depths greater than 2500 m are dominant at M1.

Meso-scale variations over the periods of 50 to 90 days are strikingly dominant near the bottom at M4, being more predominant than those at M1 (Fig. 2.8d). The variations may be due also to meso-scale eddies at M4. The power spectral density of the near-bottom current at M5 is depressed between 40 and 100 days (Fig. 2.8e). This contrasts with the meso-scale characteristics at M4, although M4 and M5 are close together. The limited meso-scale variability at M5 may be due to the fact that the variations at M5 are associated with the small anticyclonic gyre steered by the seamounts, not meso-scale eddies. The power spectrum at 4000-m depth at M5 has a shape similar to that of the near-bottom one, although it is much weaker. This shows that the variations at M5 are trapped to the bottom, probably by topographic control of the seamounts.

The power spectrum at 4000-m depth at CP is as weak as that at 4000-m depth at M5 (Fig. 2.8f). The similar energy levels are understandable, since M5 and CP are close to each other. However, the shapes of their power spectra differ markedly from each other. While the power spectrum at M5 is depressed between 40 and 100 days, that at CP is nearly uniform at periods longer than 40 days and decreases sharply from 40 days to 20 days. The power spectra at CP

may be composed of the meso-scale variations at M4 and longer-scale variations at M5.

2.5. Conclusion

The present results indicate that the deep-circulation current at 33°N, 165°E is strong and northwestward with a mean speed of 7.8 cm s^{-1} near the bottom, is very stable in the current direction, and continues for four to six months between interruptions of one or two months' duration. Expansion or shift to 31°N, 165°E of the deep-circulation current occurs intermittently. On the other hand, the deep-circulation current was not recorded, but meso-scale eddy variations were prominent, at 35°N, 165°E. The deep-circulation current does not reach 35°N, 165°E, although it shifts northward.

The current at 27°N, 165°E has a high east-northeastward mean velocity of 3.13 cm s^{-1}, 75°T with relatively high direction stability near the bottom, while it has a much lower velocity at 4000-m depth. The shapes of the power spectra of these current velocities strikingly contrast with those at neighboring moorings in that the power spectral densities are depressed between 40 and 100 days. The bottom-confined current at 27°N, 165°E may be part of the anticyclonic small gyre immediately east of the deep seamounts extending northeastward from the Mid-Pacific Seamounts as mentioned in Chapter 3.

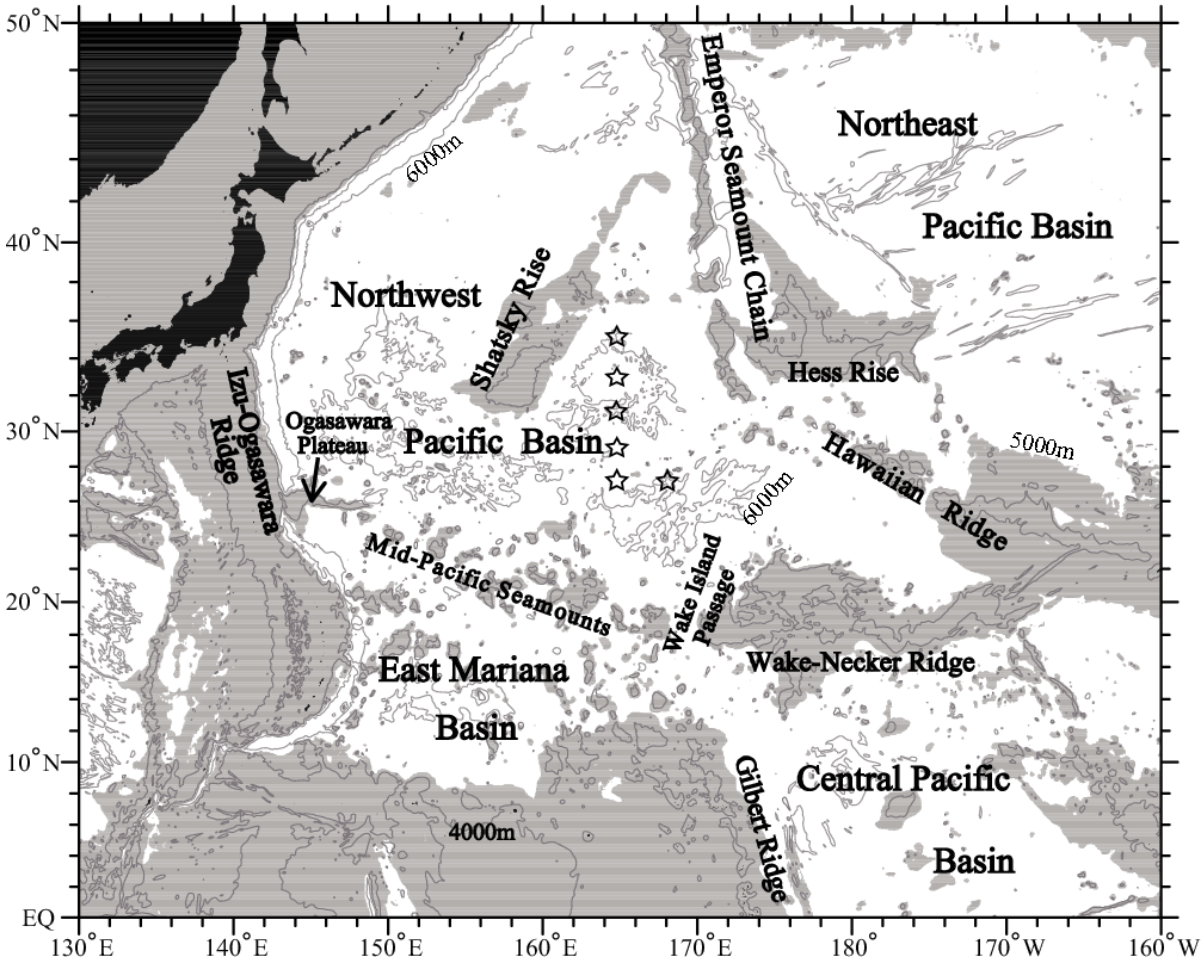

Fig. 2.1 Map of the western North Pacific. Regions less than 5000-m depth are shaded. Lines show isobaths of 4000 m and 6000 m. Stars show positions of five moorings at 165°E and one mooring at 27°N, 168°E in the present study.

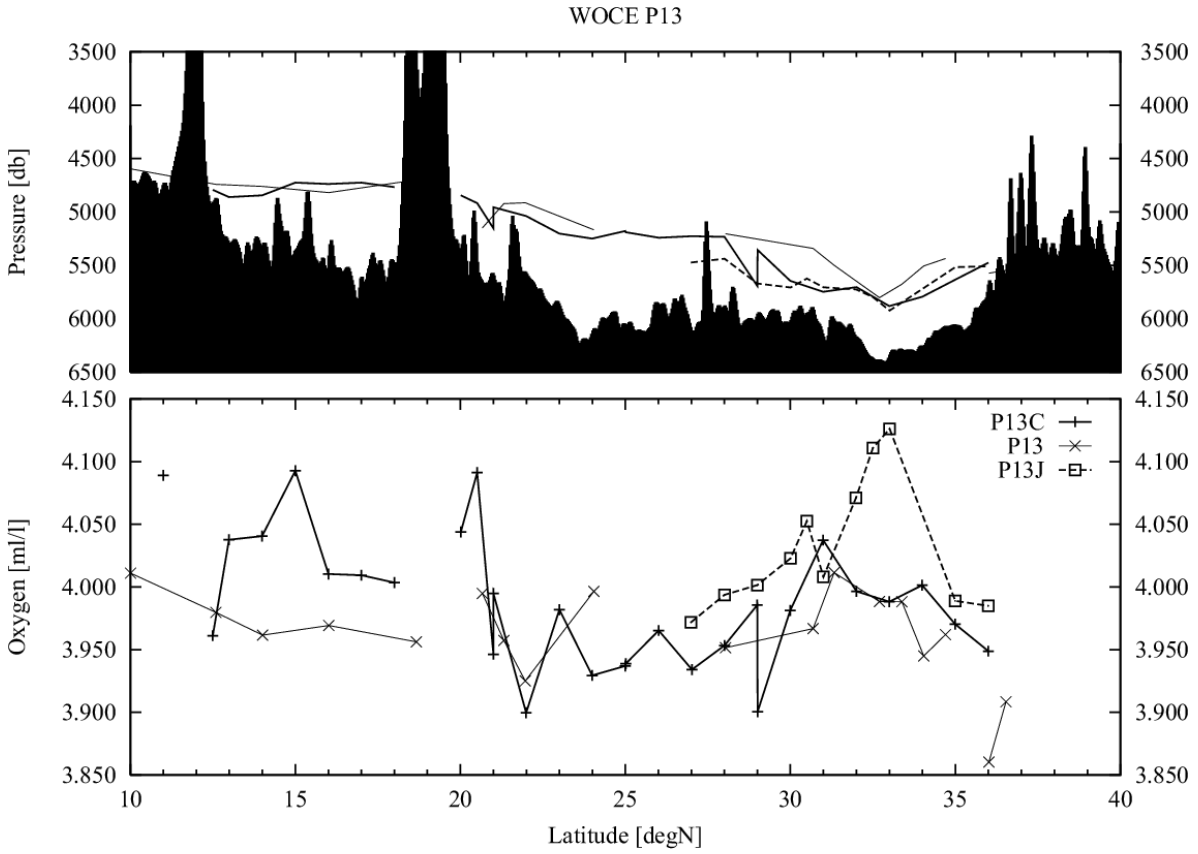

Fig. 2.2 Pressure in db (upper panel) and dissolved oxygen concentration in ml l^{-1} (lower panel) on the 50.17σ_5 isopycnal surface along 165°E, shown by thick solid lines for WHP P13C in 1991, thin solid lines for P13 in 1992, and broken lines for P13J in 1993. Data points are marked in the lower panel by pluses (+), crosses (x), and squares (□) for P13C, P13, and P13J, respectively.

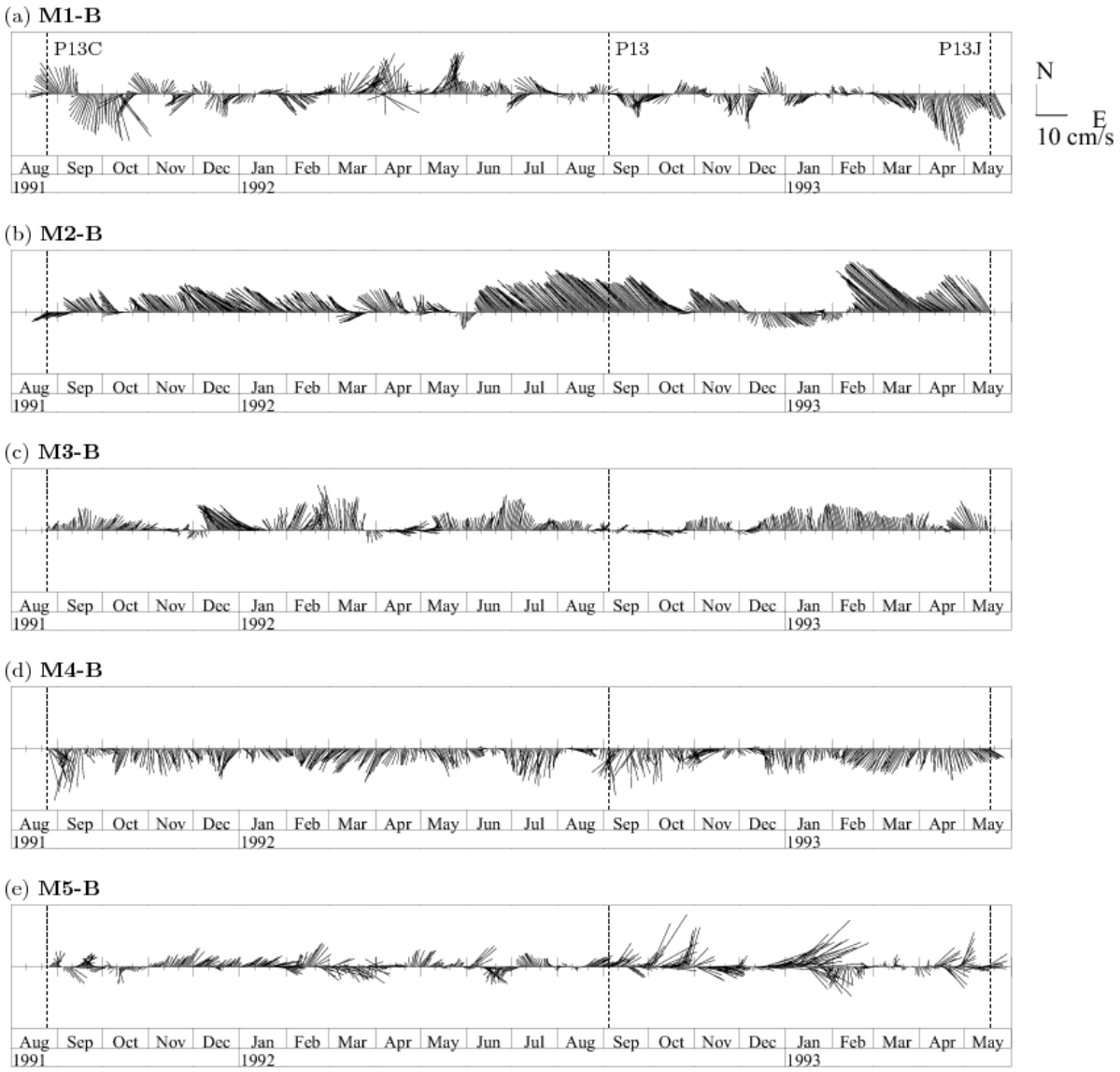

Fig. 2.3 Stick diagrams of daily velocity near the bottom from August 1991 to May 1993 at M1 (a), M2 (b), M3 (c), M4 (d), and M5 (e). Three vertical broken lines in the panels show the dates of hydrographic surveys at WHP P13C, P13, and P13J.

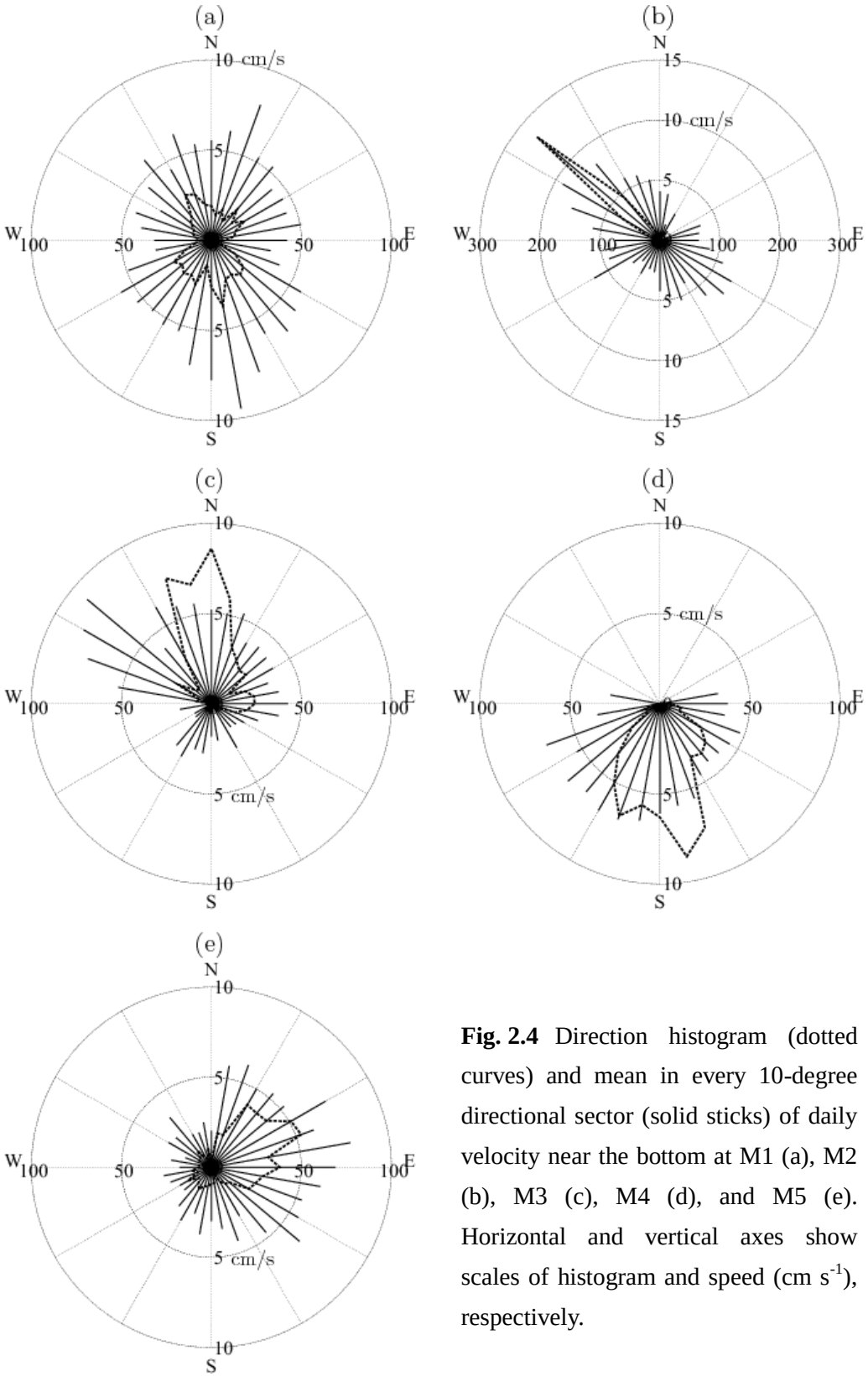

Fig. 2.4 Direction histogram (dotted curves) and mean in every 10-degree directional sector (solid sticks) of daily velocity near the bottom at M1 (a), M2 (b), M3 (c), M4 (d), and M5 (e). Horizontal and vertical axes show scales of histogram and speed (cm s^{-1}), respectively.

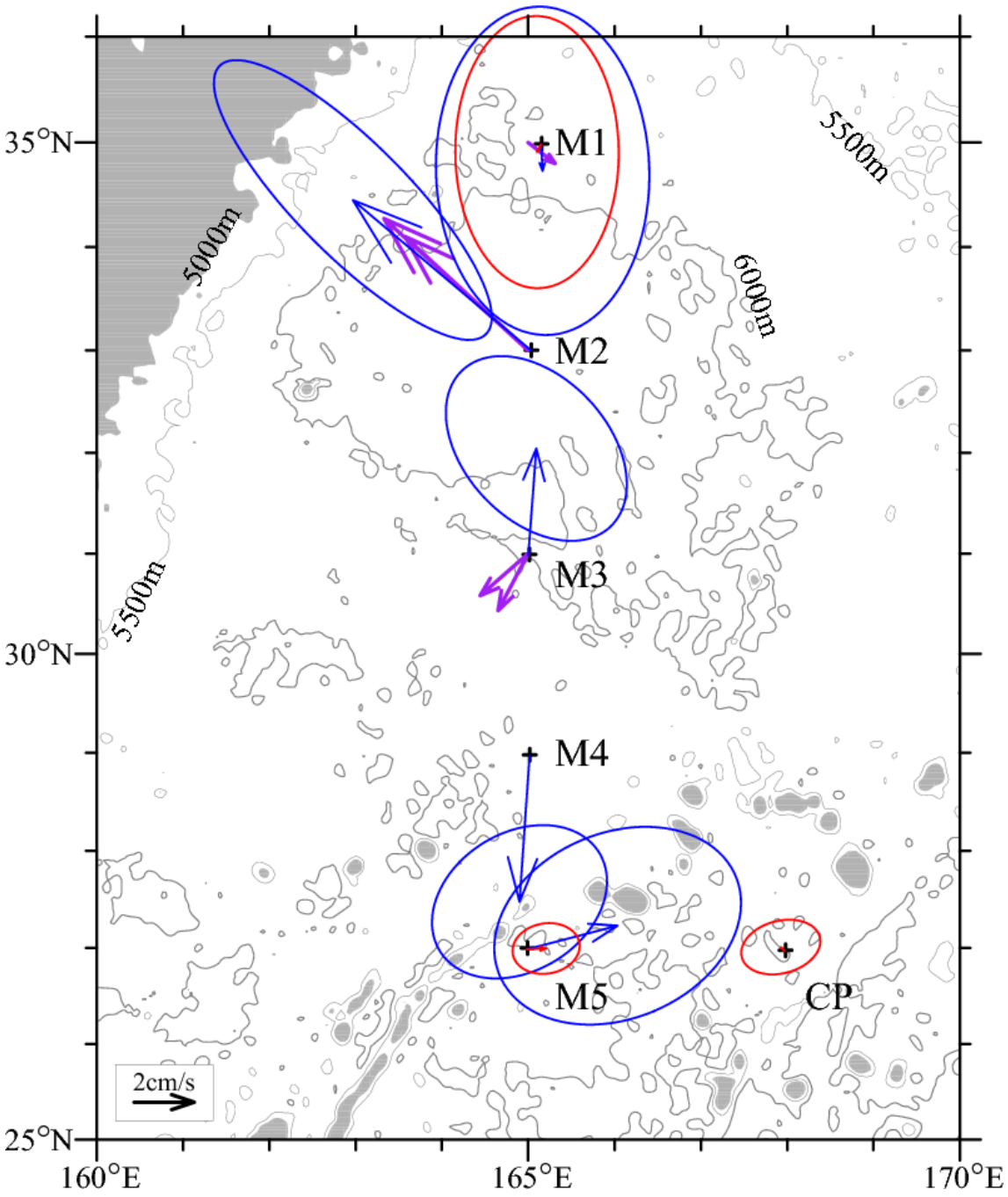

Fig. 2.5 Mean current velocity vectors (arrows) and variance ellipses. Blue and red arrows and ellipses show those near the bottom and at 4000-m depth in the present observations, respectively. Purple ones show those at 4000-m depth for two one-year mooring periods of 1983–1984 and 1984–1985 by Schmitz (1987). Regions shallower than 5000 m are shaded, and isobaths of 5500 m and 6000 m are shown by thin and thick lines, respectively.

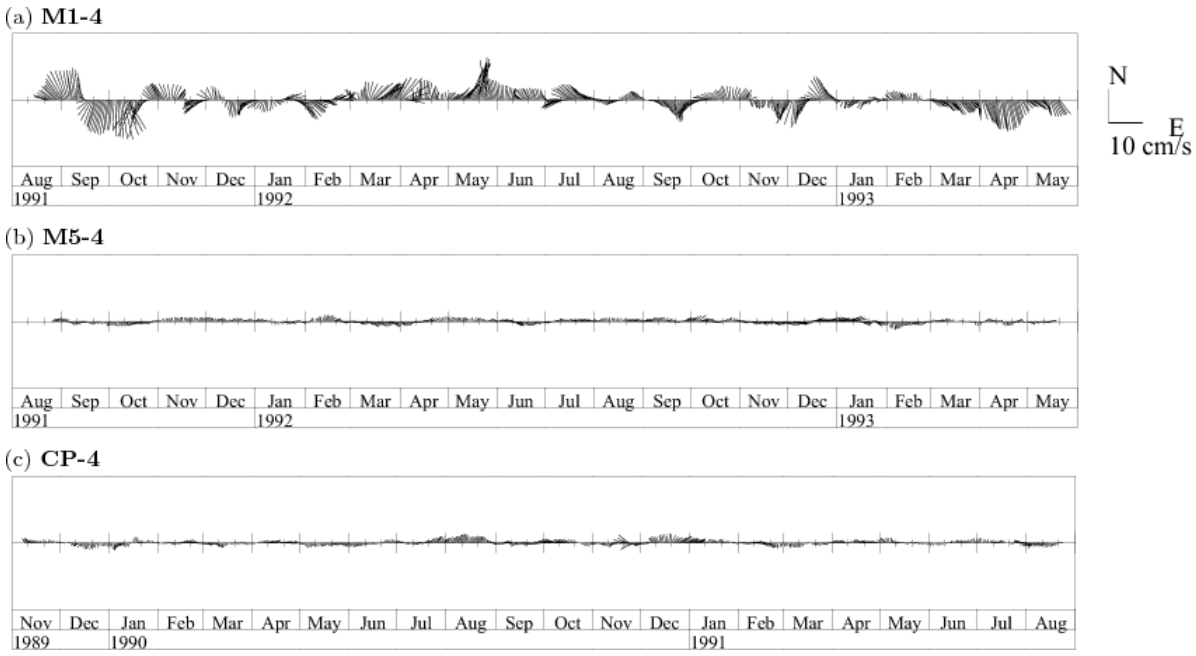

Fig. 2.6 Stick diagrams of daily current velocity at a depth of approximately 4000 m at M1 (a), M5 (b), and CP (c). The velocities were recorded between August 1991 and May 1993 in (a) and (b), and between November 1989 and August 1991 in (c).

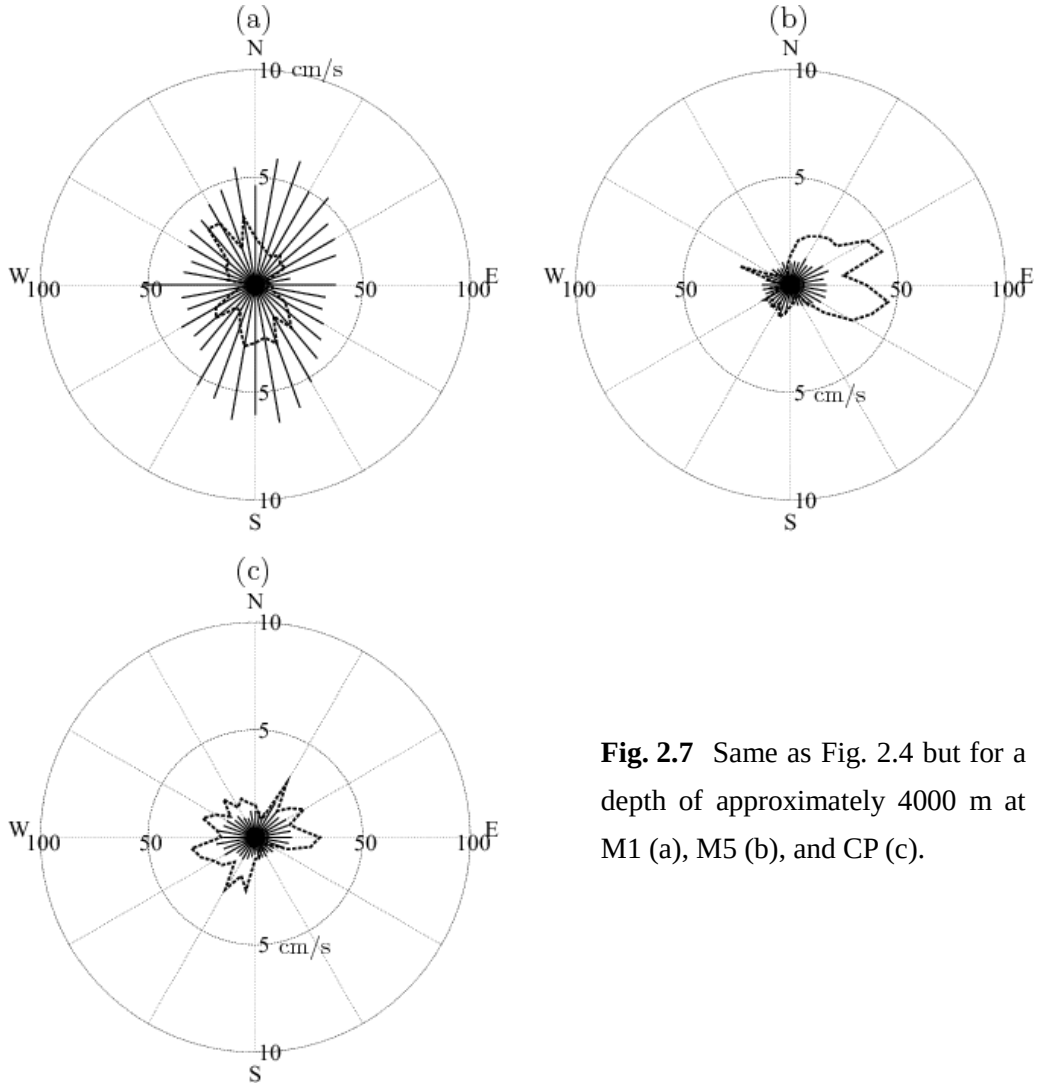

Fig. 2.7 Same as Fig. 2.4 but for a depth of approximately 4000 m at M1 (a), M5 (b), and CP (c).

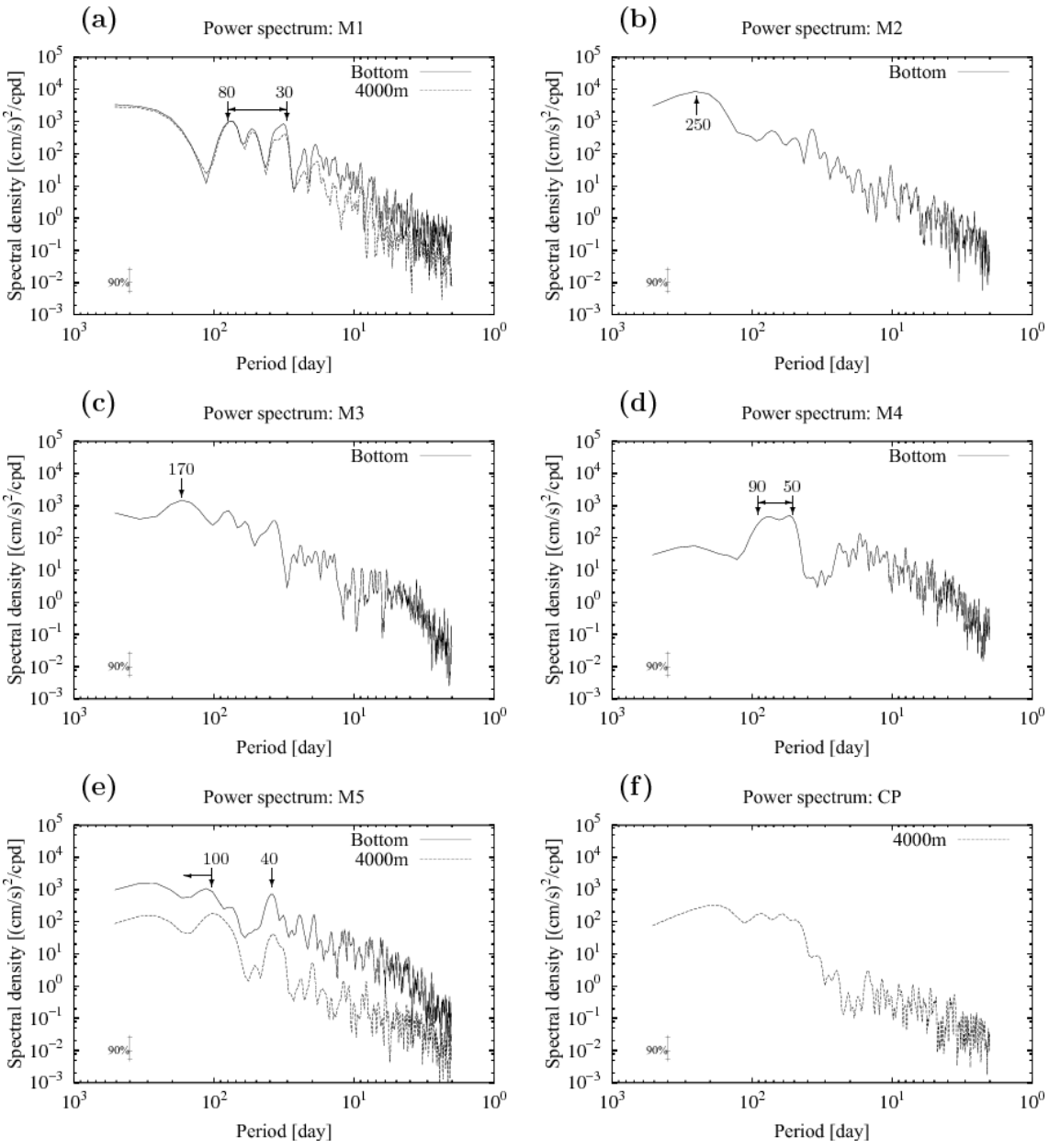

Fig. 2.8 Power spectral densities of major axis components of current velocity variations near the bottom (solid line) and at a depth of approximately 4000 m (broken line) at M1 (a), M2 (b), M3 (c), M4 (d), M5 (e), and CP (f).

Table 2.1 Statistics of time series of daily current velocities from each instrument at 4000-m and near-bottom depths shown with suffixes “4” and “B” in record IDs, respectively. Standard errors of mean current speeds are shown after plus-minus signs. $|\bar{\mathbf{u}}|/\overline{|\mathbf{u}|}$ is the ratio of vector velocity mean to scalar velocity mean, and indicates current direction stability.

Record ID	Mooring depth (m)	Record length (day)	Mean current		Major axis of variance (°T)	$\frac{\lvert\overline{\mathbf{u}}\rvert}{\overline{\lvert\mathbf{u}\rvert}}$
			Speed (cm/s)	Dir. (°T)		
M1, 34°59.3'N, 165°09.3'E, Water depth 5858m, from 22 Aug. 1991 to 21 May 1993						
M1-4	3930	639	0.30 ± 1.13	208	179	0.06
M1-B	5830	639	0.89 ± 1.38	177	178	0.15
M2, 33°00.1´N, 165°02.3´E, Water depth 6213m, from 24 Aug. 1991 to 19 May 1993						
M2-B	6180	635	7.77 ± 1.83	310	135	0.87
M3, 30°59.5´N, 165°00.9´E, Water depth 6051m, from 24 Aug. 1991 to 18 May 1993						
M3-B	6020	634	3.57 ± 0.61	4	137	0.72
M4, 28°58.7´N, 165°01.1´E, Water depth 5792m, from 25 Aug. 1991 to 17 May 1993						
M4-B	5760	632	4.88 ± 0.37	184	58	0.85
M5, 26°59.9´N, 164°59.6´E, Water depth 5785m, from 26 Aug. 1991 to 16 May 1993						
M5-4	4050	630	0.64 ± 0.27	88	81	0.45
M5-B	5750	630	3.13 ± 0.61	75	67	0.62
CP, 26°58.5´N, 167°58.9´E, Water depth 5879m, from 9 Nov. 1989 to 24 Aug. 1993						
CP-4	3820	654	0.18 ± 0.23	318	75	0.12

Chapter 3. Pathways of the deep-circulation currents in the southern part of the Northwest Pacific Basin

3.1. Introduction

The deep-circulation current transporting the oxygen-rich deep water from south, Lower Circumpolar Deep Water (LCDW), is found to flow north-northwestward at the Wake Island Passage (Kawabe et al., 2005) and northwestward at 33°N, 165°E (Chapter 2). In order to clarify its pathway, we will examine the deep dissolved-oxygen distribution north of 20°N in this chapter.

The pathway of the deep water circulation has been studied conventionally with tracing the distinguishing feature of high dissolved oxygen of LCDW. Mantyla and Reid (1983) drew an oxygen map near the bottom in the world ocean. They indicate that there is a tongue of high oxygen extending eastward to the Northeast Pacific Basin near Midway Island (the western end of the Hawaii Ridge) (see Fig. 1.1) and that this would be one of the routes of LCDW entering the Northeast Pacific Basin. However, this route remains a matter of examining because their map is based on sparse data which might have been all available at that time. Kawabe (1993) compiled denser oxygen data in the western North Pacific, which was accumulated after Mantyla and Reid (1983). His oxygen map on an isopycnal at approximately 4000 dbar shows the western branch of the deep circulation but not the eastern branch. Oxygen map near 5000 dbar should be drawn to present the deep-circulation current passing through the Wake Island Passage (Kawabe and Taira, 1995). At the present day, high-resolution and high-quality oxygen data have been accumulated since World Ocean Circulation Experiment (WOCE). In the present study, the eastern branch is examined with oxygen maps below 5000 dbar.

3.2. Data and method

We used WOCE Hydrographic Programme (WHP) data (P03 at 24°N, P02T at 30°N, and P14N at 179°E) and hydrographic data obtained on the R/V Hakuho-maru cruises KH-91-5 (WHP P13C), KH-95-1, KH-99-1, KH-03-1, KH-04-4, KH-05-4, and KH-07-1 (Kawabe, 1996, 2005a, 2005b, 2006) (Fig. 3.1). Dissolved oxygen concentrations measured with a conductivity-temperature-depth-oxygen profiler ($CTDO_2$) were used except for WHP P03. For WHP P03, oxygen data at one-decibar intervals were obtained by interpolating water sample oxygen data with the Akima method. Near-bottom oxygen was calculated by averaging oxygen data taken 100 m from the bottom, whose depth was estimated with the NOAA National Geophysical Data Center data set with a 2′ latitude-longitude resolution, usually called

ETOPO2.

Water-property data have some gaps among hydrographic sections, as Johnson et al. (2001) pointed out. Such gaps would include measurement bias and long-term variations. Since they should be removed to determine synoptic water-property distribution, we adjusted oxygen and salinity values obtained at WHP P03, P02T, KH-99-1, part of KH-04-4 (12°40′N, the Wake Island Passage–south of the Shatsky Rise), and KH-07-1 to those of KH-91-5 (WHP P13C), using values near cross points on an isothermal surface having a potential temperature (θ) of 1.20°C. The adjusted values of WHP P02T were used for adjustment of the observed values of KH-95-1 and part of KH-04-4 (32°30′N, Shatsky Rise–Izu Ridge). The adjusted values of WHP P03 were used for the adjustment of WHP P14N. We did not make any adjustments for KH-03-1, which does not cross any other sections. In accordance with the method of Johnson et al. (2001), the adjustment values for salinity were added to the original data, and those for oxygen were multiplied by the original data. The adjustment values for each section are listed in Table 3.1. We drew oxygen contours on the near-bottom using 414 data points and those on 50.17σ_5 isopycnal surface using 439 data points, after several data points were omitted because their oxygen values are extremely large or small among their surrounding points in comparison with contour intervals.

3.3. Pathways of the deep-circulation current and dissolved oxygen distributions

The near-bottom oxygen distribution in Fig. 3.2 shows that high-oxygen water in the Central Pacific Basin mainly spreads northward to the Northwest Pacific Basin through the Wake Island Passage. It also spreads westward at 13°–18°N but is almost completely blocked by the seamounts around 163°E. The northward spread forms a north-northeastward high-oxygen tongue immediately north of the Wake Island Passage, which corresponds to the current direction of 35°T at the Wake Island Passage (Kawabe et al., 2005). The high-oxygen tongue turns cyclonic and reaches 169.5°–173°E at 24°N, as seen in Roemmich et al. (1991), 168°–169°E at 30°N, and immediately south of the Shatsky Rise.

Integrating the results of high-oxygen distribution and current properties at CP at 168°E and M1–M5 at 165°E in Chapter 2 shows the following pathway of the deep-circulation current in the southern part of the Northwest Pacific Basin. First, it proceeds northward in the Central Pacific Basin and passes the Wake Island Passage north-northeastward. Then, it passes 24°N at 169.5°–173°N and 27°N around 170°E east of mooring CP. Furthermore, it passes 165°E around 33°N northwestward with meridional variations in the region between north of 30°N and immediately south of 35°N at 165°E. Last, it reaches south of the Shatsky Rise. Thus, the deep-circulation current forms a cyclonic pathway in the deep basin surrounded by the

Wake-Necker Ridge, the Emperor Seamount Chain, and the Shatsky Rise.

The oxygen distribution on the $50.17\sigma_5$ isopycnal surface (about 5000–6000db) shows that high oxygen, >4.00 ml l^{-1}, is confined to the region west of 170°–171°E at 12°–20°N, west of 179°E between the Wake-Necker Ridge and the Hawaiian Ridge, and south of 34°N between the Shatsky Rise and the Hawaiian Ridge (Fig. 3.3). This suggests that the deep-circulation current does not bifurcate into an eastward flow in the basin north of the Wake Island Passage, nor does it flow between the Hess Rise and the Hawaiian Ridge into the Northeast Pacific Basin.

The oxygen distribution on the $50.17\sigma_5$ isopycnal surface also shows that part of the deep-circulation current passing 163°–165°E at 18°20´N, as indicated by Kawabe et al. (2003), proceeds to 20°–21°N, 165°E anticyclonically and probably joins the main part of the deep-circulation current passing the Wake Island Passage (Fig. 3.3). Moreover, the contour of 3.96 ml l^{-1} suggests that an anticyclonic small gyre exists with the center at 25°N, 165°E. This is consistent with the velocity record at mooring M5 at 165°E shown in Chapter 2. The east-northeastward bottom-confined current at M5 may form the anticyclonic small gyre immediately east of the seamounts extending from the Mid-Pacific Seamounts, probably because of the influence of bottom topography. Thus, the deep-circulation current does not seem to flow westward along the north of the Mid-Pacific Seamounts.

Kawabe (1993), using a map of dissolved oxygen on the $41.52\sigma_3$ isopycnal at a depth of approximately 4000 m, showed that the western branch current of the deep-circulation flows northward in the East Mariana Basin. This is not clearly shown in Fig. 3.3, because the isopycnal surface of $50.17\sigma_5$ used in Fig. 3.3 is too deep to detect the western branch current. However, a northwestward extension of the high-oxygen tongue (>4.08 ml l^{-1}) from around 18°N, 155°E to the south of the Ogasawara Plateau and relatively high oxygen east of this plateau support the pathway of the western branch current inferred by Kawabe et al. (2003). Moreover, relatively high oxygen around the low-oxygen tongue extending from 12°N, 147°E to 18°N, 150°E supports the conclusion of Kawabe et al. (2003) that part of the western branch current turns south at the seamounts extending zonally around 20°N, 150°E.

3.4. Conclusion

From the characteristics of current velocity and deep dissolved oxygen distributions, we specified pathways of the deep-circulation current in the southern part of the Northwest Pacific Basin (Fig. 3.4). The deep-circulation current passing mainly through the Wake Island Passage (a thick black arrow in Fig. 3.4) and partially through gaps at 163°–165°E (a thin black arrow in Fig. 3.4) flows northward at 24°N, 169.5°–173°E and at 30°N, 168°–169°E, proceeds

northwestward around 33˚N, 165˚E, and goes westward through the south of the Shatsky Rise. Thus, the deep-circulation current forms a cyclonic pathway in the deep basin surrounded by the Wake-Necker Ridge, the Emperor Seamount Chain, and the Shatsky Rise. We did not find that the deep-circulation current proceeded eastward in the region between the Hess Rise and the Hawaiian Ridge toward the Northeast Pacific Basin. This is confirmed also from the vertical section of dissolved oxygen along WHP P02 at 30°N; the deep dissolved-oxygen values to the east of 180° is much different from those to the west of 180° (Fig. 3.5). The wrong suggestion of a deep-water pathway through this region by Mantyla and Reid (1983) may be due to coarse data points in their map. Relatively oxygen-rich water found to the north of the Hawaiian Ridge would come from the east as part of the deep-circulation current in the Northeast Pacific Basin (Komaki and Kawabe, 2009; Kato and Kawabe, 2009).

The current axis of the eastern branch seems to pass through the deepest parts in the basin surrounded by the Wake-Necker Ridge, the Emperor Seamount Chain, and the Shatsky Rise. The vertical section of dissolved oxygen along WHP P02 at 30°N has a deep maximum core ranging from the deepest part to the eastern bottom slope (Fig. 3.5). The northwestward deep-circulation current passes the mooring M2 at 33°N, 165°E, which is in the vicinity of the deepest part (Fig. 3.6). It is interesting that the eastern branch does not flow along a western boundary but through the deepest part across isobaths.

The deep dissolved oxygen distributions confirmed the pathway of the western branch current and its partial turn to the south concluded by Kawabe et al. (2003), and suggested the pathway shown by a thick green arrow in Fig. 3.4.

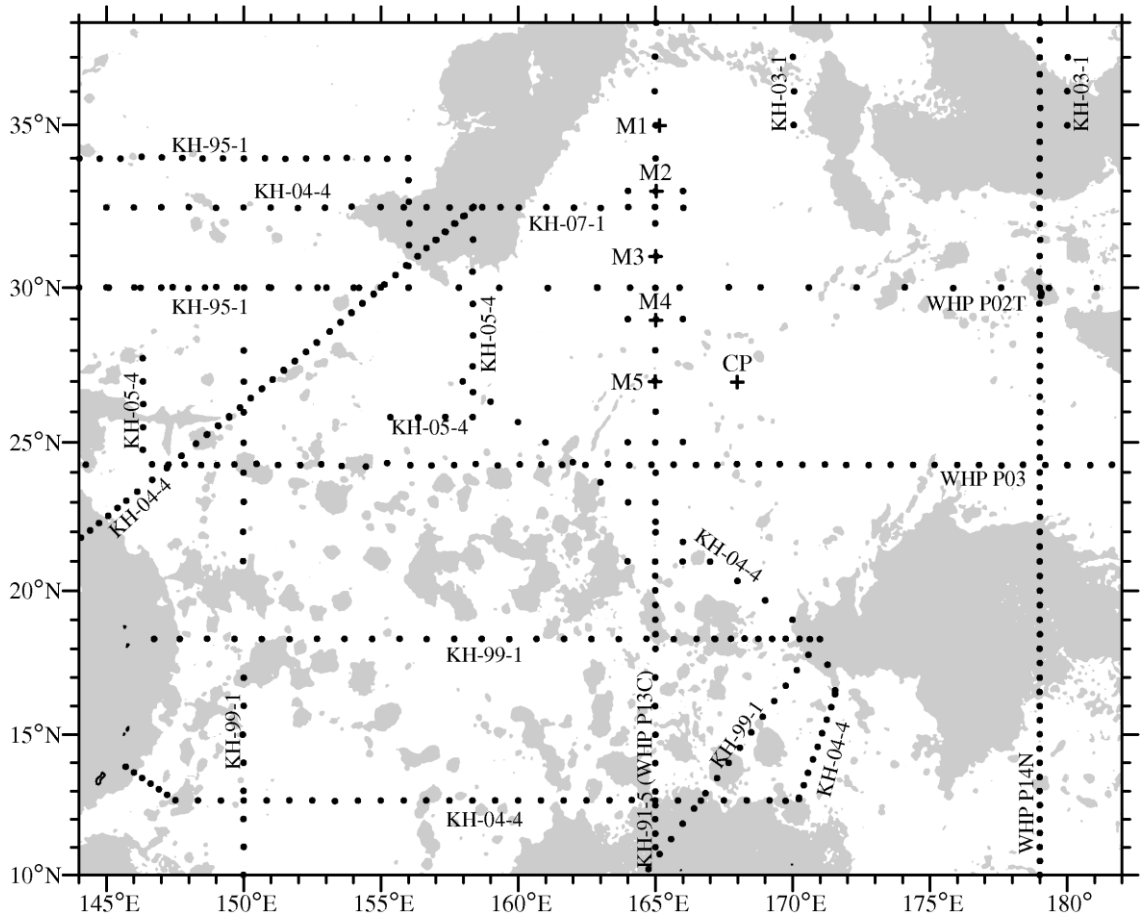

Fig. 3.1 Location of hydrographic stations used for mapping dissolved oxygen (dots). Pluses show the moorings of M1–M5 at 165°E and CP at 27°N, 168°E in Chapter 2. Regions shallower than 5000 m are shaded.

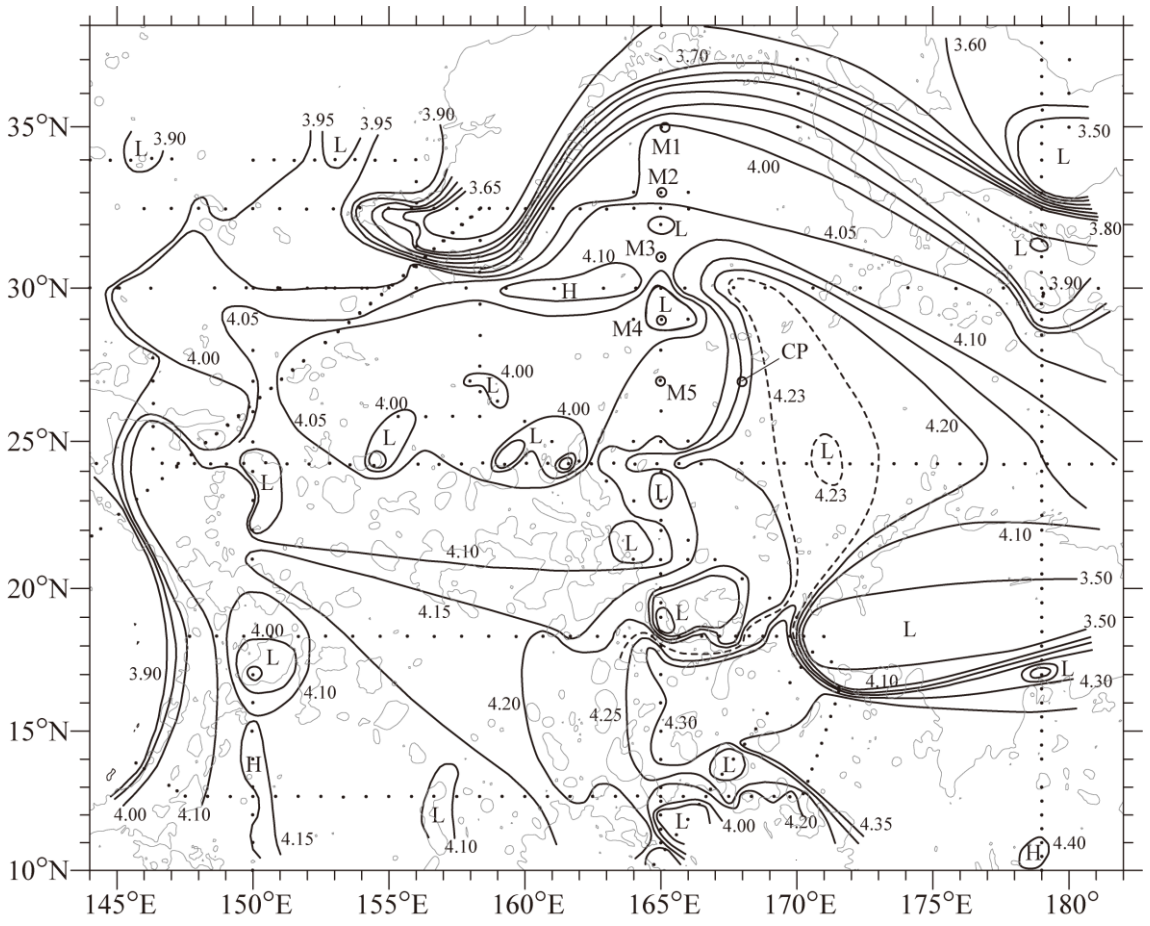

Fig. 3.2 Horizontal distribution of dissolved oxygen concentration (ml l^{-1}) near the bottom in the western subtropical region of the North Pacific. The contour interval is 0.05 ml l^{-1}. Contours of 4.23 ml l^{-1} are drawn by broken lines. Hydrographic stations used for this contour drawing are shown by dots. Thin lines are isobaths of 5000 m.

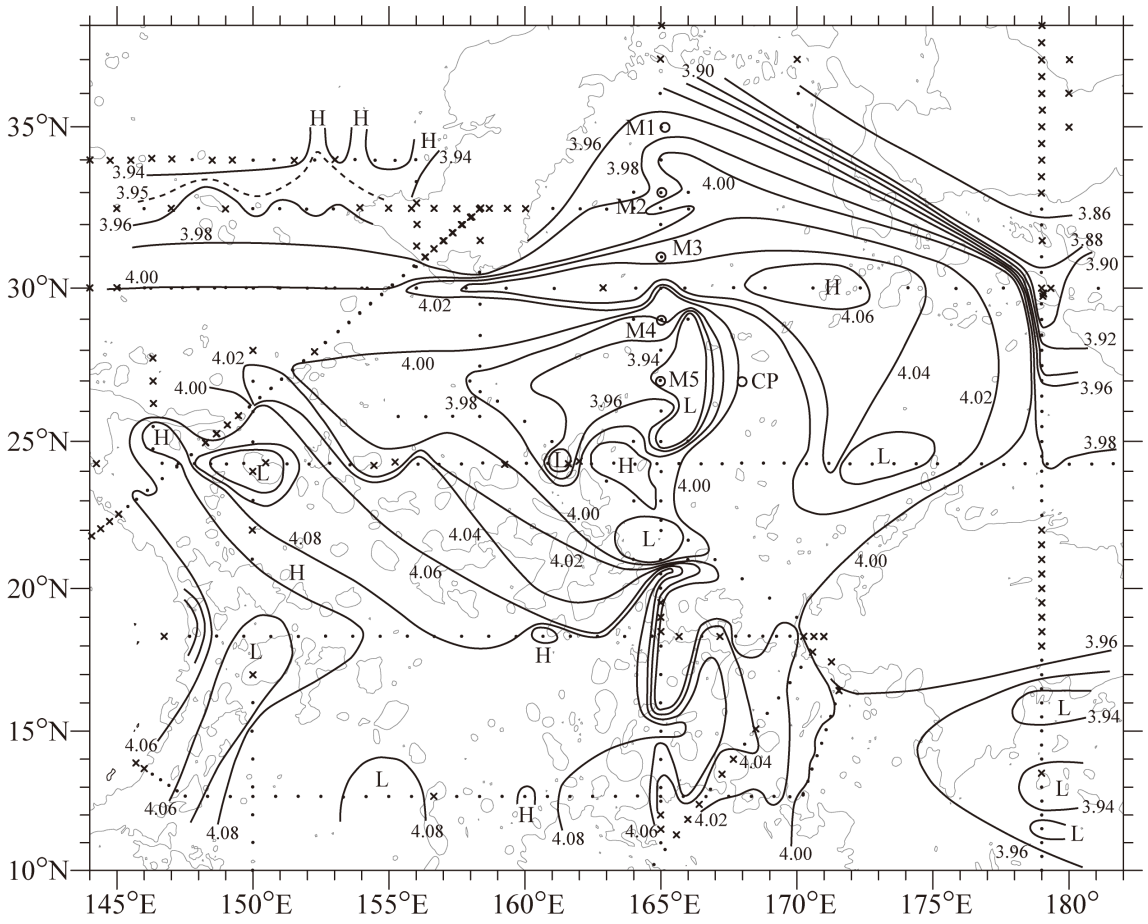

Fig. 3.3 Horizontal distribution of dissolved oxygen (ml l^{-1}) on the 50.17σ_5 isopycnal surface in the western subtropical region of the North Pacific. The contour interval is 0.02 ml l^{-1}. Contours of 3.95 ml l^{-1} are drawn by broken lines. Hydrographic stations used for this contour drawing are shown by dots, and those at which water with 50.17σ_5 was not present are shown by crosses. Thin lines are isobaths of 5000 m.

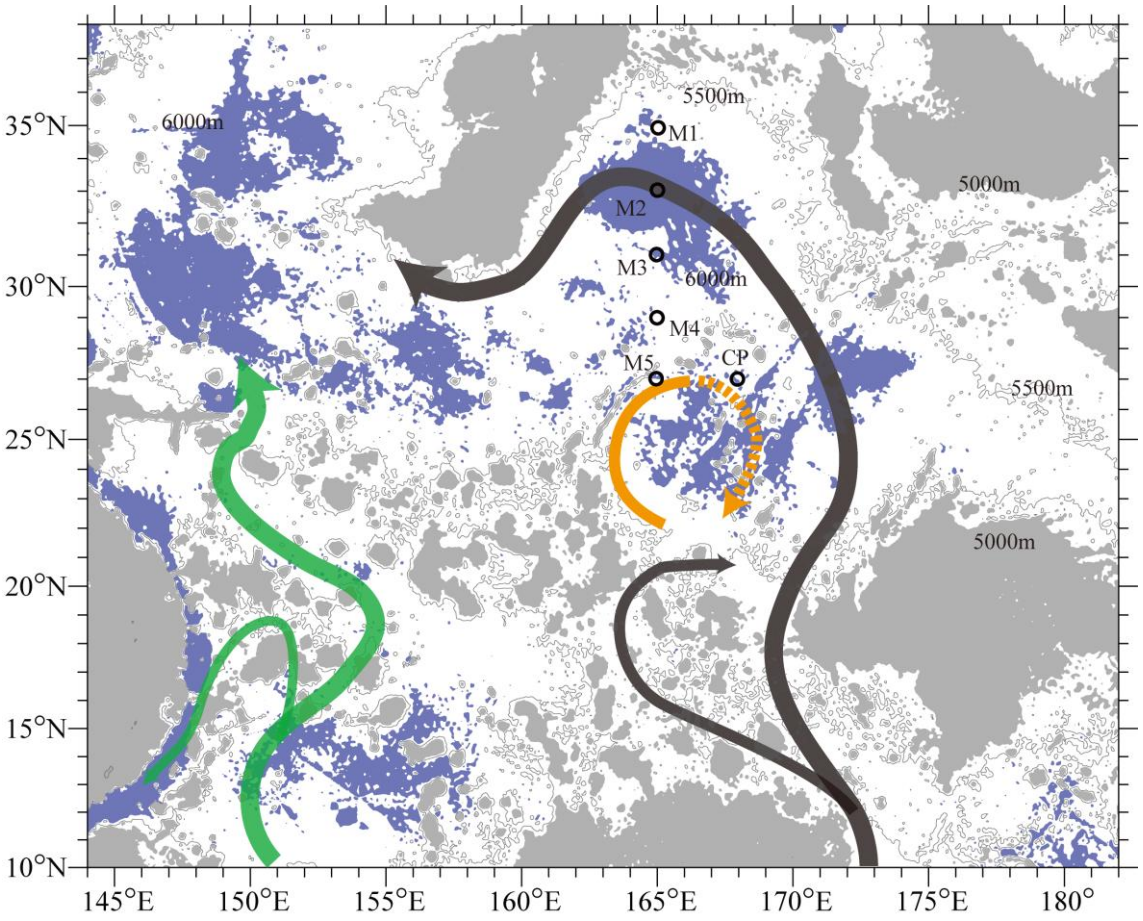

Fig. 3.4 Schematic of the deep currents in the western subtropical region of the North Pacific. The deep-circulation current is shown by black arrows, the western branch current of the deep circulation is shown by green arrows, and the anticyclonic small gyre around 25°N, 165°E is shown by an orange arrow. Regions less than 5000 m depth and more than 6000 m depth are colored gray and blue, respectively.

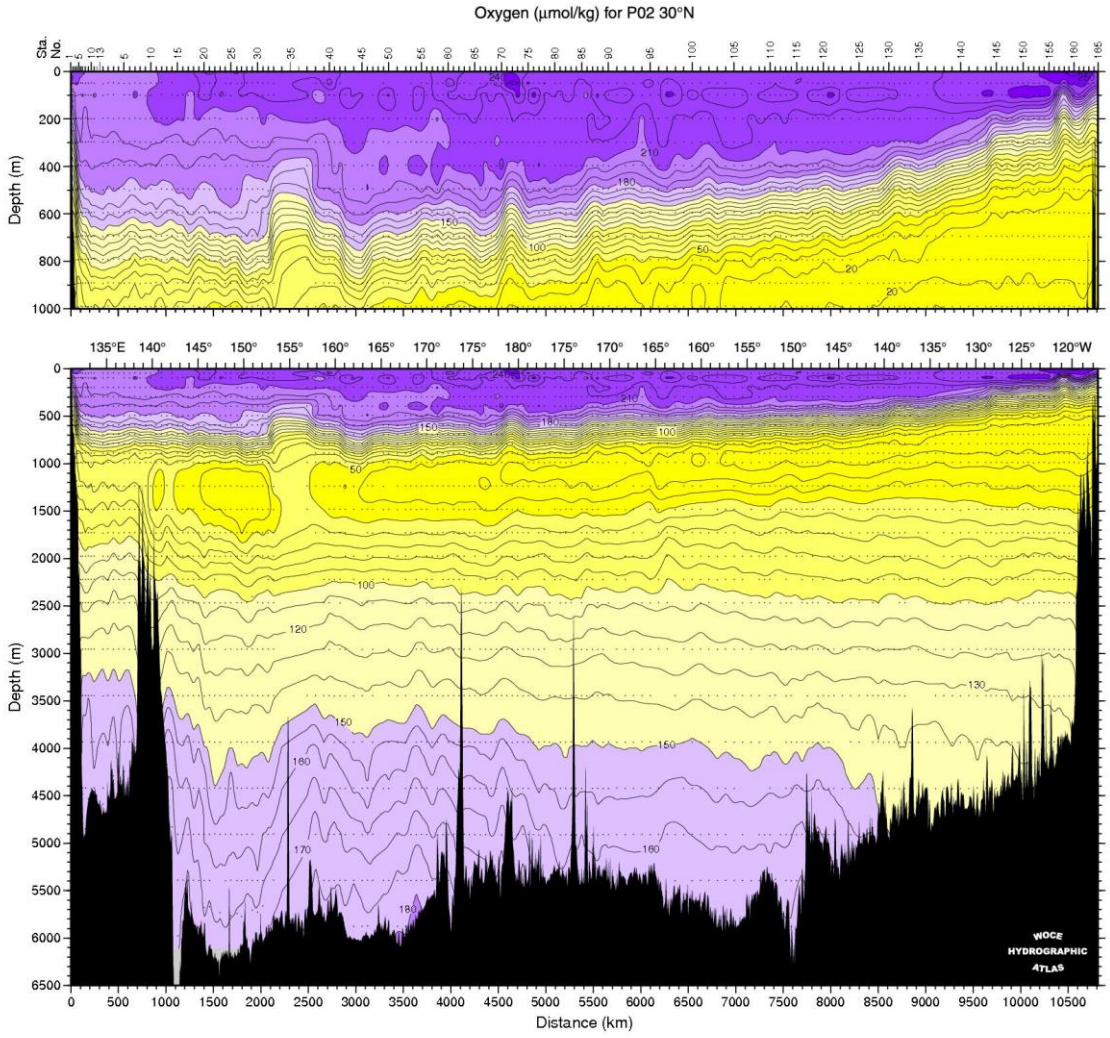

Fig. 3.5 A vertical section of dissolved oxygen along 30°N in the North Pacific (Talley, 2007).

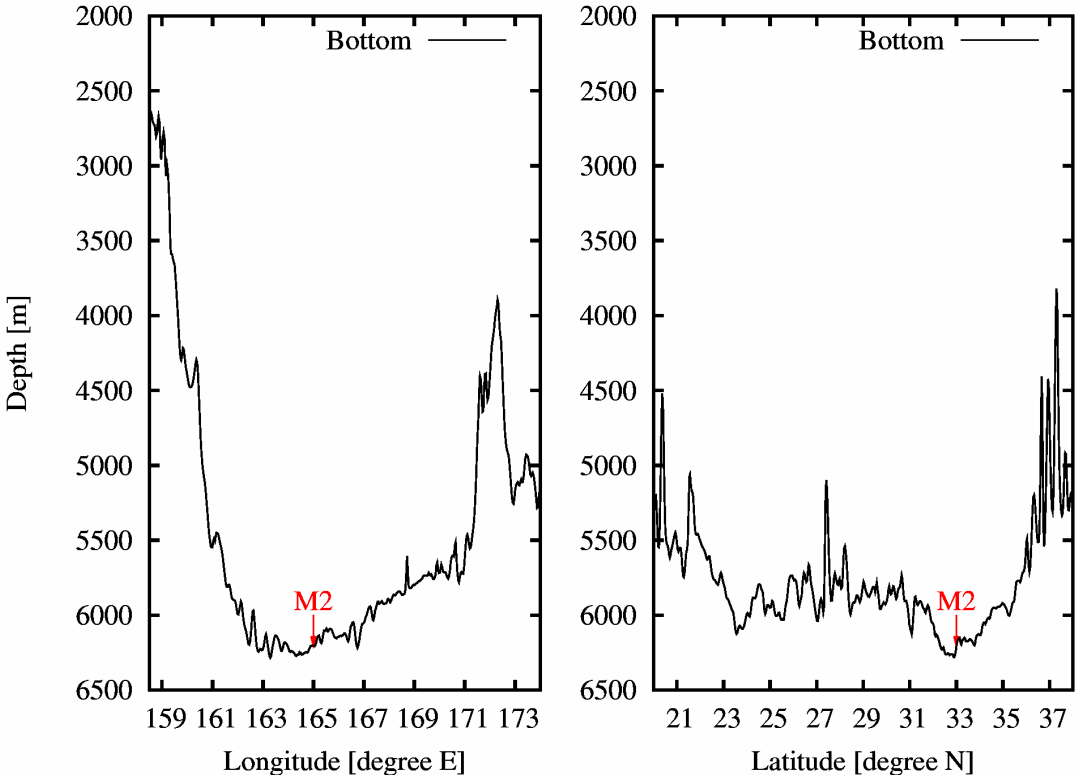

Fig. 3.6 The zonal (left) and meridional (right) sections of the bottom topography along 33°N and along 165°E, respectively. The bottom topography is based on ETOPO2. The position of mooring M2 at 33°N, 165°E is shown by red arrows.

Table 3.1 Adjustments of oxygen and salinity to remove gaps among hydrographic sections. The adjustment values for oxygen are rates to be multiplied by the original data for correction, and those for salinity are differences to be added to the original ones. Sections of KH-04-4 were divided by cruise leg, because the observation areas of the northwestern (leg 1) and southern (leg 2) regions are markedly separated as shown in Fig. 3.1.

Section	Oxygen	Salinity
WHP P02T	1.0215	–0.0017
WHP P03	1.0094	0.0053
WHP P14N	1.0147	0.0032
KH-95-1	1.0100	0.0023
KH-99-1	1.0030	–0.0039
KH-04-4 leg 1	1.0187	0.0012
KH-04-4 leg 2	1.0071	–0.0002
KH-05-4	1.0236	0.0010
KH-07-1	1.0098	0.0005

Chapter 4. Temporal and spatial characteristics of current velocities and volume transports of deep-circulation currents measured southwest of the Shatsky Rise

4.1. Introduction

As a part of the global deep circulation, the saline, oxygen-rich, cold Lower Circumpolar Deep Water (LCDW) is transported northward in the South Pacific by a deep western-boundary current, entering the Central Pacific Basin mainly through the Samoan Passage. The LCDW then spreads farther to the Northwest Pacific Basin, the Northeast Pacific Basin, and the East Mariana Basin (Mantyla and Reid, 1983). Because of the complex bottom topography at low latitudes of the western Pacific, the LCDW is transported to the Northwest Pacific Basin by two branches of a deep-circulation current (Johnson and Toole, 1993; Kawabe et al., 2003). The deep part of this deep-circulation current forms the eastern branch, flowing northward along the Gilbert Ridge toward the Wake Island Passage with a volume transport of 8.1 Sv (1 Sv = 10^6 m^3 s^{-1}), whereas the shallow part forms the western branch flowing into the Melanesian and East Mariana basins with a volume transport of 2–6 Sv (Johnson and Toole, 1993; Kawabe, 1993; Kawabe and Taira, 1995; Kawabe et al., 2003; Kawabe et al., 2006).

The eastern branch partly separates eastward immediately north of 10°N in the Central Pacific Basin (Kato and Kawabe, 2009) and the remaining part proceeds northward into the Northwest Pacific Basin through the Wake Island Passage and adjacent gaps in the Mid-Pacific Seamounts with a volume transport slightly more than 4 Sv (Kawabe et al, 2003, 2005). The latter turns cyclonically in the small basin surrounded by the Shatsky Rise, the Emperor Seamount Chain, and the Wake–Necker Ridge, and then flows westward south of the Shatsky Rise as shown in Chapter 3 (Fig. 4.1). On the other hand, part of the western branch enters the Northwest Pacific Basin through gaps in the Magellan Seamounts and the Mid-Pacific Seamounts with a volume transport of 2.1 Sv (Kawabe et al., 2003). Then, it detours around the Ogasawara Plateau, which is an eastward bulge of the Izu-Ogasawara Ridge as inferred by dissolved-oxygen distribution in Chapter 3 (Fig. 4.1). Consequently, both branches would pass through a deep strait (about 950 km width) between the Shatsky Rise and the Ogasawara Plateau.

To the east of Japan at 38°N, Fujio and Yanagimoto (2005) found westward current on the abyssal plain and northward current on the eastern flank of the Japan Trench; volume transport of the latter current exceeds that of southward current on the western flank. Excess of

northward transport is also found above the Izu-Ogasawara Trench at 34°N (Fujio et al., 2000). They pointed out that the existence of the westward current agrees with mooring results of Schmitz et al. (1987) at 152°E and those of Owens and Warren (2001) southeast of Hokkaido Island, and presumed that these westward currents would follow the eastern branch and the northward excess on the Japan Trench would come from the western branch. Examining the deep circulation southwest of the Shatsky Rise is also necessary for knowing the downstream deep circulation in the Northwest Pacific Basin.

We conducted hydrographic and mooring observations along a line located southwest of the Shatsky Rise. Kawabe et al. (2009) analyzed the hydrographic data in 2004 and 2005, and found that the lower deep layer where LCDW with potential temperature (θ) lower than 1.2°C exists is nearly homogeneous. They concluded that geostrophic volume transport carrying LCDW (θ < 1.2°C) in the lower deep layer is slightly less than 4 Sv and slightly more than 2 Sv for the eastern and western branches of the deep-circulation current, respectively. These volume transports are consistent with the previous studies. In their results, the location and volume transport of the branch currents are different between the observations undertaken in 2004 and 2005. This suggests temporal variability in the deep-circulation currents. Marked temporal variability in the deep-circulation currents has been shown with mooring observations by Whitworth et al. (1999) in the western South Pacific, by Rudnick (1997) at the Samoan Passage, and by Kawabe et al. (2005) at the Wake Island Passage. In the present chapter, we analyze the mooring data of current velocity, and document temporal variations in the volume transport of the deep-circulation currents southwest of the Shatsky Rise.

4.2. Mooring observations

We conducted direct current measurements for approximately 14 months at nine moorings (M1–M9) using 50 current meters along the line from M1 (25°42′N, 149°16′E) to M9 (31°13′N, 156°33′E) (Figs. 4.1 and 4.2, Table 4.1). The nine moorings were anchored during the period 15–23 September 2004 in the R/V Hakuho-maru KH-04-4 cruise and were recovered during the period 21 November to 1 December 2005 in the KH-05-4 cruise. We used 30 rotor-type current meters manufactured by Union Engineering Co., Ltd., Japan (equivalent to Aanderaa RCM5), 14 Aanderaa RCM11 Doppler current meters, 5 FSI 3D-ACM acoustic current meters, and 1 RDI 300-kHz Workhorse Doppler current profiler.

For all nine moorings, we installed current meters near the bottom and at depths of approximately 5000, 4500, 4000, and 3500 m. The moorings M1–M3 and M5–M7 were anchored in a deep basin at water depths of 5700–5900 m, and had additional current meters installed at depths of approximately 5500 m. The other moorings were located in shallower

regions: M4 was anchored on a small seamount at a water depth of 5601 m and had an additional current meter installed at 2930 m depth, and M8 and M9 were anchored at water depths of 5112 and 4440 m on the slope of the Shatsky Rise, respectively. The water depths and depths of current meters listed in Table 4.1 were estimated using depth data converted from pressure data measured using Aanderaa RCM11 current meters, based on a Sounders and Fofonoff's method (Fofonoff and Millard, 1983).

Most of the current meters recorded velocity data throughout the full mooring period, while the current meters at 4890 m depth at M3, 5020 and 4500 m depth at M4, 4930 m depth at M5, and 4930 m depth at M6 ceased operating during the mooring period, and the current meter near the bottom at M5 malfunctioned due to a water leak.

Prior to the mooring observations at M1–M9, we deployed two moorings M7p and M8p during the R/V Hakuho-maru KH-03-1 cruise in May 2003; these sites were located 1.8 km northeast of M7 and 2.1 km northwest of M8, respectively. Consequently, the water depth at M8p is nearly 300 m greater than that at M8, although the water depth is similar between M7 and M7p (Table 4.2). The bottom topography around M8p seems to be a small, deep valley according to the sounding with a ship-mounted precision depth recorder (PDR) of the R/V Hakuho-maru.

In the following sections, we analyzed daily current velocities subsampled at midnight (coordinated universal time) after filtering out inertial oscillations and diurnal and semi-diurnal tides using a Gaussian filter equivalent to "gaus24" described by Thompson (1983).

4.3. Velocity field near the ocean bottom

The mean velocity directions below approximately 4000 m depth are within 270°–360°T at M2, M4, and M6–M9, whereas those are toward 65°T, 163°T, and 244°T at M1, M3, and M5, respectively (Tables 4.1 and 4.2). Moreover, the direction of the near-bottom current velocity at M2, M4, and M7–M9 has sharp peaks within the range 270°–360°T in the direction histogram, whereas that at M6 has a dominant peak to the west-southwest, similar to that for M5 (Fig. 4.3).

Because of those velocity characteristics, the vertical section of objectively-mapped mean current velocity component normal to the observation line shows that northwestward velocity components have maximum cores near the bottom at M2, M4, and M8, and the maximum core at M8 expands toward M7 and M9 (Fig. 4.4). Figure 4.4 was drawn through the following processes. The obtained current data were mapped to grids of 100 m depth by 0.1° in latitude (about 17 km) for the northeastward observation line with using the optimal interpolation

method developed by Bretherton et al. (1976). The optimal interpolation was applied with influence radii of 0.5° in latitude, 500 m depth, and a noise level of 0.5 $cm^2\ s^{-2}$. The sizes of the influence radii are similar to the spacings of the current meters, and the noise level is similar to the estimation errors of the mean currents (see Table 4.1).

The pattern of temporal variation in current velocity at M4 is markedly different from that recorded at M2 and M7–M9. The northwestward current near the bottom at M4 (red arrows in Fig. 4.5b) varies significantly between 0 and 20 cm s^{-1} with a period of 45 days, as shown by the marked peak in the power spectrum (Fig. 4.6). This current is strongly intensified near the bottom and is highly stable in its direction (Table 4.1). Since M4 was anchored at a water depth of 5601 m on a small seamount, it may be part of a bottom-intensified clockwise eddy around an isolated seamount located immediately east of M4. The seamount has the top at about 3800 m depth and a horizontal scale of about 20 km (Fig. 4.7). The clockwise eddy is suggested by the geostrophic flow distribution presented by Kawabe et al. (2009).

Based on the above results, we conclude that the western and eastern branches of the deep circulation flow northwestward around M2 near the Ogasawara Plateau and at M7–M9 near the Shatsky Rise.

The eastern branch is almost shown as a current flowing toward 270°–360°T in the stick diagrams for M7–M9 and M7p–M8p (Fig. 4.5). The current toward 270°–360°T at M8-B (M8p-40) makes up 77% (80%) of the total daily record, while that at M7-B (M7p-B) and M9-40 accounts for 60% (67%) and 62%, respectively. According to the ratio of the vector mean to the scalar mean of each velocity ($|\bar{\mathbf{u}}|/\overline{|\mathbf{u}|}$), all the current meters at M8 and M9 record highly stable current directions, being the most stable among the moorings except for the near-bottom current meter at M4 (Table 4.1). Furthermore, the current meters below 3800 m at M8 record the highest northwestward mean velocities among the moorings at M7–M9 (Table 4.1). These findings suggest that the eastern branch flows primarily at M8, and secondarily at M7 and M9.

Current velocity and directional stability of the eastern branch increase toward the bottom at M7, M7p, and M8 (Tables 4.1 and 4.2); this is similar with the deep-circulation current at the Wake Island Passage (Kawabe et al., 2005). Exceptionally, current velocity and directional stability decrease from M8p-40 to M8p-B. This is probably because the current at M8p-50 and M8p-B is affected by the small valley in which M8p was moored. The current at M9-B is also weaker than M9-40 and M9-35 probably due to disturbance by topography.

The eastern branch was not detected at any mooring during short periods in September 2004 and February–March and May 2005 (Fig. 4.5b), indicating that the eastern branch may

disappear temporarily, as demonstrated previously in the Wake Island Passage (Kawabe et al., 2005). On the other hand, a current flowing toward 270°–360°T was found at M6 continuously in November–December 2004 and July–September 2005, indicating that the eastern branch infrequently expands to M6.

The western branch is detected at M2, being recorded at this mooring from November 2004 to March 2005, from April to June 2005, and from August to September 2005 (Fig. 4.5b). Currents with northeastward mean velocity at M1 and with southward mean velocity at M3 would not connect with the western branch at M2 because coherences between M1 and M2 and between M2 and M3 are not significant at longer periods than 60 days (Fig. 4.8). This suggests that the western branch, flowing solely at M2, has a narrower width than the distance between M1 and M3 of approximately 190 km. The strong current at the peak of current velocity at M2 is not colored in Fig. 4.5b because it is directed toward 0°–10°T; this would undoubtedly be the western branch current according to the current direction histogram of Fig. 4.3b. During the remaining periods, the western branch is not apparent in the current-meter records probably because of its meridional shifts or intermittent disappearance.

4.4. Variability in volume transport of the deep circulation

Daily volume transport of the deep-circulation current was estimated by integrating velocity components normal to the observation line below the average isotherm of $\theta = 1.2$°C for the two hydrographic sections obtained during the KH-04-4 and KH-05-4 cruises (the isotherm is shown in Fig. 4.4). We used the objectively-mapped velocities toward 270°–10°T between M1 and M3 for the volume transport of the western branch and those toward 270°–360°T between M6 and M9 for the eastern branch. The average volume transports of the western and eastern branches are 4.1 ± 1.2 Sv and 9.8 ± 1.8 Sv, respectively.

According to the low-passed volume transport composed of 25-day low-passed velocity (Fig. 4.9), the volume transport of the western branch exceeded 5 Sv during the periods December 2004–March 2005, April–June 2005, and August–September 2005, similar to current velocity at M2, whereas that of the eastern branch exceeded 10 Sv during the periods October 2004–January 2005, April 2005, and July–November 2005. The volume transport of the eastern branch was close to zero during September–October 2004 and February–March and May 2005, when counter-currents were present at M7-M9 (see Fig. 4.5). Thus, the low-passed volume transports of the both branches have variations with intervals of 2–4 months. The temporal variations in volume transport of the western and eastern branches have common dominant periods of 3 months and 1 month (Fig. 4.10). The 3-month-period variations, which may correspond to the above 2–4-month-interval one, have a significant coherence of 0.58

(95% confidence level is 0.39) between the two branches; volume transport of the western branch lags behind that of the eastern branch with a phase of 116° (about 1 month). Although the volume transport of the western branch has high spectral power at periods shorter than 25 days, the large short-term variations may reflect current variations at M2.

The volume transport of the eastern branch increases with increasing its sectional average current velocity (Figs. 4.9b and 4.9c). The correlation coefficient reaches 0.85. Moreover, its volume transport also has a high correlation with its current width, yielding a correlation coefficient of 0.65 (Figs. 4.9b and 4.9d). Daily current width of the eastern branch was estimated from daily horizontal distribution of volume transport per 1-meter width (Fig. 4.11). First, positions of the maximum unit-width volume transports were detected between M6 and M9. They form relatively continuous curves as shown by blue lines in Fig. 4.11, except for short periods in January, February-March, May, and June 2005; the maxima near M5 are separate from the eastern branch. Then, southwestern and northeastern limits of the eastern branch on the observation line were defined as positions where unit-width volume transport decreases to one-tenth of the maximum, as shown by red lines in Fig. 4.11. Though the southwestern limits are mostly found, the northeastern limits are mostly restricted at M9. The restriction would not cause much underestimate of current width because the eastern branch is not expected to expand northeastward further from M9 according to the geostrophic flow by Kawabe et al. (2009). The average current width of the eastern branch is estimated to be 201 ± 70 km.

4.5. Conclusion

Direct velocity measurements with a nine-system mooring array (M1–M9) from 2004 to 2005 and additional two moorings (M7p and M8p) from 2003 to 2004 revealed spatial and temporal properties of the deep-circulation currents southwest of the Shatsky Rise in the western North Pacific. The western branch of the deep-circulation current flowing northwestward (270°–10°T) is detected almost only at M2 (26°15′N) northeast of the Ogasawara Plateau, having a narrower width than the distance between M1 (25°42′N) and M3 (26°48′N) of approximately 190 km. The mean current speed near the bottom at M2 is 3.6 ± 1.3 cm s^{-1}. The eastern branch of the deep-circulation current is located at the southwestern slope of the Shatsky Rise, flowing northwestward mainly at M8 (30˚48′N) on the lower part of the slope of the Shatsky Rise with a mean near-bottom speed of 5.3 ± 1.4 cm s^{-1}. It expands to M7 (30˚19′N) on the foot of the rise with a mean near-bottom speed of 2.8 ± 0.7 cm s^{-1} and M9 (31˚13′N) on the middle of the slope of the rise with a mean speed of 2.5 ± 0.7 cm s^{-1} (nearly 4000-m depth) with a frequency of about 60 % during the mooring period. Furthermore, it expands to M6 (29˚33′N) twice during the mooring period. The width of the eastern branch is

201 ± 70 km on average.

Daily volume transports of the western and eastern branch of the deep-circulation current were estimated with using daily objectively mapped velocities toward 270°–10°T between M1 and M3 and toward 270°–360°T between M6 and M9, respectively. Temporal variations of the volume transports of the western and eastern branches consist of dominant variations with periods of 3 months and 1 month, varying between almost zero and significant amount of volume transport. The 3-month-period variations are significantly coherent to each other with a phase lag of about 1 month for the western branch. The almost zero volume transport due to the occupation of counter-currents occurs at intervals of 2–4 months. This finding is similar to the variations of the current and volume transport at the Wake Island Passage, where the deep-circulation current weakens and pauses with a counter-current between the peaks of the four-month variations (Kawabe et al., 2005). In the eastern branch, volume transport is highly correlated with not only cross-sectional average current velocity but also current width; in other words, volume transport increases with not only current strength but also current width.

The mean volume transport of 4.1 ± 1.2 Sv for the western branch and 9.8 ± 1.8 Sv for the eastern branch is double or more the volume transports of 4 Sv for the eastern branch and 2 Sv for the western branch, which are estimated by Kawabe et al. (2009) on the basis of their geostrophic velocity sections and accumulation of previous results in the upstream regions as reviewed in Chapter 1. This overestimate would be because the current meters are too sparse to estimate exact volume transport by interpolating the current velocities. The difficulty in production of exact current structure may be prominent in wide basins in which the location and width of current vary over time, like in the strait southwest of the Shatsky Rise. In contrast, realistic volume transports have been estimated from current-meter data in narrow straits such as the Samoan Passage (6.0 ± 1.5 Sv; Rudnick, 1997) and the Wake Island Passage (3.6 ± 1.3 Sv; Kawabe et al., 2005). Although the volume transports can be reduced by changing parameters in the present interpolation method, any realistic velocity sections cannot be reproduced as is described in Appendix A. On the other hand, particularly in the eastern branch, the long temporal scale of transport variability such as 3-month period would not differ largely by interpolation parameters (Appendix A).

At M4 (27°55′N), we found a northwestward current varying with a period of 45 days, which is probably part of a deep clockwise eddy around an isolated seamount located immediately east of M4. Appendix B shows that a Taylor cap with a clockwise eddy can occur over a seamount with the similar geographic scale in a steady uniform flow with the typical current velocity found in the present study. However, it is not clear what causes a meso-scale periodic oscillation over a seamount. At the southernmost mooring along 152°E by Schmitz et

al. (1987), which is 28 km northwest of M4, deep current shows a marked periodical variation with about 45-day period (see Fig. 9f in Schmitz et al., 1982). Imawaki (1985) indicates a Rossby wave with a period of 44 day and a westward phase speed of 7.5 cm s^{-1} at five moorings around 30°N, 146°40′E, which is located between the Izu-Ogasawara Ridge and the present study area. Thus, eddies with 45-day-period variability are frequently seen at these latitudes in the western North Pacific. The clockwise eddy at M4 might be a trapped one by the seamount.

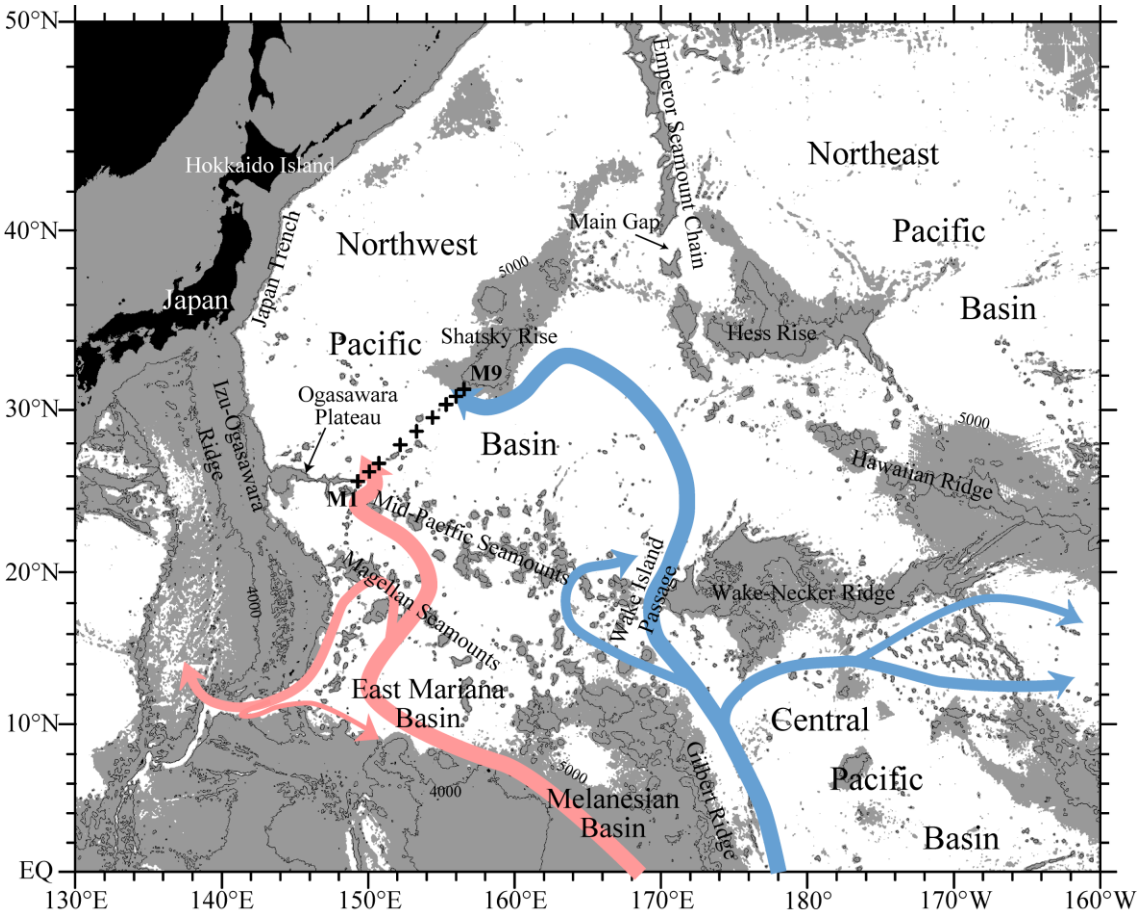

Fig. 4.1 Location of the nine-system mooring array in the western North Pacific. The '+' symbols show the positions of the mooring systems (M1–M9). Shading indicates water depths less than 5000 m and the 4000 m isobaths are shown. Red and blue arrows show the pathways of the western and eastern branches of the deep circulation, respectively.

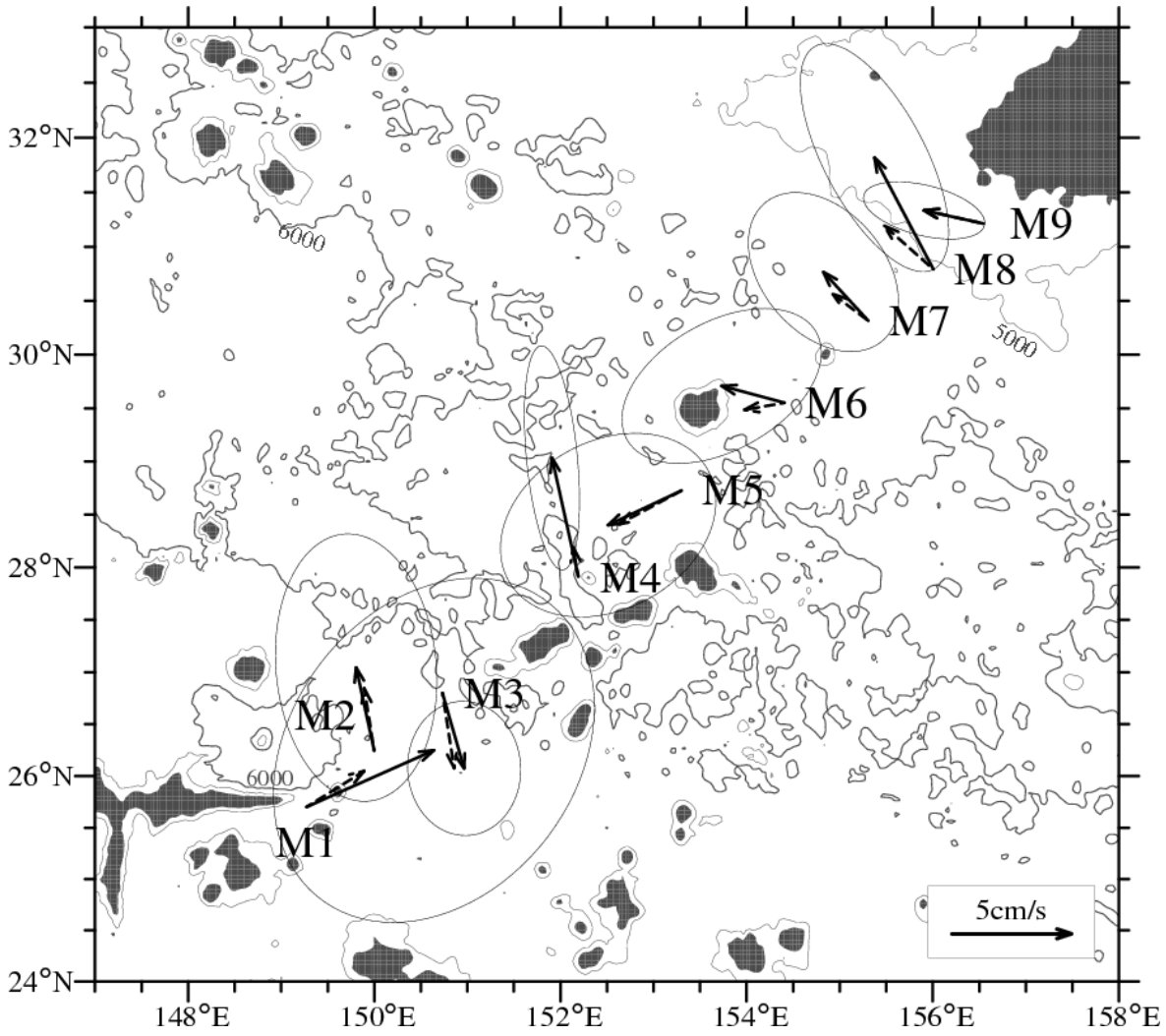

Fig. 4.2 Mean velocity distribution over the period 2004–2005. Solid arrows and ellipses show mean velocities and standard deviations near the bottom, respectively, except for M5 and M9, where those at M5-55 and M9-40 are shown. Dashed arrows show mean velocities at approximately 4000 m depth. The 5000 and 6000 m isobaths are shown by thin and thick lines, respectively, and regions shallower than 4000 m are shaded (based on ETOPO2).

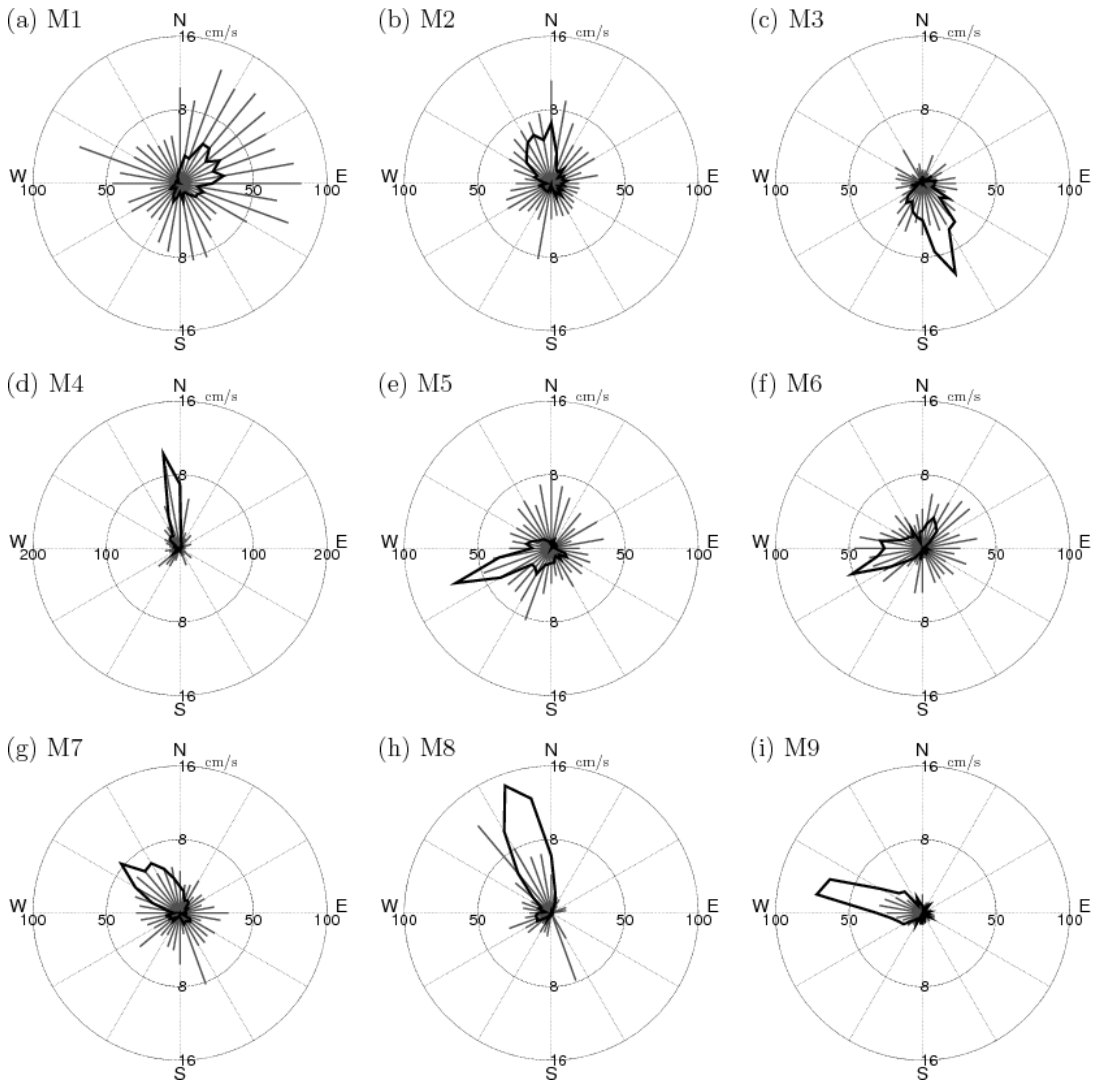

Fig. 4.3 Direction histograms (black curves) and mean values for 10° intervals (gray lines) of daily current velocity near the bottom at M1 (a), M2 (b), M3 (c), M4 (d), M5-55 (e), M6 (f), M7 (g), M8 (h), and M9-40 (i). Horizontal and vertical axes show the histogram scale and current speed (cm s^{-1}), respectively.

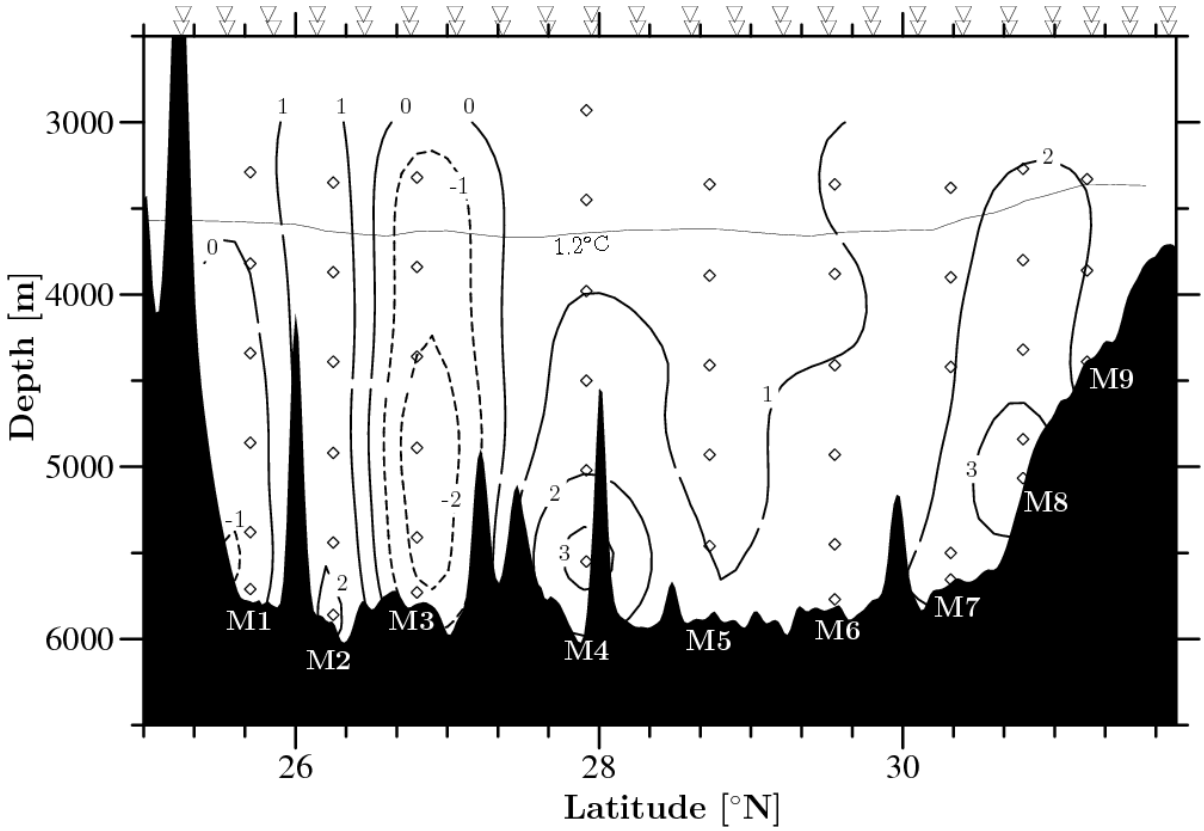

Fig. 4.4 Vertical distribution of cross-sectional components of objectively mapped current velocity (positive northwestward). Contour interval is 1 cm s^{-1}. The 1.2°C isotherm of potential temperature is the average of two hydrographic sections obtained during the R/V Hakuho-maru KH-04-4 and KH-05-4 cruises, for which the station locations are shown by the lower and upper triangles at the top of the panel, respectively. The locations of current meters are shown by diamonds. Bottom topography is based on ETOPO2.

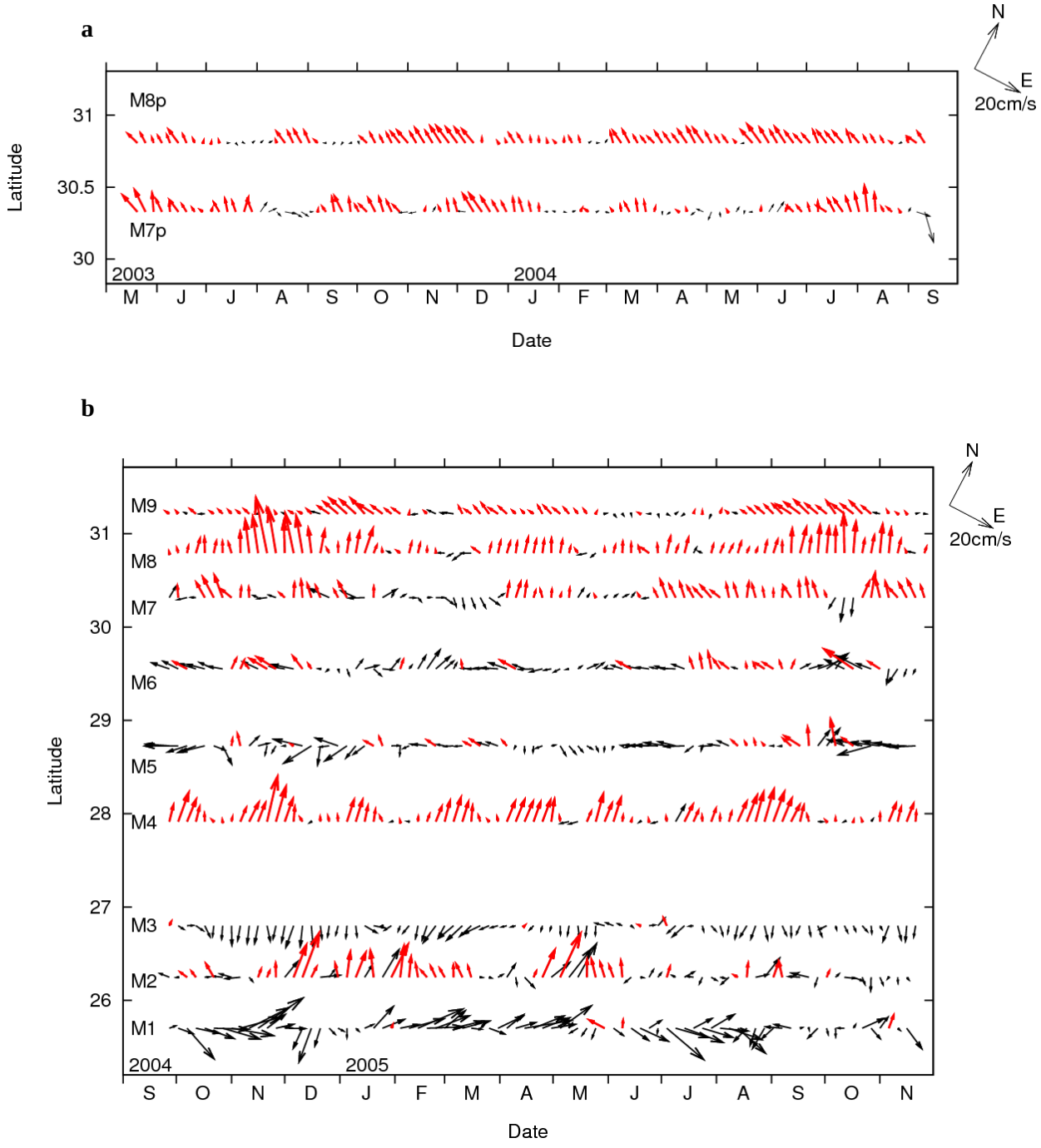

Fig. 4.5 Stick diagrams of 5-day-averaged current velocities near the bottom from 2003 to 2004 (a) and from 2004 to 2005 (b). Current velocities at M8p-40, M5-55, and M9-40 are shown for M8p, M5, and M9, respectively. Orientation is slant so that northwestward flows perpendicular to the observation line directs upward on paper as shown at the upper right corners. Red arrows are velocities toward 270°–360°T.

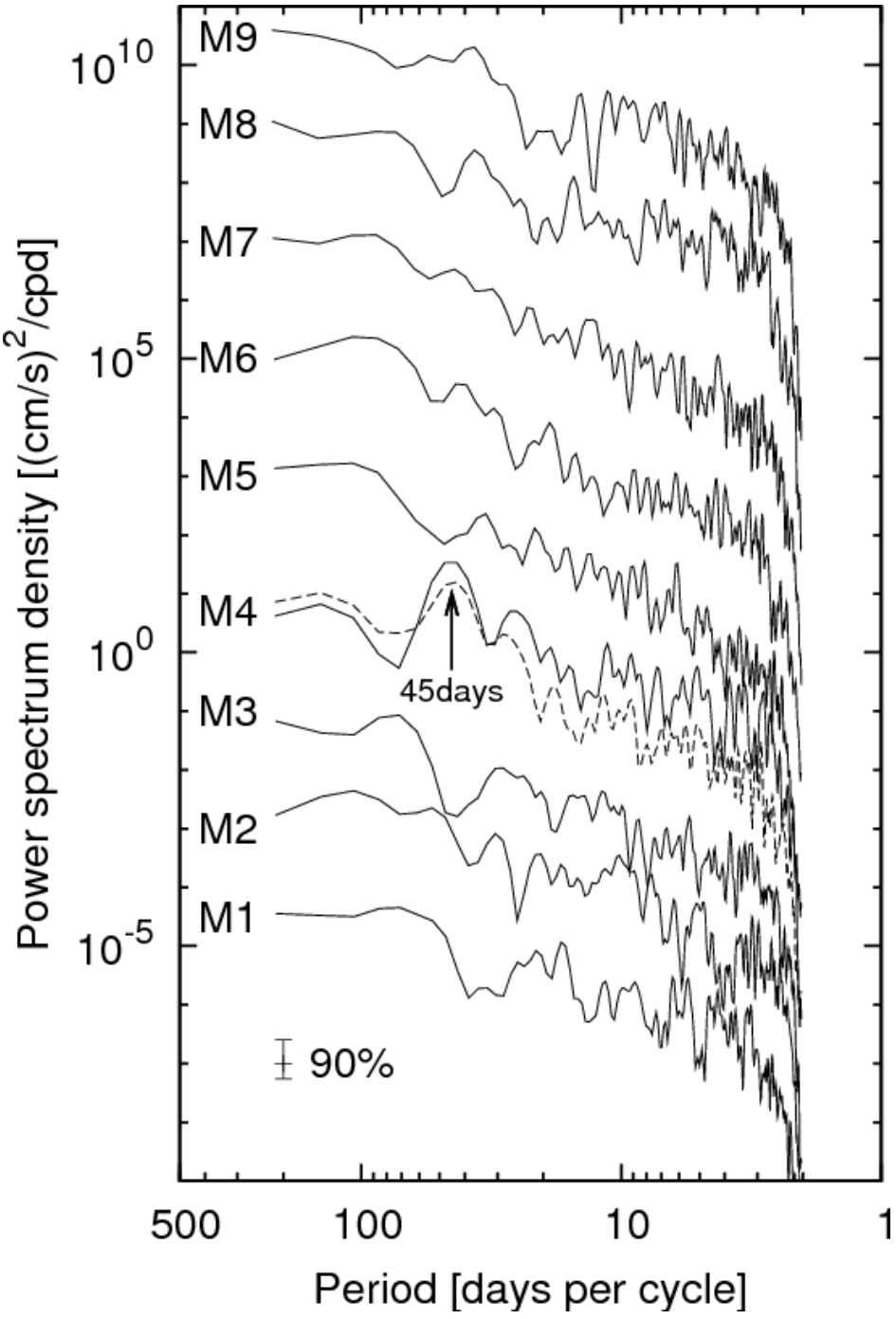

Fig. 4.6 Power spectral densities of the major axis components of current variability near the bottom for M1 to M9 (solid lines) and at 3980 m depth for M4 (dashed line). To eliminate overlap, each power spectrum is shifted by a 10^2 (cm s^{-1})^2 (cycle per day)$^{-1}$ decrement (M3 to M1) or increment (M5 to M9).

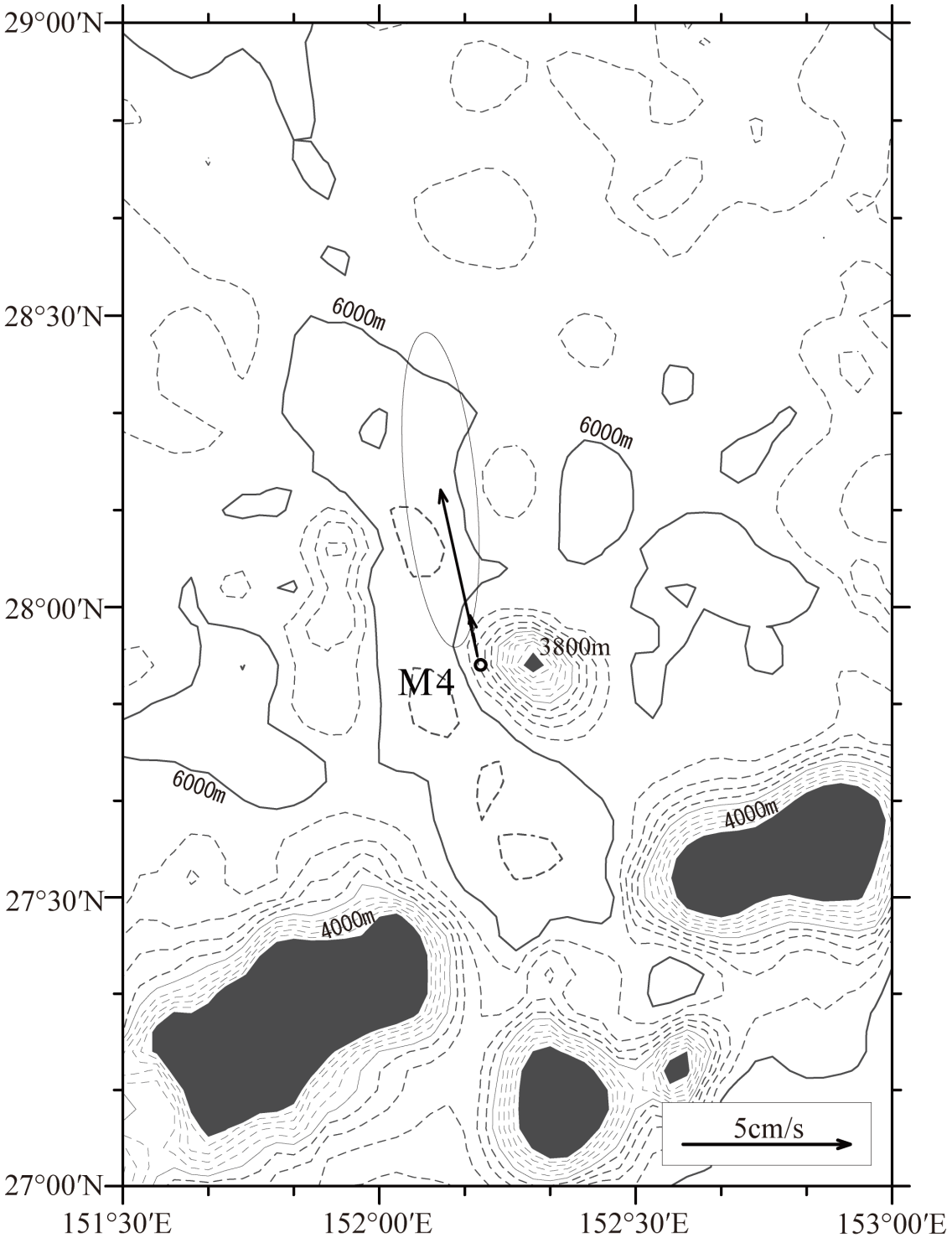

Fig. 4.7 The narrow, tall seamount with a top at 3800 m depth in the vicinity of the mooring M4. Hatched regions are shallower than 4000 m depth. Contours are shown at every 200 m by broken lines and at every 1000 m by solid lines.

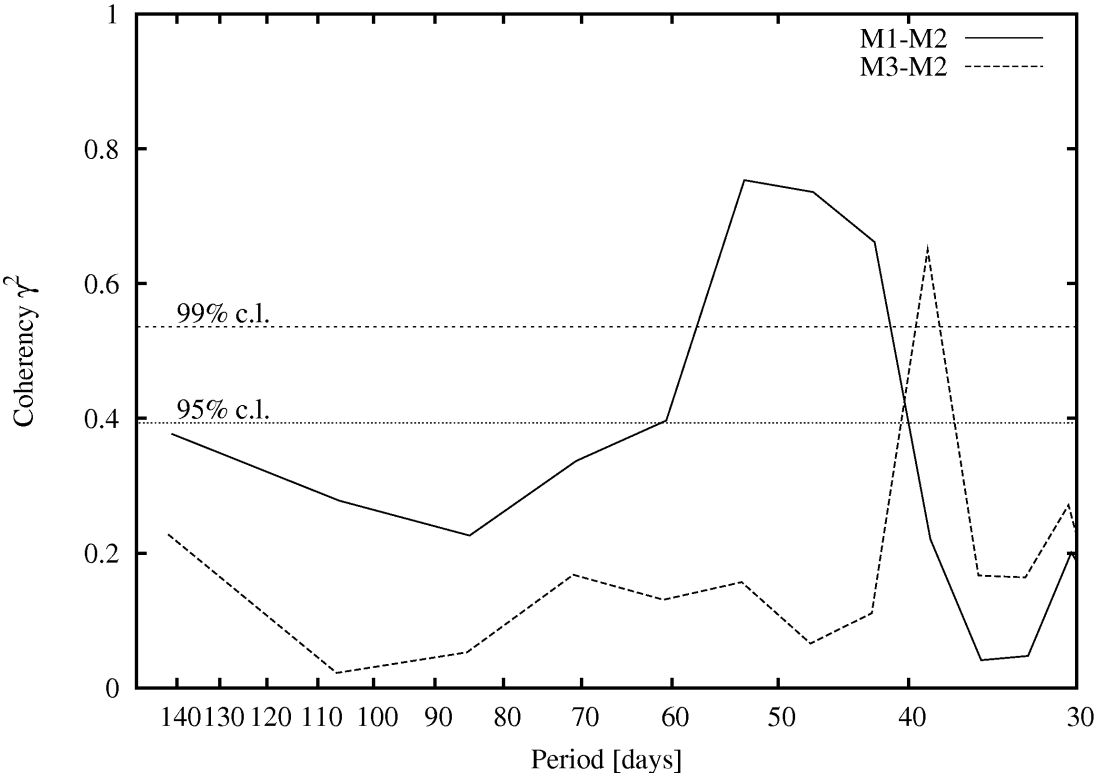

Fig. 4.8 Coherency for major-axis current variations among M1, M2, and M3.

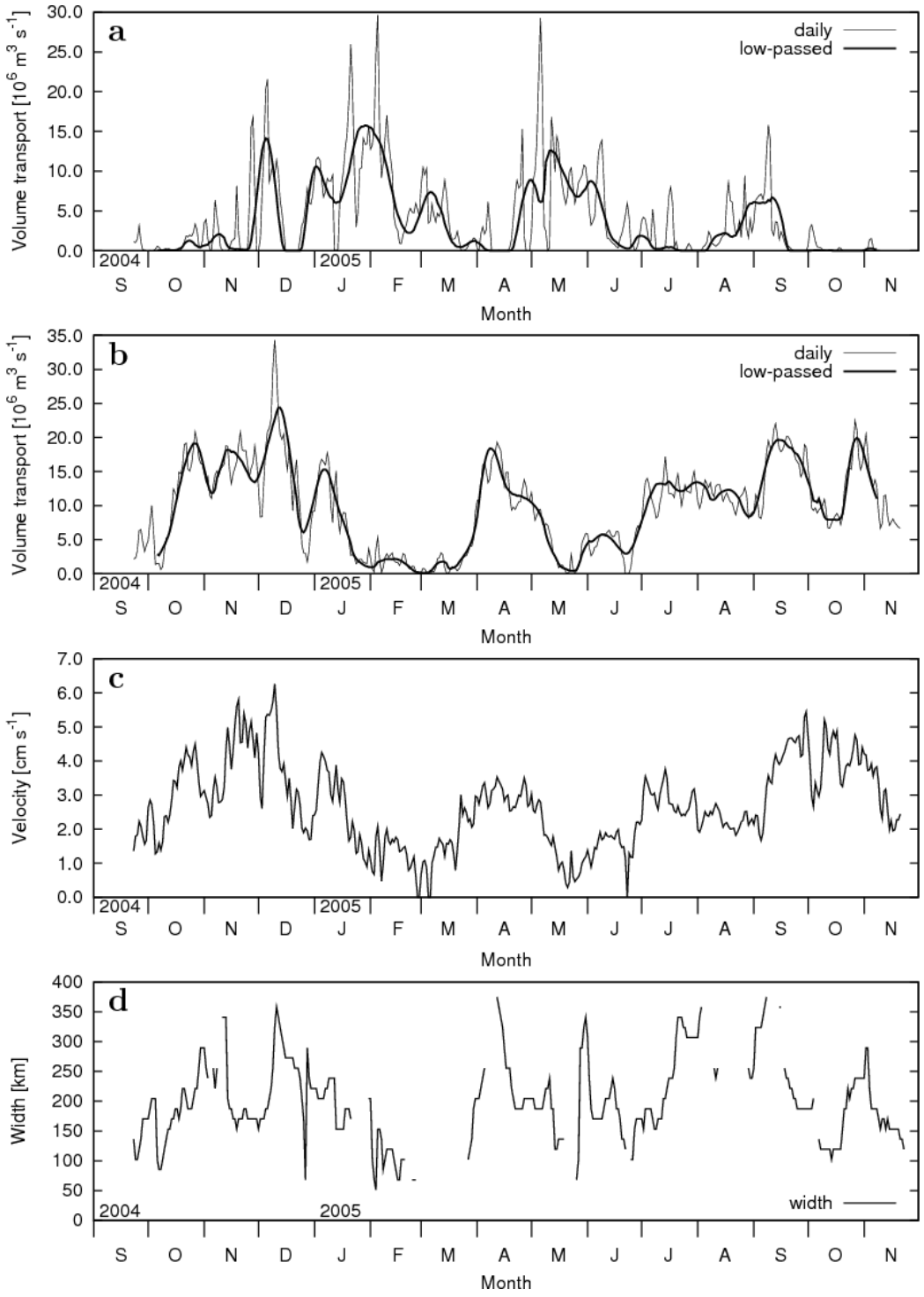

Fig. 4.9 Time series of daily and low-passed volume transports of the western branch current (a) and the eastern branch current (b), and time series of cross-sectional average current velocity (c) and current width of the eastern branch (d).

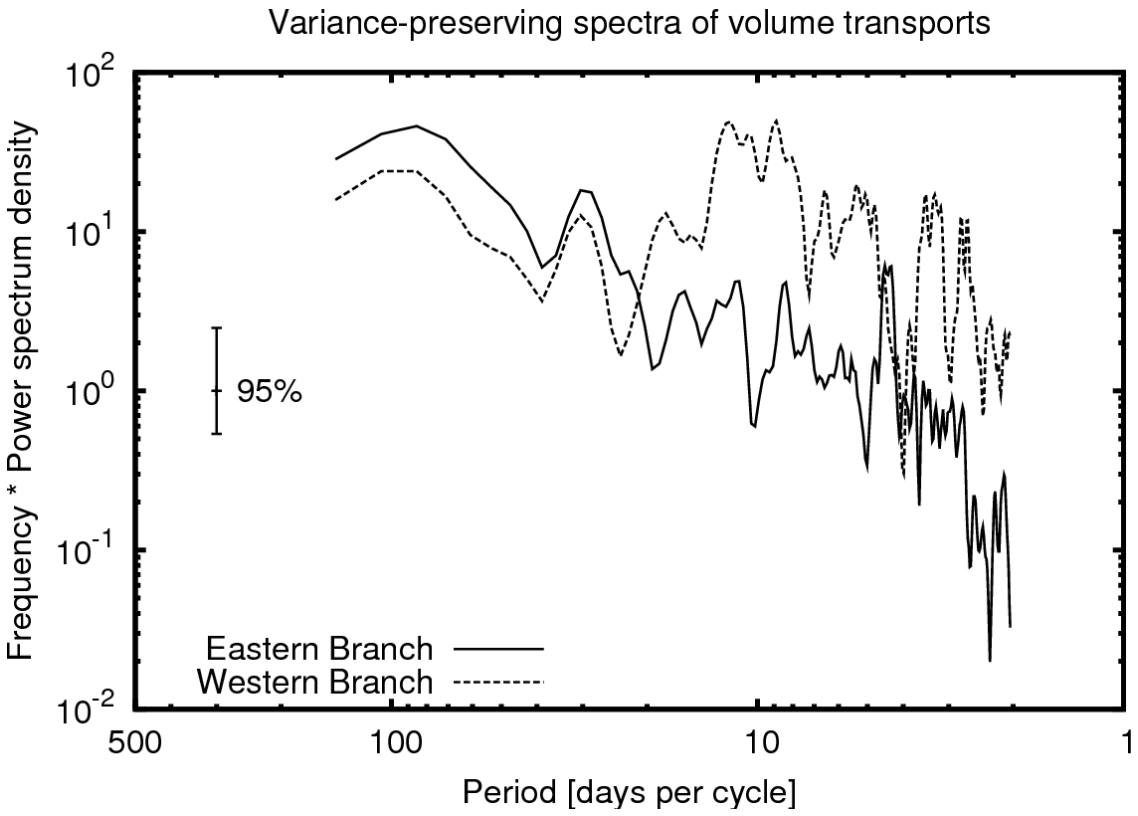

Fig. 4.10 Variance-preserving power spectra of volume transport variability of the western branch current (solid line) and the eastern branch current (dashed line).

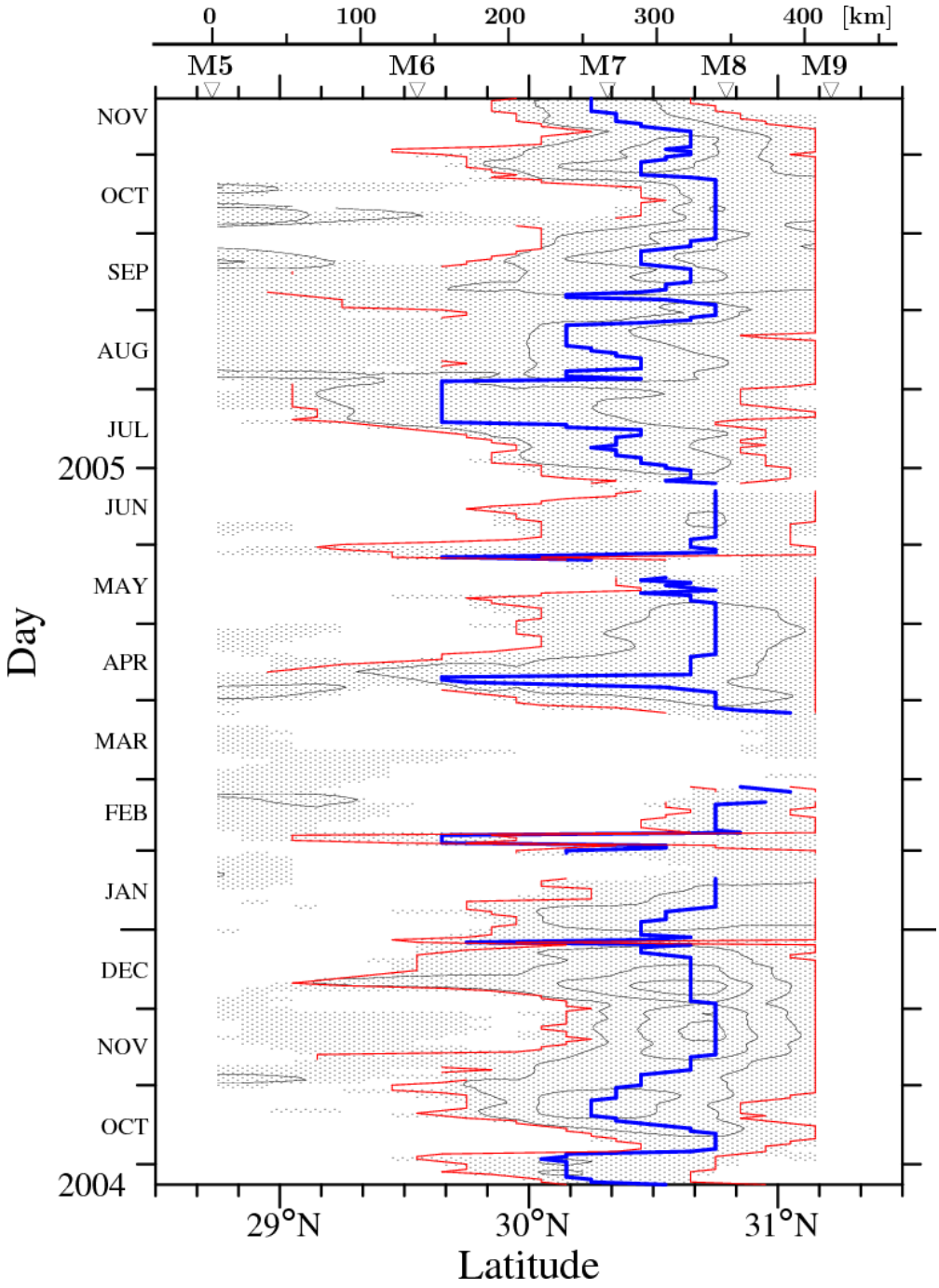

Fig. 4.11 Temporal change of horizontal distribution of volume transport per 1-meter width by northwestward velocities in the eastern branch. Contour interval is 50 m^3 s^{-1} and non-zero transport is shown by hatching. Maximum-transport position is shown by blue lines, and the northeastern and southwestern limits of the eastern branch are shown by red lines. Distance in kilometers along the observation line from M5 is shown at the top.

Table 4.1 Statistics of daily current velocity measured by each moored instrument (September 2004 to December 2005). The suffixes "30," "35," "40," "45," "50," "55," and "B" in record IDs indicate the record at 3000, 3500, 4000, 4500, 5000, and 5500 m nominal depth and near the bottom, respectively. Instrument types "UCM", "RCM11", "3DACM", and "ADCP" stand for Union Engineering current meter, Aanderaa RCM11, FSI 3D-ACM, and RDI Workhorse, respectively. Standard errors of mean current speeds are shown after plus-minus signs. The value $|\bar{\mathbf{u}}|/\overline{|\mathbf{u}|}$ represents the ratio of the vector mean to the scalar mean of velocity (see text).

Record ID	Mooring depth (m)	Instrument type	Record length (days)	Mean current		Major axis direction of variability (°T)	$\frac{\lvert\overline{\mathbf{u}}\rvert}{\overline{\lvert\mathbf{u}\rvert}}$
				Speed (cm s^{-1})	Dir. (°T)		
M1, 25°42.1'N, 149°16.3'E, water depth 5760m, from 22 Sep. 2004 to 21 Nov. 2005							
M1-35	3290	UCM	424	2.42 ± 1.23	41	47	0.55
M1-40	3820	UCM	424	2.84 ± 1.45	58	24	0.50
M1-45	4340	UCM	424	3.75 ± 1.47	62	21	0.58
M1-50	4860	RCM11	424	3.78 ± 1.67	69	31	0.50
M1-55	5380	RCM11	424	4.63 ± 1.78	64	31	0.54
M1-B	5710	UCM	424	5.84 ± 1.82	65	37	0.60
M2, 26°14.9'N, 149°59.9'E, water depth 5910m, from 21 Sep. 2004 to 23 Nov. 2005							
M2-35	3350	UCM	426	2.29 ± 0.72	345	349	0.70
M2-40	3870	UCM	426	2.63 ± 0.90	350	347	0.71
M2-45	4390	RCM11	426	2.76 ± 1.10	351	348	0.63
M2-50	4920	RCM11	426	2.86 ± 1.18	349	348	0.58
M2-55	5440	RCM11	426	3.05 ± 1.17	353	352	0.58
M2-B	5860	UCM	426	3.56 ± 1.25	347	354	0.59
M3, 26°48.0'N, 150°44.0'E, water depth 5780m, from 21 Sep. 2004 to 24 Nov. 2005							
M3-35	3320	UCM	427	3.30 ± 0.64	181	48	0.84
M3-40	3840	UCM	427	3.18 ± 0.66	171	54	0.79
M3-45	4360	UCM	427	3.33 ± 0.77	165	120	0.75
M3-50	4890	3DACM	400	4.88 ± 0.96	169	170	0.79
M3-55	5410	RCM11	427	3.54 ± 0.67	170	177	0.78
M3-B	5730	UCM	427	3.28 ± 0.65	163	176	0.75

Table 4.1 (continued).

M4, 27°55.0'N, 152°11.5'E, water depth 5600m, from 18 Sep. 2004 to 29 Nov. 2005							
M4-30	2930	UCM	429	0.72 ± 0.40	22	351	0.32
M4-35	3450	UCM	429	0.84 ± 0.46	8	345	0.35
M4-40	3980	UCM	429	1.23 ± 0.56	349	347	0.40
M4-45	4500	3DACM	377	1.71 ± 0.73	351	1	0.49
M4-50	5020	RCM11	220	2.67 ± 0.76	342	346	0.81
M4-B	5550	UCM	429	5.08 ± 0.85	347	354	0.92
M5, 28°43.7'N, 153°18.1'E, water depth 5830m, from 18 Sep. 2004 to 26 Nov. 2005							
M5-35	3360	UCM	431	2.49 ± 0.94	235	259	0.60
M5-40	3890	UCM	431	2.97 ± 1.01	241	257	0.64
M5-45	4410	UCM	431	2.68 ± 0.94	250	256	0.67
M5-50	4930	3DACM	391	1.60 ± 0.74	250	245	0.37
M5-55	5460	RCM11	431	3.40 ± 1.02	244	240	0.60
M6, 29°33.1'N, 154°24.4'E, water depth 5820m, from 17 Sep. 2004 to 27 Nov. 2005							
M6-35	3360	UCM	433	1.69 ± 1.01	268	240	0.38
M6-40	3880	UCM	433	1.70 ± 0.99	259	233	0.40
M6-45	4410	UCM	433	1.34 ± 0.64	275	235	0.46
M6-50	4930	3DACM	391	2.18 ± 0.84	279	219	0.47
M6-55	5450	RCM11	433	2.10 ± 0.86	270	229	0.48
M6-B	5770	UCM	433	2.72 ± 0.97	284	240	0.52
M7, 30°19.0'N, 155°18.4'E, water depth 5705m, from 16 Sep. 2004 to 30 Nov. 2005							
M7-35	3380	UCM	437	1.75 ± 1.00	314	321	0.49
M7-40	3900	UCM	437	1.86 ± 0.85	306	315	0.56
M7-45	4420	RCM11	437	2.10 ± 0.75	303	309	0.59
M7-55	5500	RCM11	437	2.34 ± 0.65	311	314	0.56
M7-B	5655	UCM	437	2.77 ± 0.72	317	319	0.57
M8, 30°47.5'N, 156°00.4'E, water depth 5116m, from 15 Sep. 2004 to 1 Dec. 2005							
M8-35	3270	UCM	440	2.26 ± 0.53	311	315	0.83
M8-40	3800	UCM	440	2.74 ± 0.57	311	310	0.87
M8-45	4320	RCM11	440	3.34 ± 0.77	311	309	0.89
M8-50	4840	RCM11	440	3.37 ± 0.63	318	335	0.85
M8-B	5066	ADCP	440	5.29 ± 1.36	332	332	0.89
M9, 31°12.8'N, 156°32.6'E, water depth 4440m, from 15 Sep. 2004 to 1 Dec. 2005							
M9-35	3330	UCM	440	2.55 ± 0.66	283	286	0.86
M9-40	3860	RCM11	440	2.54 ± 0.71	282	283	0.85
M9-B	4390	UCM	440	1.80 ± 0.63	281	294	0.71

Table 4.2 As for Table 1, but for mooring results from May 2003 to September 2004.

Record ID	Mooring depth (m)	Instrument type	Record length (days)	Mean current		Major axis direction of variability (°T)	$\frac{\lvert\overline{\mathbf{u}}\rvert}{\overline{\lvert\mathbf{u}\rvert}}$
				Speed (cm s^{-1})	Dir. (°T)		
M7p, 30°19.7'N, 155°19.2'E, water depth 5725m, from 14 May 2003 to 17 Sep. 2004							
M7p-30	2895	UCM	488	0.73 ± 0.32	286	300	0.56
M7p-40	3920	UCM	488	1.92 ± 0.59	311	314	0.67
M7p-50	4945	3DACM	212	2.27 ± 1.06	310	355	0.57
M7p-55	5370	RCM11	488	1.84 ± 0.54	311	306	0.62
M7p-B	5695	UCM	488	2.38 ± 0.66	314	308	0.65
M8p, 30°48.4'N, 155°59.6'E, water depth 5410m, from 14 May 2003 to 18 Sep. 2004							
M8p-30	3205	UCM	488	1.18 ± 0.26	307	313	0.78
M8p-40	4230	UCM	488	3.24 ± 0.55	300	294	0.93
M8p-50	5255	3DACM	215	2.36 ± 0.85	349	356	0.79
M8p-B	5380	RCM11	434	1.09 ± 0.35	354	334	0.60

Chapter 5. General conclusion

The author clarified the pathway and the volume transport variability of the deep-circulation current transporting Lower Circumpolar Deep Water (LCDW) in the western North Pacific with analyzing current velocity data directly measured at two mooring arrays along 165°E and southwest of the Shatsky Rise. The both arrays are located at key points for the deep-circulation current in the region between 20°N and 35°N in the Northwest Pacific Basin. Five moorings were deployed at 27°–35°N along 165°E from 1991 to 1993 and additional one mooring at 27°N, 168°E from 1989 to 1991. Nine moorings were deployed between the Shatsky Rise and the Ogasawara Plateau from 2004 to 2005 and additional two moorings on the foot of the Shatsky Rise from 2003 to 2004. The author also utilized recent high-quality and high-resolution dissolved-oxygen data in order to estimate the pathway of the deep-circulation current between the moorings.

First, the author examined the pathway of the deep-circulation current between 20°N and 35°N in the Northwest Pacific Basin, which has not been confirmed and has been different among researchers. The points of issue that the author organized the subject on the pathways of the deep-circulation current into in Chapter 1 were the following: (1) whether part of the eastern branch flows eastward between the Wake-Necker Ridge and the Hess Rise into the Northeast Pacific Basin or not, (2) whether the western branch proceeds northwestward with a detour east of the Ogasawara Plateau or not, and (3) whether the deep-circulation current flows westward or eastward between 20°N and 35°N. These questions are answered in the present thesis as below.

As for the question (1), the author did not find the deep-circulation current flowing eastward between the Wake-Necker Ridge and the Hess Rise into the Northeast Pacific Basin, which was supposed as one of the routes of the deep water from south into the Northeast Pacific Basin based on relatively sparse data of water property (Chapter 3). As for the question (2), the author concluded that the western branch proceeds northwestward with a detour east of the Ogasawara Plateau (Chapter 3, Chapter 4). As for the question (3), the author concluded that the deep-circulation current flows not eastward but westward as the eastern branch after passing the Wake Island Passage (Chapter 2, Chapter 3, Chapter 4).

Thus, after passing north-northeastward through the Wake Island Passage, the eastern branch takes a cyclonic turn, proceeds northwestward around 33°N, 165°E, and takes a detour south of the Shatsky Rise. Figure 5.1 shows the picture of the deep-circulation current in the western North Pacific added the location of the deep current classified by our mooring

observations at 3 points (marked by blue stars). These findings of pinpoint location could not be obtained without the mooring observations because the water properties of LCDW of high salinity and high dissolved oxygen let us know only a rough location with relatively great width as shown in Chapter 3.

Second, the author examined the temporal variations of volume transports of the western and eastern branches southwest of the Shatsky Rise (Chapter 4). Time series of their volume transports have dominant spectral peaks at periods of 3 months and 1 month; the almost zero volume transport occurs at intervals of 2–4 months. This is the fourth result on the temporal characteristics of volume transport of the deep-circulation current in the Pacific, following the results at the Samoan Passage (Rudnick, 1997), in the Southwest Pacific Basin (Whitworth et al., 1999), and at the Wake Island Passage (Kawabe et al., 2005).

The volume transport variation of the eastern branch flowing northwestward mainly on the lower part of the slope of the Shatsky Rise has rather high correlation with its width variation. It has an average width of 200 ± 70 km and intermittently expands up to 200 km away southwestward from the main position. Compared with the deep-circulation current in the Southwest Pacific Basin with a mean width of 700 km with flow most intense on the flank of the Tonga-Kermadec Ridge (Whitworth et al., 1999), the eastern branch in the Northwest Pacific Basin has only about one-third width. The western branch is also so narrow that we find it almost exclusively at one mooring northeast of the Ogasawara Plateau.

These findings on the temporal and spatial structures of the deep-circulation current between 20°N and 35°N in the western North Pacific do not only elucidate the deep circulation pathway that has been different for researchers so far, but also suggest the northward extension of the meridional overturning circulation (MOC) in the Pacific Ocean. The two branches of the deep-circulation current would converge to the east of Japan (Fujio and Yanagimoto, 2005), and the confluence flows northward east of the Japan Trench at 40°N (Kojiro Ando, personal communication). The deep circulation would continue flowing northward along the Japan and Kuril trenches to the northernmost point of the Northwest Pacific Basin at about 55°N. Thus, almost all LCDW entering the Northwest Pacific Basin flows into the Northeast Pacific Basin through the Aleutian Trench region. This leads to the conclusion that the MOC in the Pacific Ocean extends to the Aleutian Trench at 55°N, namely, further north than the northern limit (20°–40°N) of the MOC represented from geostrophic velocities at several transpacific hydrographic sections with the inverse technique by Macdonald et al. (2009) and so on.

The present thesis demonstrates two subjects which should be clarified in the next step of deep circulation studies. The first subject is the cause of the 3-month-period variation in

volume transport of the deep-circulation current southwest of the Shatsky Rise. We compare volume transport variations along the pathway of the deep-circulation current shown in Fig. 5.2d. The 3-month-period variation of volume transport of the eastern branch is similar to that at the Wake Island Passage (Kawabe et al., 2005) (Fig. 5.2a), while it is not similar to those at the Samoan Passage (Rudnick, 1997) (Fig. 5.2b) and in the Southwest Pacific Basin (Whitworth et al., 1999) (Fig. 5.2c). Rudnick (1997) speculated that the 1-month-period transport variation at the Samoan Passage would be due to a resonance in the Samoa Basin south of the passage. Kawabe et al. (2005) speculated a relation of the 3–4-month-period variation at the Wake Island Passage to the dominant 90-day-period variation in sea level at the Wake Island, which is due to westward propagation of the disturbances generated at the Big Island of Hawaii (Mitchum, 1995). The 3–4-month-period transport variation of the eastern branch may be propagated downstream and found southwest of the Shatsky Rise.

The second subject is the dynamical mechanism of pathway of the eastern branch entering the Northwest Pacific Basin through the Wake Island Passage. The eastern branch current passes the deepest part of the small basin surrounded by the Wake-Necker Ridge, the Emperor Seamount Chain, and the Shatsky Rise, turns anticlockwise in this basin, and reaches immediately south of the Shatsky Rise. This shows that the eastern branch in the Northwest Pacific Basin is not the western boundary current as it does not flow along the Mid-Pacific Seamounts. The other parts of the deep-circulation current flow northward along the western boundary of the Pacific Ocean. In a 1-degree-grid numerical model, Ishizaki (1994) showed that the eastern branch after passing the Wake Island Passage flows partly along the Mid-Pacific Seamounts and partly northward along the Shatsky Rise with turning clockwise in the small basin. If the bottom topography is expressed more realistically in a finer-grid model with 11-km grids, the eastern branch flows not along the Mid-Pacific Seamounts but along the f/h contours, and is modified more realistically by taking upwelling at the current into consideration (Shinzou Fujio, personal communication).

Dynamics of these phenomena should be examined using ocean models. Before that, they may have to be described more exactly by further observations.

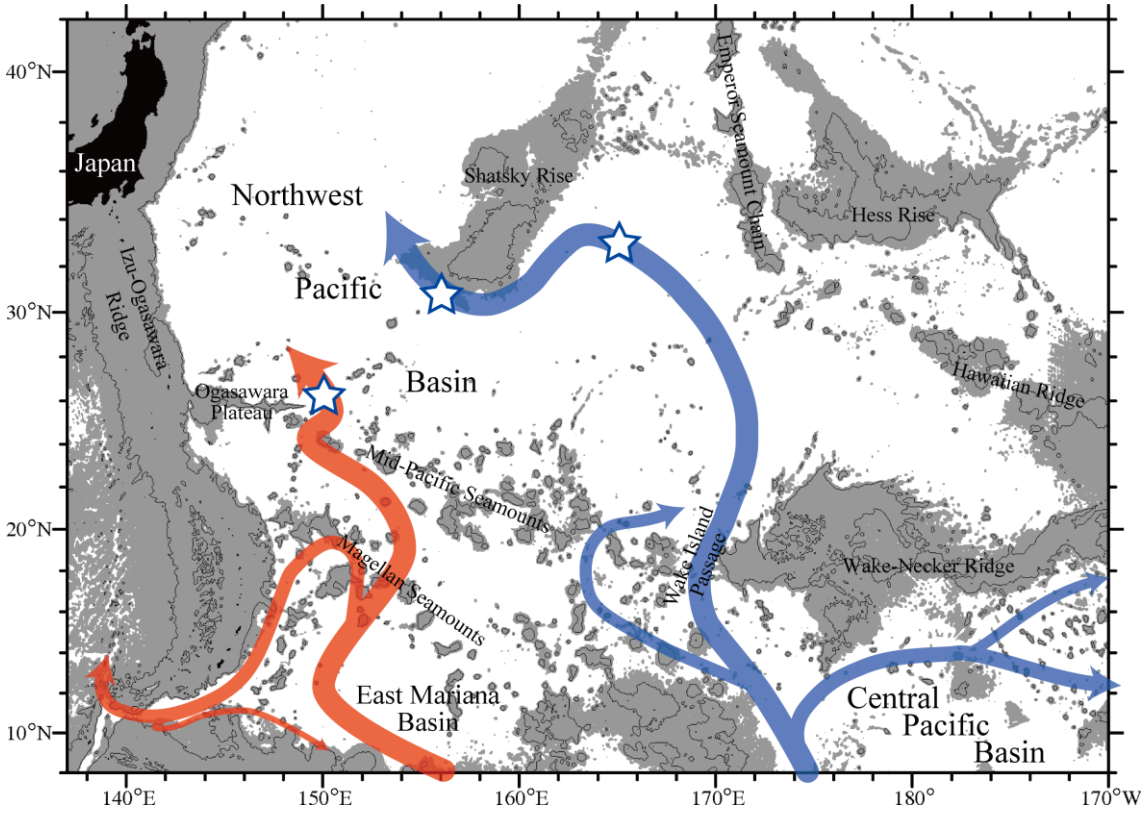

Fig. 5.1 The pathways of the deep-circulation current in the western North Pacific. The blue arrow shows the eastern branch, and the orange arrow shows the western branch. The positions of these branches in the Northwest Pacific Basin are identified by the moorings marked by blue stars in the present thesis. Bottom topography is shown by isobaths of 4000 m and shades for shallower than 5000 m.

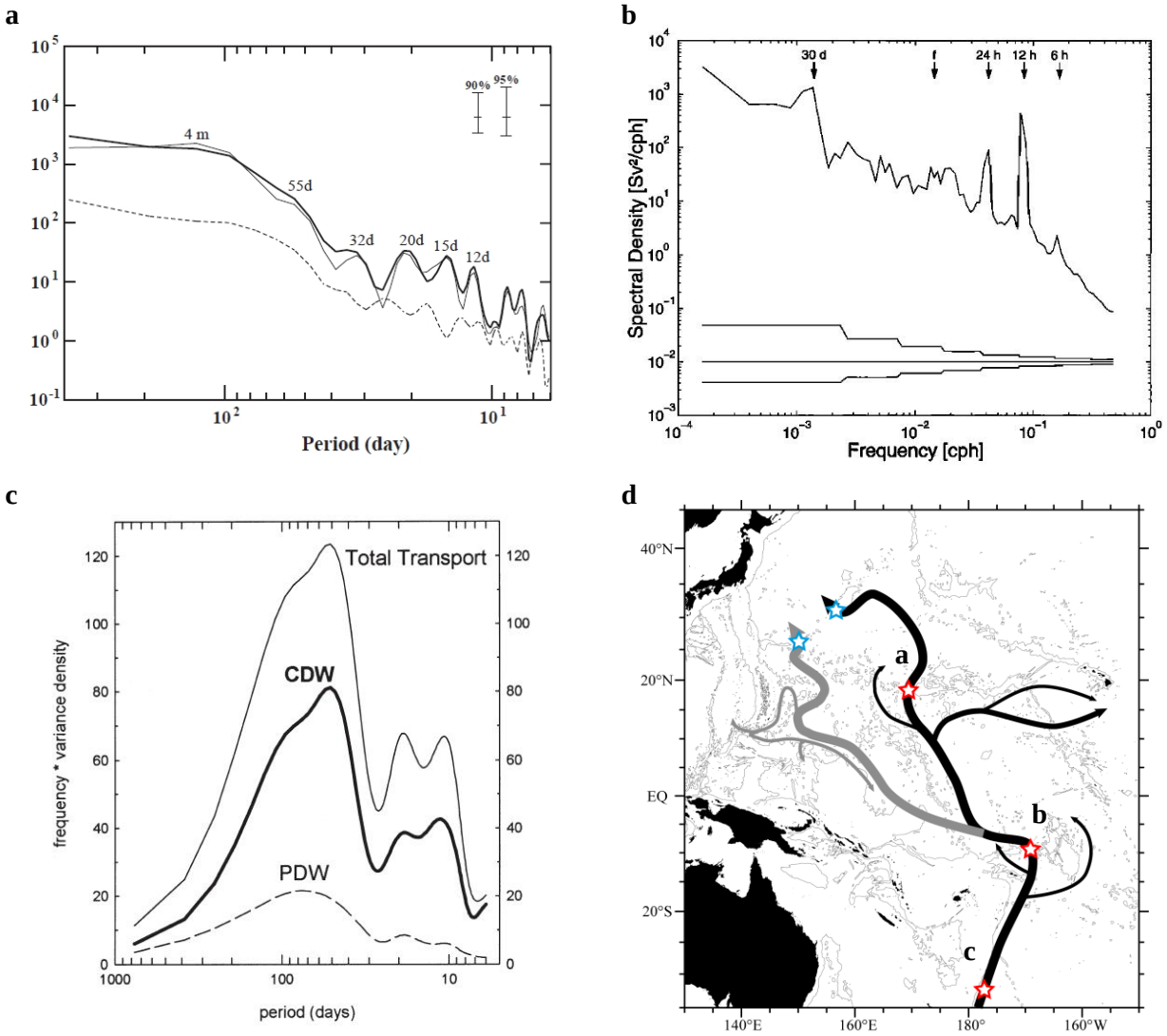

Fig. 5.2 Power spectrum of volume transport of the deep-circulation current (a) at the Wake Island Passage (thick line) (Kawabe et al., 2005), (b) at the Samoan Passage (Rudnick, 1997), and (c) in the Southwest Pacific Basin (denoted by CDW) (Whitworth et al., 1999). The map (d) shows the positions of (a)–(c) by red stars and the positions of the moorings in the present study by blue stars. Black arrows are the deep circulation current and the following eastern branch and gray arrows are the western branch in the map (d).

Appendix A. Dependency of volume transport estimation from current meter data on interpolation method

In order to estimate daily volume transports southwest of the Shatsky Rise from cross-sectional components of directly-measured current speeds at rather sparse mooring systems, the author integrated daily grid-point components interpolated to fine grids with a vertical interval of 100 m and a latitudinal interval of 0.1° on the mooring-array section (Chapter 4). The author used a traditional optimal interpolation method by Bretherton et al. (1976), which needs a correlation matrix for state estimation constructed from a priori parameters: a noise level and horizontal and vertical influence radii. This optimal interpolation method does not only interpolate between data points but also smoothes observed data within the noise level. Dependency of volume transports of the eastern and western branches on these parameters is examined as in Table A.1. Within this range of parameters, the volume transport of the eastern branch changes from 11.8 ± 2.2 Sv in Case c1 to 5.0 ± 0.8 Sv in Case a3, and that of the western branch changes from 5.0 ± 1.4 Sv in Case b1 to 2.0 ± 0.5 Sv in Case c3. Error ranges of volume transports in Table A.1 are merely standard errors in estimating mean values from time series of transports. Differences among the cases are generally larger than these standard errors although the range of parameters can be selected arbitrarily. The larger noise level is given, the smaller interpolated speeds are located at grid points, and then, the smaller volume transports are obtained (Cases 1 to 3). Dependency on influence radii (Cases a to c) is rather complex for the western branch while the transport of the eastern branch decreases with an increase in influence radii.

Case b2 is the parameter combination leading volume transports of 9.8 ± 1.8 Sv for the eastern branch and 4.1 ± 1.2 Sv for the western branch in Chapter 4. In this case, the noise level is comparable to the standard errors of the mean velocities and influence radii are similar to the spacing of the mooring instruments. Furthermore, the mean velocity section in Case b2 seems more realistic than those in Cases 1 and 3 and Cases a and c (Fig. A.1). The velocity section in Case a3 is much different from our familiar one; there are many velocity cores. The velocity section in Case c3 is too strongly smoothed; it has a too wide negative core near 27°N. Although we have no objective criterion to discriminate realistic velocity sections, this optimal interpolation method is unlikely to lead realistic volume transport, which is similar to the transports in Cases a3 and c3, within parameters producing realistic velocity sections. A simple linear interpolation also leads large volume transport of 11.1 ± 2.1 Sv for the eastern branch and 4.3 ± 1.3 Sv for the western branch.

Because the gridded current speeds are small in Cases a3 and c3, zero volume transports occur more often than in Case b2 (Fig. A.2). However, rough shape of the time-series diagram of volume transport of the eastern branch in Cases a3 and c3 does not differ much from that in Case b2 (Fig. A.2a). On the other hand, that of the western branch largely varies with interpolation parameters (Fig. A.2b).

Table A.1 Volume transport depending on the parameters of objective interpolation method of Bretherton et al. (1976). Upper and lower value in each column is volume transport by Sv (1 Sv = 10^6 m^3 s^{-1}) of the eastern branch and the western branch, respectively. Rx and Rz indicates horizontal influence radius (latitudinal degree) and vertical influence radius (meter), respectively.

Noise level Influence radii	*Cases 1* 0.1 cm^2 s^{-2}	*Cases 2* 0.5 cm^2 s^{-2}	*Cases 3* 4.0 cm^2 s^{-2}
Cases a Rx = 0.25°, Rz = 250m	*Case a1* 7.7 ± 1.3 Sv 4.2 ± 1.0 Sv	*Case a2* 6.9 ± 1.1 Sv 3.7 ± 0.8 Sv	*Case a3* 5.0 ± 0.8 Sv 3.2 ± 0.5 Sv
Cases b Rx = 0.5°, Rz = 500m	*Case b1* 10.6 ± 2.0 Sv 5.0 ± 1.4 Sv	*Case b2* 9.8 ± 1.8 Sv 4.1 ± 1.2 Sv	*Case b3* 6.8 ± 1.2 Sv 2.8 ± 0.6 Sv
Cases c Rx = 1.0°, Rz = 1000m	*Case c1* 11.8 ± 2.2 Sv 4.6 ± 1.4 Sv	*Case c2* 11.2 ± 2.1 Sv 2.9 ± 0.9 Sv	*Case c3* 8.8 ± 1.7 Sv 2.0 ± 0.5 Sv

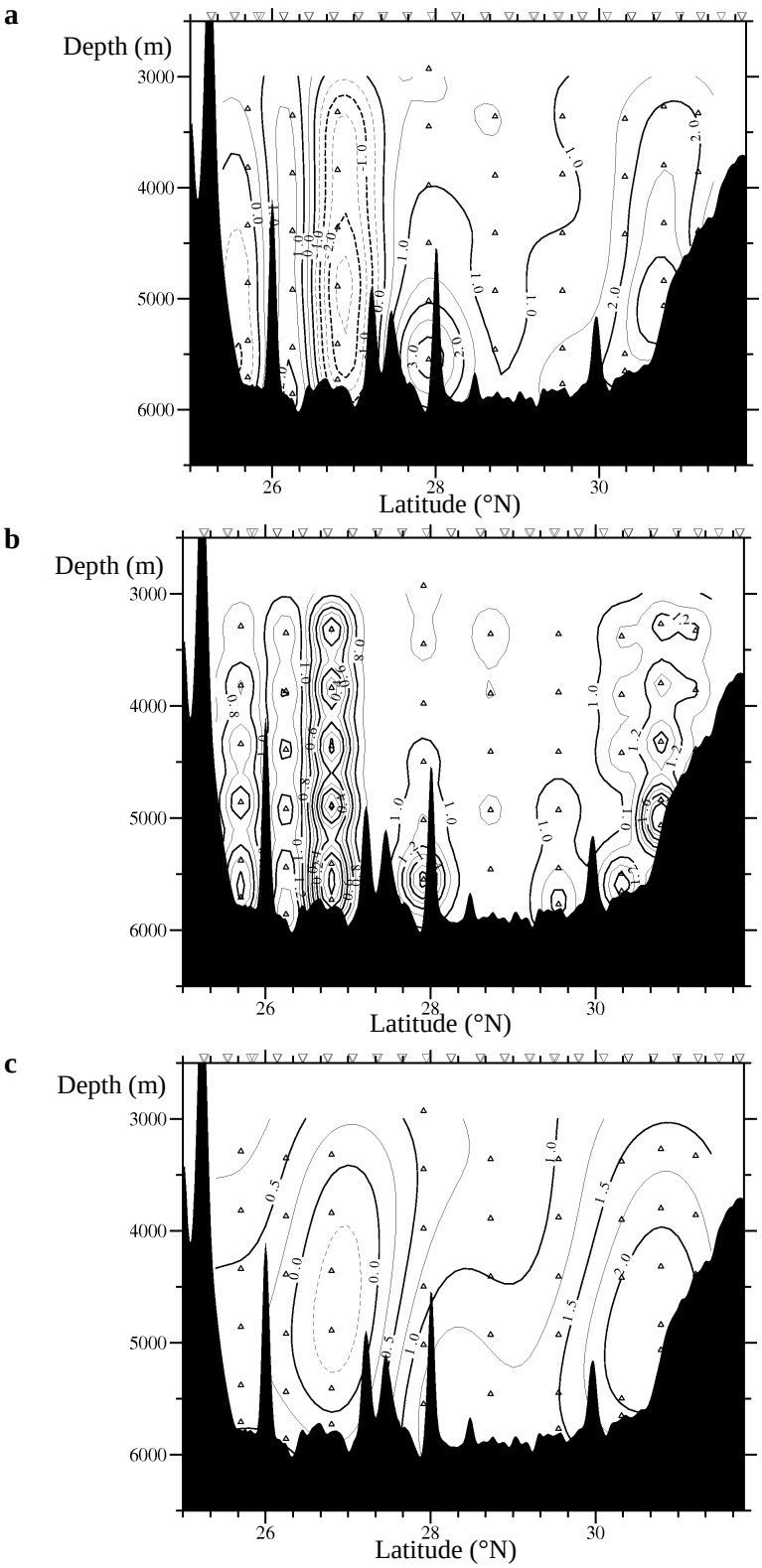

Fig. A.1 Mean normal velocity sections southwest of the Shatsky Rise in Case b2 (a), Case a3 (b), and Case c3 (c). Panel a is the same as Fig. 4.4 in Chapter 4. Contour interval in Panel a, b, and c is 0.5 cm s^{-1}, 0.1 cm s^{-1}, and 0.25 cm s^{-1}, respectively.

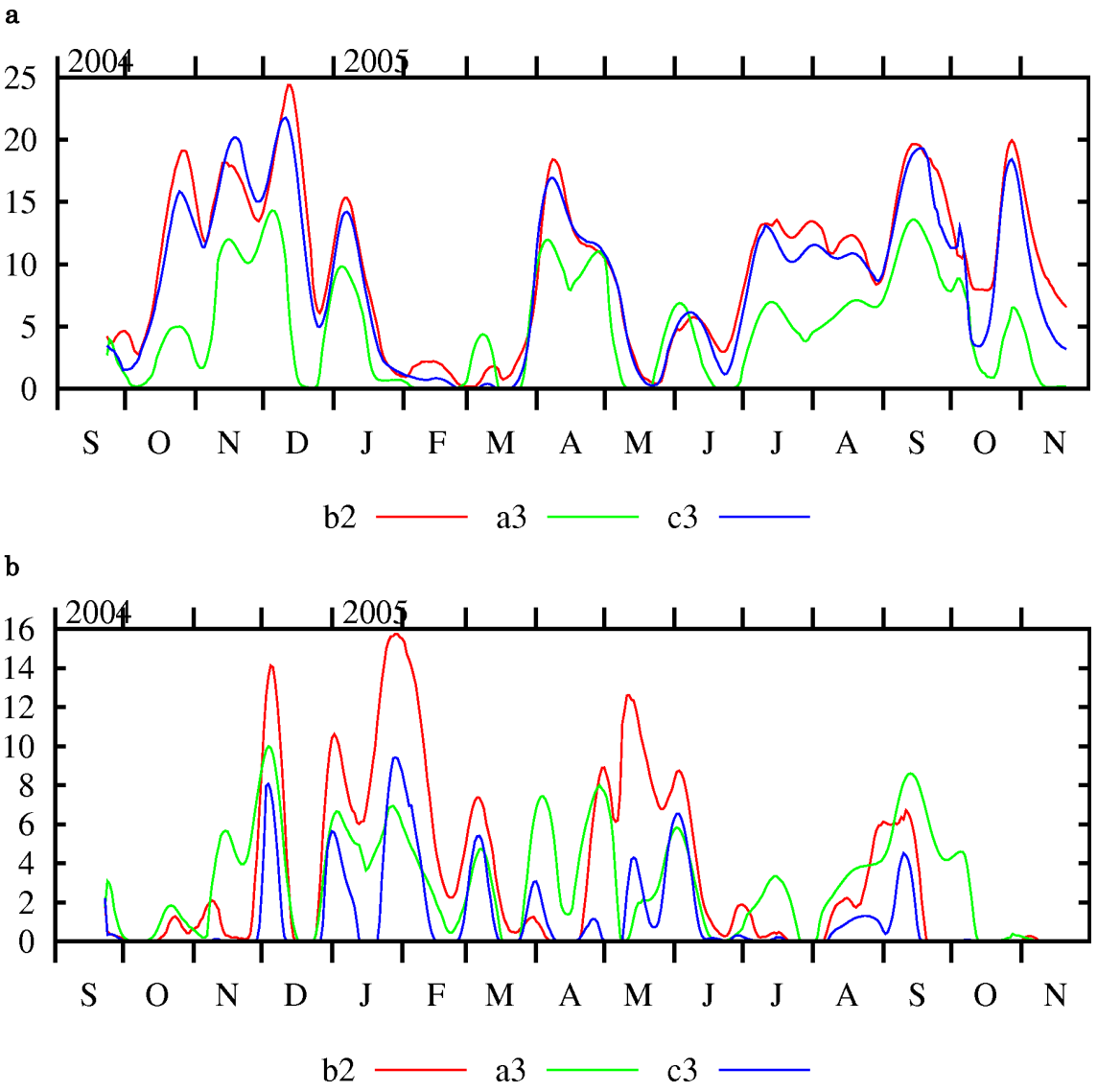

Fig. A.2 Time series of volume transports smoothed with 25-day low-pass filter for the eastern branch (a) and the western branch (b). Red, green, and blue lines in each panel are the time series in Cases b2, a3, and c3, respectively. Red lines for Case b2, based on the parameters adopted in Chapter 4, are the same as thick lines in panels a and b of Fig. 4.9.

Appendix B. Anticyclonic eddy over an isolated seamount

Geostrophic flow in ideal homogeneous fluid follows the isobaths with avoiding an isolated topographic obstacle, over which water is trapped. This trapped-water region is called Taylor column. On the other hand, stratification permits geostrophic flow to pass over an obstacle, and the trapped-water region becomes confined to the vicinity of the obstacle with a shape like cap or cone. This is called Taylor cap or Taylor cone (Hogg, 1973). Various aspects of Taylor caps have attracted many researchers for a long time; particularly from the 1970s to the 1990s, many observational studies were made for documents on Taylor-cap-like effects and many theoretical studies with numerical and laboratory experiments were made for understanding the dynamics of Taylor caps. Roden (1987) reviews theoretical studies mainly based on quasi-geostrophic approximation and observational studies in the 1970s and the 1980s. Numerical modeling has evolved into primitive equation model; Chapman and Haidvogel (1992) present the conditions of formation of Taylor caps over seamounts in steady, rotating, stratified flows.

In a steady, rotating, nearly inviscid, stratified flow, the following parameters generally controls aspects of the flow over a seamount:

Rossby number: $Ro = U/fL$,
Burger number: $S = NH/fL$,
Beta parameter: $b = \beta L^2/U$,
Fractional seamount height: $\delta = h_m/H$,

where U: the speed of the spatially uniform inflow, L: the horizontal scale of the seamount, h_m: the seamount height, H: the depth of the flat bottom around the seamount, N: the buoyancy frequency, f: the Coriolis parameter, and β: the beta parameter.

The overview of transient response of the flow over a seamount is expressed as the following (McCartney, 1975; Verron and LeProvost, 1985; Chapman and Haidvogel, 1992). A spatially uniform inflow impinging on the seamount causes upwelling on its upstream side and downwelling on its downstream side. Stratification parameterized by burger number controls the upwelling and downwelling. The upwelling and downwelling form anticyclonic and cyclonic eddies by shrinking and stretching of water column, respectively. In the Northern Hemisphere, these eddies co-rotate anticyclonically around the seamount with advected by the inflow. Then, the anticyclonic eddy moves to the top of the seamount and is trapped over the seamount, and the cyclonic eddy is carried downstream (Verron and LeProvost, 1985; Chapman and Haidvogel, 1992). If the inflow is strong enough (Rossby number is large), the

anticyclonic eddy is also carried downstream and a Taylor cap is not formed (Chapman and Haidvogel, 1992). If the seamount has an enough large horizontal scale, we must consider the beta effect (Beta parameter is large). In this case, the cyclonic eddy carried downstream by the eastward inflow remains by Rossby wave and develops a complex flow pattern to the east of the seamount. On the other hand, the cyclonic eddy carried downstream by the westward inflow does not develop. Thus, the beta effect causes an asymmetric response to the direction of zonal inflow (McCartney, 1975). If the fractional seamount height is large enough (also stratification is present), the upstream upwelling moves lower dense water to higher layer. This strengthens local density stratification and causes bottom intensification of Taylor cap (Chapman and Haidvogel, 1992).

The seamount near the mooring M4 southwest of the Shatsky Rise in this study (Chapter 4), which is at 28°N ($f = 7 \times 10^{-5}$ s^{-1}, $\beta = 2 \times 10^{-3}$ m^{-1} s^{-1}), has a horizontal scale (L) of 20 km and a height (h_m) of 2200 m (the ambient water depth is ~6000 m and the top is at the depth of ~3800 m) (see Fig. 4.7). Our hydrographic observations southwest of the Shatsky Rise indicate deep density stratification with the buoyancy frequency (N) of 3×10^{-4} s^{-1}. Burger number (S) is about 1.3, which means the deep stratification in this study area is comparable with the effect of the earth rotation. If the inflow has a speed (U) of 5 cm s^{-1}, which is similar to (or rather higher than) the typical current speed in the deep layer of this study area, Beta parameter becomes 0.16 and we can ignore the beta effect. Therefore, we examine the condition of formation of a Taylor cap over the seamount on an f-plane with using the diagram of Chapman and Haidvogel (1992), which shows regimes of Taylor-cap formation by Rossby number (Ro) and fractional seamount height (δ) (Fig. B.1). Their setting of Burger number is S=1, which is almost the same as that in this study area. In the regime of Taylor-cap formation, water particles remain over the seamount with rotating anticyclonically as in Fig. B.2a, while they are swept downstream in the regime of "TT" with slightly larger Rossby number (Fig. B.2b). In the case of this seamount,

Rossby number: $Ro = U/fL \sim 0.04$,
Fractional seamount height: $\delta = h_m/H \sim 0.37$.

This combination of parameters is within the regime of Taylor-cap formation.

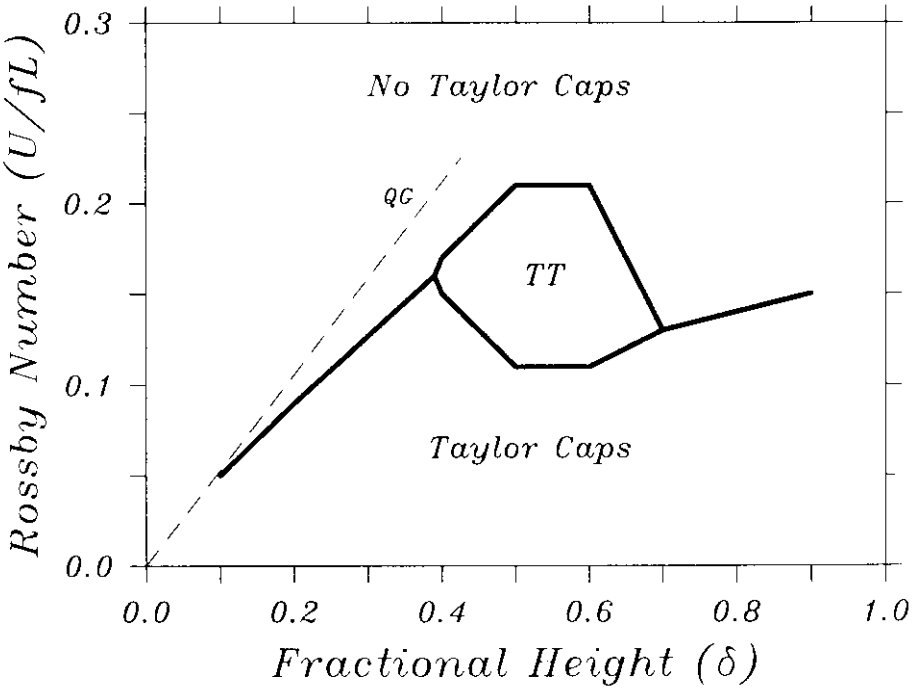

Fig. B.1 Regimes for steady, stratified flow (Burger number is 1) over a seamount estimated from the numerical modeling (divided by solid lines) (Chapman and Haidvogel, 1992). "TT" means the regime of temporarily-trapped eddy before being swept downstream. Regimes divided by a broken line are predicted from quasi-geostrophic (QG) theory.

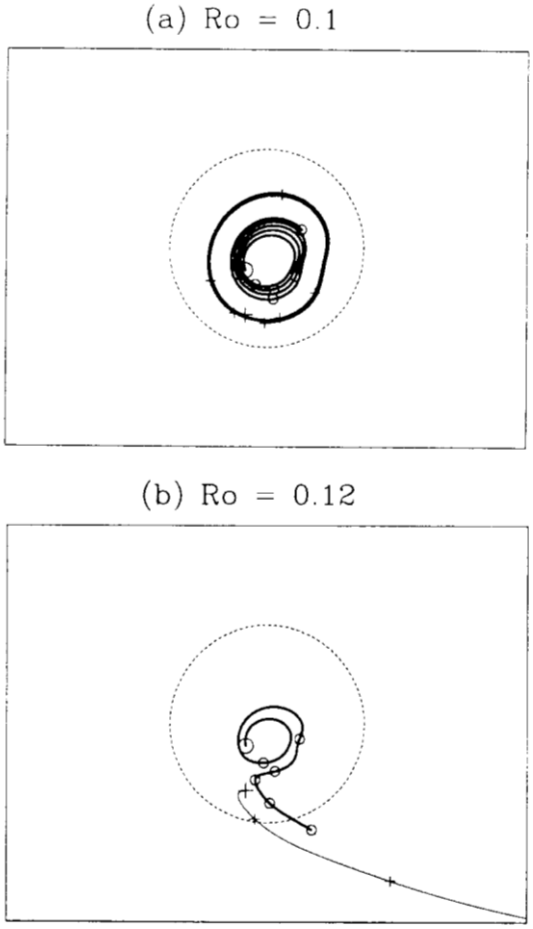

Fig. B.2 Plan views of trajectories of two water particles departed from near-bottom in steady, stratified flow (S = 1) over a seamount with a moderate height (δ = 0.6) (Chapman and Haidvogel, 1992) with inflow speed of Ro = 0.1 (a) and Ro = 0.12 (b). Inflow is from left to right. Particle positions at every 5 days are shown by symbols. Larger symbols denote the start points.

References

Bretherton, F. P., Davis, R. E., Fandry, C. B., 1976. A technique for objective analysis and design of oceanographic experiments applied to MODE-73. *Deep-Sea Research*, **23**, 559–582.

Chapman, D. C., Haidvogel, D. B., 1992. Formation of Taylor caps over a tall isolated seamount in a stratified ocean. *Geophysical and Astrophysical Fluid Dynamics*, **64**, 31–65.

Fofonoff, N. P., Millard, R. C., 1983. Algorithms for the computation of fundamental properties of seawater, UNESCO Technical Papers in Marine Science 44.

Fujio, S., Yanagimoto, D., 2005. Deep current measurements at 38°N east of Japan. *Journal of Geophysical Research*, **110**, C02010, doi:10.1029/2004JC002288.

Fujio, S., Yanagimoto, D., Taira, K., 2000. Deep current structure above the Izu-Ogasawara Trench. *Journal of Geophysical Research*, **105**, 6377–6386.

Hogg, N. G., 1973. On the stratified Taylor column. *Journal of Fluid Mechanics*, **58**, 517–537.

Imawaki, S., 1985. Features of mesoscale eddies in the deep mid-ocean of the western North Pacific. *Deep-Sea Research*, **32**, 599–611.

Ishizaki, H., 1994a. A Simulation of the abyssal circulation in the North Pacific Ocean. Part I: flow field and comparison with observations. *Journal of Physical Oceanography*, **24**, 1921–1939.

Johnson, G. C., Toole, J. M., 1993. Flow of deep and bottom waters in the Pacific at 10˚N. *Deep-Sea Research I*, **40**, 371–394.

Johnson, G. C., Robbins, P. E., Hufford, G. E., 2001. Systematic adjustments of hydrographic sections for internal consistency. *Journal of Atmospheric and Oceanic Technology*, **18**, 1234–1244.

Joyce, T. M., 1987. Hydrographic sections across the Kuroshio extension at 165˚E and 175˚W. *Deep-Sea Research*, **34**, 1331–1352.

Kato, F., Kawabe, M., 2009. Volume transport and distribution of deep circulation at 165°W in the North Pacific. *Deep-Sea Research I*, **56**, 2077–2087.

Kawabe, M, 1993. Deep water properties and circulation in the western North Pacific. In: Teramoto T. (Ed.), Deep Ocean Circulation, Physical and Chemical Aspects. Elsevier Science Publishers, Amsterdam, 17–37.

Kawabe, M, 1996. Preliminary report of the Hakuho-maru cruise KH-95-1. Ocean Res. Inst.,

The Univ. of Tokyo.

Kawabe, M, 2005a. Preliminary report of the Hakuho-maru cruise KH-03-1. Ocean Res. Inst., The Univ. of Tokyo.

Kawabe, M, 2005b. Preliminary report of the Hakuho-maru cruise KH-04-4. Ocean Res. Inst., The Univ. of Tokyo.

Kawabe, M, 2006. Preliminary report of the Hakuho-maru cruise KH-05-4. Ocean Res. Inst., The Univ. of Tokyo.

Kawabe, M., Taira, K., 1995. Flow distribution at 165˚E in the Pacific Ocean. In *Biogeochemical Processes and Ocean Flux in the Western Pacific*, Sakai, H., Nozaki, Y. (eds.), Terra Scientific Publishing Company (TERRAPUB), Tokyo, 629–649.

Kawabe, M., Fujio, S., Yanagimoto, D., 2003. Deep-water circulation at low latitudes in the western North Pacific. *Deep-Sea Research I*, **50**, 631–656.

Kawabe, M., Yanagimoto, D., Kitagawa, S., 2006. Variations of deep western boundary currents in the Melanesian Basin in the western North Pacific. *Deep-Sea Research I*, **53**, 942–959.

Kawabe, M., Fujio, S., Yanagimoto, D., Tanaka, K., 2009. Deep-circulation currents southwest of the Shatsky Rise in the western North Pacific. *Deep-Sea Research I*, **56**, 1675–1687.

Kawabe, M., Yanagimoto, D., Kitagawa, S., Kuroda, Y., 2005. Variations of the deep western boundary current in Wake Island Passage. *Deep-Sea Research I*, **52**, 1121–1137.

Kenyon, K. E., 1983. Sections at 35˚N in the Pacific. *Deep-Sea Research*, **30**, 349–369.

Komaki, K., Kawabe, M., 2009. Deep-circulation current through the Main Gap of the Emperor Seamounts Chain in the North Pacific. *Deep-Sea Research I*, **56**, 305–313.

Macdonald, A. M., Mecking, S., Robbins, P. E., Toole, J. M., Johnson, G. C., Talley, L., Cook, M., Wijffels, S. E., 2009. The WOCE-era 3-D Pacific Ocean circulation and heat budget. *Progress in Oceanography*, **82**, 281–325.

Mantyla, A. W., Reid, J. L., 1983. Abyssal characteristics of the World Ocean waters. *Deep-Sea Research*, **30**, 805–833.

McCartney, M. S., 1975. Inertial Taylor columns on a beta plane. *Journal of Fluid Mechanics*, **68**, 71–95.

Mitchum, G. T., 1995. The source of 90-day oscillations at Wake Island. *Journal of Geophysical Research*, **100**, 2459–2475.

Owens, W. B., Warren, B. A., 2001. Deep circulation in the northwest corner of the Pacific

Ocean. *Deep-Sea Research I*, **48**, 959–993.

Richardson, P. L., 2008. On the history of meridional overturning circulation schematic diagrams. *Progress in Oceanography*, **76**, 466–486.

Roden, G. I., 1987. Effect of seamounts and seamount chains on ocean circulation and thermocline structure. In *Seamounts, Islands and Atolls*, Keating, B., Fryer, P., Batiza, R., Boehlert, G. (eds.), *Geophysical Monograph*, **43**, American Geophysical Union, 335–354.

Roemmich, D., Hautala, S., Rudnick, D., 1996. Northward abyssal transport through the Samoan passage and adjacent regions. *Journal of Geophysical Research*, **101**, 14,039–14,055.

Roemmich, D., McCallister, T., Swift, J., 1991. A transpacific hydrographic section along latitude 24˚N: the distribution of properties in the subtropical gyre. *Deep-Sea Research*, **38**, S1–S20.

Rudnick, D., 1997. Direct velocity measurements in the Samoan Passage. *Journal of Geophysical Research*, **102**, 3293–3302.

Schmitz, Jr., W. J., 1987. Observations of new, large and stable abyssal currents at midlatitudes along 165˚E**.** *Journal of Physical Oceanography*, **17**, 1309–1315.

Schmitz, Jr., W. J., Niiler, P. P., Koblinsky, C. J., 1987. Two-year moored instrument results along 152°E. *Journal of Geophysical Research*, **92**, 10,826–10,834.

Schmitz, Jr., W. J., Niiler, P. P., Bernstein, R. L., Holland, W. R., 1982. Recent long-term moored instrument observations in the western North Pacific. *Journal of Geophysical Research*, **87**, 9425–9440.

Siedler, G., Holfort, J., Zenk, W., Müller, T. J., Csernok, T., 2004. Deep-water flow in the Mariana and Caroline Basins. *Journal of Physical Oceanography*, **34**, 566–581.

Stommel, H., Arons, A. B., 1960. On the abyssal circulation of the world ocean – II. An idealized model of the circulation pattern and amplitude in oceanic basins. *Deep-Sea Research*, **6**, 217–233.

Taft, B. A., Hayes, S. P., Friederich, G. E., Codispoti, L. A., 1991. Flow of abyssal water into the Samoa Passage. *Deep-Sea Research (Suppl. 1)*, **38**, S103–S128.

Talley, L.D., 2007. Hydrographic Atlas of the World Ocean Circulation Experiment (WOCE). Volume 2: Pacific Ocean (eds. Sparrow, M., Chapman, P., Gould, J.), International WOCE Project Office, Southampton, U.K., ISBN 0-904175-54-5.

Thompson, R. O. R. Y., 1983. Low-pass filters to suppress inertial and tidal frequencies. *Journal of Physical Oceanography*, **13**, 1077–1083.

Tsimplis, M. N., Bacon, S., Bryden, H. L., 1998. The circulation of the subtropical South Pacific derived from hydrographic data. *Journal of Geophysical Research*, **103**, C10, 21,443–21,468.

Verron, J., LeProvost, C., 1985. A numerical study of quasi-geostrophic flow over isolated topography. *Journal of Fluid Mechanics*, **154**, 231–252.

Wijffels, S. E., Hall, M. M., Joyce, T., Torres, D. J., Hacker, P., Firing, E., 1998. Multiple deep gyres of the western North Pacific. *Journal of Geophysical Research*, **103**, C6, 12,985–13,009.

Whitworth, T., Warren, B. A., Nowlin, W. D., Rutz, S. B., Pillsbury, R. D., Moore, M. I., 1999. On the deep western-boundary current in the Southwest Pacific Basin. *Progress in Oceanography*, **43**, 1–54.

Yanagimoto, D., Kawabe, M., 2007. Deep-circulation flow at mid-latitude in the western North Pacific. *Deep-Sea Research I*, **54**, 2067–2081.

Yanagimoto, D., Kawabe, M., Fujio, S., 2010. Direct velocity measurements of deep circulation southwest of the Shatsky Rise in the western North Pacific. *Deep-Sea Research I*, **57**, 328–337.